The Dissertation Committee for Rodolfo Santana
certifies that this is the approved version of the following dissertation:

Towards understanding magnetic field generation in relativistic shocks with GRB afterglow observations and the GRB radiation mechanism with Photospheric simulations and the X-ray flare radiation mechanism

Committee:

Pawan Kumar, Supervisor

Miloš Milosavljević

Edward L. Robinson

J. Craig Wheeler

Richard A. Matzner

Towards understanding magnetic field generation in relativistic shocks with GRB afterglow observations and the GRB radiation mechanism with Photospheric simulations and the X-ray flare radiation mechanism

by

Rodolfo Santana, B.S.Phy.

DISSERTATION

Presented to the Faculty of the Graduate School of

The University of Texas at Austin

in Partial Fulfillment

of the Requirements

for the Degree of

DOCTOR OF PHILOSOPHY

THE UNIVERSITY OF TEXAS AT AUSTIN

December 2015

Dedicated to my parents and sisters.

Acknowledgments

First and foremost, I would like to thank my advisor, Pawan Kumar. I would like to thank him for his patience, for never giving up on me, and for giving me the opportunity to join his research group. It was also a privilege to get to experience his great joy of Astrophysics and his deep understanding of Physics, always being able to distill the most complicated processes into simple terms. I also appreciate the interest he has for my research, it allowed me to see the implications of my work and kept me motivated to continue moving forward. I also learned how to approach and solve difficult problems under his guidance, these are skills that will definitely help me in the future. This thesis would have definitely have not been possible without his support. I would also like to thank him for always being available to answer my research questions, for allowing me to be his TA and develop course materials, for allowing me to work on research proposals with him, and for allowing me to give feedback on his review.

I would also like to thank my committee members for attending my committee meetings and for giving me honest feedback. Milos for generously providing computational resources, which helped us perform a large suite of simulations, which produced exciting results and allowed us to obtain a deeper physical insight. Craig and Rob for their encouragement and Richard for

allowing me to stop by his office at any time to get help with General Relativity homework as a first year.

I would also like to thank all the graduate students from Pawan's group and their significant others: Rongfeng Shen, Rodolfo Barniol Duran and Jessa Hollett de Barniol, Patrick Crumley and Diana Crumley, Roberto Hernandez and Daniela DaSuta, and Wenbin Lu. They were very supportive of my research and were great collaborators for talking about Astrophysics and getting answers to my research questions. They were also among my best friends in Austin and provided a lot of support and enjoyment outside of research life.

I would like to thank all my previous research advisors from MIT, for allowing me to join their research groups and for writing recommendation letters for me. Prof. Joshua Winn was my academic advisor and always gave me very helpful advice when faced with difficult decisions about coursework and grad school applications. Prof. Sara Seager was the first person to allow me to join her research group and provided a lot of helpful lessons about attitude and researching, lessons which continue to help me today. Prof. Alison Malcolm for allowing me to work on a computational project for the first time. I learned to code from her, a skill which has been extremely valuable for grad school. Prof. Bernd Surrow, for allowing me to join his research group for my undergrad thesis, for giving me great advice for grad school, and for keeping in touch and continuing to believe in me.

I would also like to thank my fellow classmates: Chi-Ting Chiang, Taylor Chonis, Sam Harrold, Jacob Hummel, Myoungwon Jeon, Jared Rand,

Alan Sluder, Mimi Song, Nalin Vutisalchavakul. It was great to be part of a big class with them and I have learned a lot from them. They were also great to hangout with and understanding/supportive when talking about grad school life.

I would also like to thank my office mates: Sehyun Hwang, John Jardel, JJ Hermes, Yi-Kuan Chiang, Kevin Gullikson, Briana Indahl, Jacob Hummel Sarah Danielle Hummel for putting up with me and being great people to discuss Astronomy and life.

I would also like to thank the following grad students who I shared time with in UT: Tim Weinzirl, Masa Shoji Meghann Agarwal, Paul Robertson, John Jardel, Chris Lindner, Manos Chatzopoulos, Manuel Antonio Merello Ferrada and Victoria Gamonal Gamonal, Michael Gully-Santiago, Jonathan Ganc, Chalence Timber Safranek-Shrader, Julie Krugler Hollek, Randi Ludwig, Benny Tsang Tsz Ho, Aaron Smith, Jeremy Ritter. They made the department and my PhD experience much more enjoyable.

I also had many friends outside the department who were great to talk to and made my life in Austin much more pleasant and enjoyable. I would like to thank Charlie Chen Chieh, Weimin Chen, Juan Guevara, Juan Martinez, Cedric Yu Hao Tsai, Bora Sohn, Tsung-Wei Huang Yingyue Boretz, Elizabeth Lam, Naa Korkoi Pappoe, Nathan Erickson, Bobby Stevens, Akshay Singh, Raj Rao.

I would also like to thank my friends from back home who continue

to believe in me and have always been great friends when I visited home. I would like to thank Mayra Lazarit, Jovanny Navarro , Esmeralda Alvarez, Hiral Bhakta, Denise Cardenas, Joshua Colato, Steven Suon, Evelyn Martinez, Pablo Martinez, Luis Luna, Daniel Cendejaz Mendez, Rudy Torres.

I would also like to thank my cousins for being great family and always being great to talk to when I see them: Irma Zambrano, Henry Zambrano, Edgar Preciado Garcia, Francisco Santana, Chico Santana.

I would also like to thank my high school teachers for challenging me in middle school/high school, believing in me, and doing the best they could to prepare me for the future. I thank them for their unending support and encouragement: Mrs. Mardirosian, Mr. Hart, Mr. Pierson, Mr. Soo Hoo, Mrs. Velarde-Hernandez, Mr. Contreras, Ms. Lo Verme, Mr. Cathers.

I would also like to thank the Astronomy grad coordinators for helping me navigate the graduate program, I definitely would not have graduated without their help: Char Charmarie, Rachel Walker, Susy Graves.

I would also like to thank the following libraries/coffee shops and the librarians/baristas working there. Much of the work presented in this thesis was completed in these fine establishments: 24th street Starbucks, PCL, PMA, Epoch, Strange Brew, Bennu, Mozarts. They provided a nice atmosphere outside of RLM.

Last, but not least, I would like to thank my parents and sisters for always loving me, always encouranging me, always supporting me, and always

being there for me when I needed help.

Towards understanding magnetic field generation in relativistic shocks with GRB afterglow observations and the GRB radiation mechanism with Photospheric simulations and the X-ray flare radiation mechanism

Publication No. _____

Rodolfo Santana, Ph.D.
The University of Texas at Austin, 2015

Supervisor: Pawan Kumar

In this thesis, we present three projects on open questions in the Gamma-ray Burst (GRB) field. In the first project, we used X-ray and optical observations to determine the amount of amplification of the ISM magnetic field needed to explain the GRB afterglow observations. We determined that mild amplification is required, at a level stronger than shock-compression but weaker than predicted by the Weibel mechanism. In the second project, we present a Monte Carlo code we wrote from scratch to perform realistic simulations of the photospheric process, one of the mechanisms considered to explain the GRB gamma-ray emission. We determined that photospheric emission can explain the GRB gamma-ray spectrum above the peak-energy if the photons are taken to have a temperature much smaller than the electron temperature and if the interactions between photons and electrons take place at a

large optical depth. In the third project, we used multi-wavelength observations to constrain the X-ray flare radiation mechanism. We determined that synchrotron from a Poynting jet and the Photospheric process are the best candidates to explain the X-ray flare observations.

Table of Contents

List of Tables

List of Figures

Chapter 1

Introduction

1.1 Brief Overview of GRBs

1.1.1 Summary of GRB Observations

Gamma-ray Bursts (GRBs) are short, intense, and non-repeating flashes of gamma-rays associated with energetic explosions of stars. They typically last ~ 10 sec, they occur in random directions in the sky a few times a day, and they have been observed in distant galaxies. Their gamma-ray spectrum is a non-thermal broken power-law with a peak energy between a few keV and a few MeV and a typical spectrum $f_\nu \propto \nu^0$ ($f_\nu \propto \nu^{-1.2}$) below (above) the peak energy (Band et al., 1993; Kaneko et al., 2006). From the observed redshift and gamma-ray flux, it is determined that GRBs typically radiate $\sim 10^{50} - 10^{54}$ ergs, if their emission is isotropic (Kulkarni et al., 1999). However, the GRB outflow is not spherical, but is instead a highly collimated jet with an opening angle $\sim 2 - 10$ degrees. This reduces the amount of energy released in GRBs to $\sim 10^{48} - 10^{52}$ ergs, similar to supernova explosion energies (Frail et al., 2001; Panaitescu & Kumar, 2001a; Berger et al., 2003a; Curran et al., 2008; Liang et al., 2008; Racusin et al., 2009; Cenko et al., 2010). The typical Lorentz factor of the GRB jet is $\Gamma = 300$ (corresponding to 99.9995% the speed of light) (Molinari et al., 2007; Xue et al., 2009; Liang et al., 2010),

where $\Gamma = 1/\sqrt{1-(v/c)^2}$, v is the speed of the jet, and c is the speed of light. These large Lorentz factors make GRB outflows among the fastest sources in nature. Their spectacular nature, their origin in the distant Universe, and their connection with supernovae explosions have placed the study of GRBs at the forefront of astrophysical research (Piran, 2004; Gehrels et al., 2009; Zhang, 2014; Kumar & Zhang, 2015).

Much of what we have learned about GRBs comes from afterglow observations. The afterglow emission refers to rapidly fading synchrotron emission in the X-ray, optical, and radio bands following the burst of gamma-rays. As the relativistic jet expands outwards, it collides with the surrounding medium. This interaction drives a shock, referred to as the external-forward shock, which deposits energy to the surrounding medium. As GRB jet decelerates, the surrounding medium heats up and radiates the afterglow synchrotron emission (Paczynski & Rhoads, 1993; Meszaros & Rees, 1997; Sari et al., 1998; Sari & Piran, 1999b; Panaitescu & Kumar, 2000; Granot & Sari, 2002). The afterglow light curves typically decline as a power-law $f_\nu \propto t^{-1.0}$. Evidence for the GRB outflow being a highly collimated jet comes from observations of the steepening of afterglow lightcurves to $f_\nu \propto t^{-2.0}$ at ~ 1 day (Rhoads, 1999; Sari et al., 1999). As the GRB jet is decelerated, the strength of the relativistic beaming diminishes and the edge of the GRB jet becomes visible to the observer. The finite angular extent of the ejecta leads to a faster decline of the emission from the jet (the so-called "jet-break"). Direct evidence that the GRB outflow is relativistic comes from the measurement of "superlumi-

nal" motion of the radio afterglow of a relatively nearby burst, GRB 030329 (Taylor et al., 2004). The confirmation of GRBs occurring at cosmological distances comes from the detection of the redshift of the GRB host galaxy from observations of the afterglow spectrum (Costa et al., 1997; van Paradijs et al., 1997; Frontera et al., 1998).

There are two different progenitors that produce GRBs. The so-called "long" GRBs, which emit gamma-rays for more than 2 seconds (Kouveliotou et al., 1993), are associated with the core-collapse of a massive star. Direct evidence for the association of long-GRBs with the explosion of massive stars comes from optical afterglow observations. For several long-GRBs, broad-lined type Ic supernova associated with the GRB have been detected with optical spectrum (Galama et al., 1998; Hjorth et al., 2003; Stanek et al., 2003; Malesani et al., 2004; Modjaz et al., 2006; Campana et al., 2006; Pian et al., 2006; Chornock et al., 2010; Starling et al., 2011; Sparre et al., 2011; Melandri et al., 2012; Xu et al., 2013; Levan et al., 2014). On the other hand, "short" GRBs emit gamma-rays for less than 2 seconds and are associated with the binary merger of two compact object (either two neutron stars or a neutron star and a black hole). Indirect evidence for the association of short GRBs with binary mergers comes from the analysis of short GRB host galaxies. About 20% of the host galaxies of short GRBs are elliptical galaxies with old stellar populations and they are all at low redshifts $z < 2$ (Gehrels et al., 2005; Fox et al., 2005; Barthelmy et al., 2005a; Berger et al., 2005; Bloom et al., 2006; Nakar, 2007; Berger, 2014). Recently, several groups have claimed to have

found more direct evidence for the association of short GRBs with binary mergers from the detection of an infrared excess in the afterglow light curve of short GRB 130603B (Tanvir et al., 2013; Berger et al., 2013). The ejecta launched from short GRBs is expected to be neutron rich, which allows for the creation of heavy elements through the r-process. The infrared excess comes from these heavy elements undergoing radioactive decay (Li & Paczyński, 1998; Metzger et al., 2010; Barnes & Kasen, 2013).

1.1.2 Main Steps Involved in Forming a GRB

These observational signatures have lead to the following general picture for GRBs, shown in Figure 1.1 (Gehrels et al., 2009), with many of the details still not well understood and the focus of active research. On the left hand side of Figure 1.1, as we discussed, long GRBs are produced by the collapse of the core of a massive star, referred to as the collapsar model (Woosley, 1993; Paczyński, 1998; MacFadyen & Woosley, 1999), and short GRBs are produced by the binary merger of two compact objects (Eichler et al., 1989; Narayan et al., 1992). Then, for both long and short GRBs, a central engine is produced. One of the major open questions in the GRB field is: what is the central engine that powers GRBs? The two main central engines that have been studied are the magnetar, a highly magnetized, rapidly rotating neutron star, and the hyper-accreting black hole. In the magnetar model, the source of energy for the relativistic jet is the rotational energy of the magnetar, $E_{\rm rm} = 2 \times 10^{52} M_{1.4} R_{10}^2 P_{\rm ms}^{-2}$ ergs, where $M = 1.4 M_\odot M_{1.4}$ is the

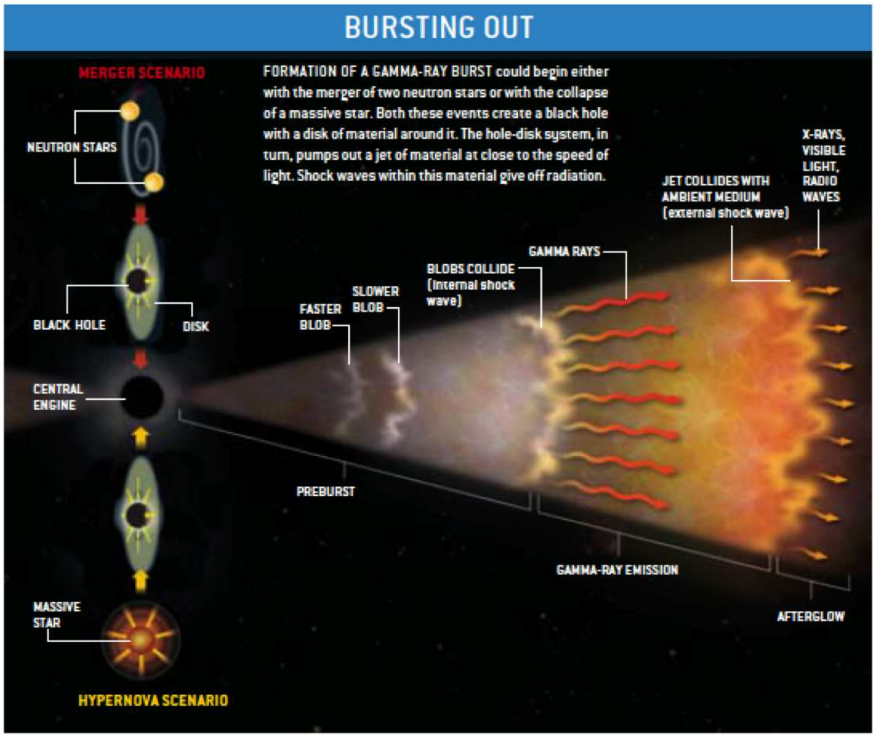

Figure 1.1: Schematic of the main steps involved in the production of a GRB. For the central engine, in addition to an accreting black hole, the magnetar is another possibility for the central engine. For the dissipation of kinetic energy of the jet, in addition to internal shocks, dissipation of magnetic energy by magnetic reconnection in a magnetized jet is another possibility. Figure taken from (Gehrels et al., 2009).

mass of the neutron star, $R = 10^{10}$ cmR_{10} is the radius of the neutron star, and $P = 1$ msec$P_{\rm ms}$ is the rotational period of the neutron star (Usov, 1992; Thompson, 1994a; Dai & Lu, 1998; Kluźniak & Ruderman, 1998; Wheeler et al., 2000; Zhang & Mészáros, 2001; Dai et al., 2006a; Bucciantini et al., 2008, 2009; Metzger et al., 2011). Thus, for a neutron star with a typical M and R, a rapid rotation period ~ 1 msec is required to have enough energy

budget to explain the beaming corrected energies $\sim 10^{51} - 10^{52}$ ergs observed for GRBs. In the black hole model, an accretion disk is produced by gravitationally bound material falling back to the black hole. In order to form a disk, the specific angular momentum of the fallback material needs to be larger than $j_{\rm min} \sim 1.5 \times 10^{16} [M_{BH}/(3M_\odot)] {\rm cm}^2/{\rm sec}$, where $j_{\rm min}$ is the specific angular momentum of the inner most stable orbit around a black hole with mass M_{BH} (Woosley, 2011). The energy released in gamma-ray rays, in terms of the accretion rate $\dot{M}$ and the efficiency of converting accretion power to radiation η, is $E_\gamma = 2 \times 10^{52}$ ergs$(\eta/10^{-3})[\dot{M}/(M_\odot/{\rm sec})]$. For a typical $\eta \sim 10^{-3}$, a high accretion rate $(0.01 - 1) M_\odot/{\rm sec}$ is required to produced the observed energy in gamma-rays.

After the central engine is formed, the jet is launched. In the magnetar model, the jet is formed by a combination of a neutrino driven wind and magnetic dipole radiation (Qian & Woosley, 1996; Metzger et al., 2008; Bucciantini et al., 2008, 2009; Metzger et al., 2011). When the magnetar is born, it is very hot and cools by emitting neutrinos. The large neutrino flux drives baryons from the surface of the neutron star, which produces a wind. Initially, the wind cannot attain a large Lorentz factor since it has a heavy baryon loading. As the magnetar cools, the neutrino flux, and thus the baryon loading of the jet, decreases, allowing for the wind to become relativistic. In the black hole model, the two main mechanisms that have been investigated to power the jet are neutrino annihilation and the Blandford-Znajek (BZ) mechanism. The large accretion rate $(0.01 - 1) M_\odot/{\rm sec}$ required for the black hole

central engine implies that the accretion flow is very dense and cannot cool by emitting photons. At distances ~ 10 Schwarzschild Radii from the black hole, the gas becomes very hot and dense and the accretion flow can cool by producing neutrinos, referred to as a Neutrino-dominated accretion flow (NDAF) (Popham et al., 1999; Narayan et al., 2001; Di Matteo et al., 2002; Kohri & Mineshige, 2002; Kohri et al., 2005). Neutrino anti-neutrino emission from the NDAF can produce a hot photon and electron-positron pair gas (Qian & Woosley, 1996; Chen & Beloborodov, 2007; Zalamea & Beloborodov, 2011; Lei et al., 2013). Neutrinos can also transfer momentum to protons through weak interactions. This hot gas of photons, electron-positron pairs, and protons can then expand to relativistic speeds under its own thermal pressure. In the BZ mechanism, the rotational energy of the black hole is the source of energy for the GRB jet (Blandford & Znajek, 1977; Lee et al., 2000; Wang et al., 2002; McKinney, 2005; Tchekhovskoy & McKinney, 2012a). A magnetic field, which is anchored to the black hole by an accretion disk, extracts the rotational energy of the black hole. In this scenario, the jet is initially magnetized and the jet can accelerate to relativistic speeds either by dissipating its magnetic energy and converting it to kinetic energy or by adiabatic expansion (Drenkhahn, 2002; Drenkhahn & Spruit, 2002; Komissarov, 2004; McKinney, 2005; McKinney & Narayan, 2007; Tchekhovskoy et al., 2008; Komissarov et al., 2009; McKinney & Blandford, 2009; Tchekhovskoy et al., 2010; Granot et al., 2011; Tchekhovskoy & McKinney, 2012b).

After the jet is launched and becomes relativistic, the kinetic energy of

the jet is dissipated and transferred to the particles to produce the gamma-ray emission, referred to as the prompt emission. The two main mechanisms investigated for the dissipation of the kinetic energy of the jet are shocks in baryon-dominated jets, referred to as internal shocks (Rees & Meszaros, 1994), and dissipation of the magnetic field by magnetic reconnection in magnetized jets (Parker, 1957; Sweet, 1958; Kulsrud, 1998; Zweibel & Yamada, 2009; Kagan et al., 2015). In shocks, the particles are accelerated by crossing the shock front multiple times, i.e. the Fermi mechanism (Fermi, 1949; Blandford & Eichler, 1987; Achterberg et al., 2001). In the magnetic reconnection scenario, the particles are accelerated in particle acceleration sites where the magnetic field is small due to magnetic reconnection and the electric field created in this process accelerates the particles (Drake et al., 2006, 2010; Kagan et al., 2013; Sironi & Spitkovsky, 2014; Guo et al., 2014; Werner et al., 2014; Guo et al., 2015).

With the particles now accelerated to relativistic speeds, the radiation mechanism that produces the prompt gamma-ray emission is unknown and one of the major open questions in the GRB field. The radius of emission of the prompt emission is very uncertain, with the possible values ranging from (distances measured with the central engine as the origin) $R \sim 10^{11}$ cm (location at which the outflow becomes optically thin to electron scattering) to $R \sim 10^{17}$ cm (location at which the jet collides with the surrounding medium) (Kumar et al., 2007; Zhang, 2011; Kumar & Zhang, 2015). The three main mechanisms that have been studied are synchrotron, synchrotron self-Compton

(SSC), and the photospheric process. Each of these three mechanisms faces major problems for explaining the prompt emission observations.

The main problem with synchrotron is that for typical GRB parameters, the synchrotron cooling time is much smaller than the dynamical time (Sari et al., 1996; Ghisellini et al., 2000). For rapidly cooling electrons, the spectrum below the peak energy is $f_\nu \propto \nu^{-1/2}$, in disagreement with the observed $f_\nu \propto \nu^0$ low-energy spectrum of the prompt emission. One possibility to avoid the fast cooling of electrons is to have the electrons be re-accelerated before they cool in multiple particle acceleration sites in a magnetized jet (Ghisellini et al., 2000; Kumar & McMahon, 2008). This possibility is currently the focus of active research since the details of energy dissipation and particle acceleration due to magnetic reconnection are complex and poorly understood. In the SSC process, a seed photon field is produced by the synchrotron process and then this photon field is inverse-Compton (IC) scattered by the same electrons that produced the synchrotron photons to the gamma-ray band. The SSC process faces several problems for explaining the prompt emission: 1. the expected seed synchrotron flux in the optical band is $\sim 10^3$ times larger than the observed optical flux during the prompt emission (Piran et al., 2009; Kumar & Zhang, 2015) 2. A 2nd IC scattering, where the gamma-ray photons are IC scattered to higher energies, is also expected to take place. The main problem with a 2nd IC scattering is that it is not detected by the *Fermi*-LAT telescope.

The photospheric process involves photons and electrons undergoing

multiple scatterings while the medium is optically thick (Ghisellini & Celotti, 1999; Mészáros & Rees, 2000; Mészáros et al., 2002; Rees & Mészáros, 2005; Pe'er et al., 2006; Thompson et al., 2007; Pe'er, 2008; Pe'er & Ryde, 2011). The average energy of the photons is taken to be much smaller than the average energy of the electrons. Thus, the photons gain energy from the electrons until they escape the photosphere or until they reach the average energy of the electrons. The photons are usually taken to initially have a blackbody (BB) spectrum. Thus, the goal of the photospheric process is to broaden the BB spectrum so that the exponentially declining Wien tail becomes $f_\nu \propto \nu^{-1.2}$ and so that the Rayleigh-Jeans $f_\nu \propto \nu^2$ spectrum becomes $f_\nu \propto \nu^0$. As with the synchrotron process, the major problem with the photospheric process is that it is very difficulty to broaden the Rayleigh-Jeans part of the BB spectrum to $f_\nu \propto \nu^0$ (Vurm et al., 2013; Lundman et al., 2013; Deng & Zhang, 2014).

After the prompt gamma-ray emission is produced, the jet continues to travel outwards until it collides with the surrounding medium at a distance $R \sim 10^{17}$ cm. As mentioned above, this interaction drives a shock, which interacts with the surrounding medium, referred to as the external-forward shock. The external-forward shock is taken to accelerate the particles of the surrounding medium to relativistic speeds and to amplify the pre-existing magnetic field in the surrounding medium. The accelerated electrons then gyrate around the magnetic field and produce synchrotron emission. This synchrotron emission produces the afterglow emission observed in the X-ray, optical, and radio bands after the burst of gamma-rays.

1.1.3 The *Swift* Satellite and X-ray Flares

Observations from the *Swift* satellite, launched in November 2004 (Gehrels et al., 2004a), have answered a few questions and provided additional puzzles for GRBs. Prior to the *Swift* satellite, afterglow observations typically began ~ 10 hours after the burst of gamma-rays. *Swift* was designed to begin taking X-ray and optical observations ~ 1 minute after the burst of gamma-rays (Burrows et al., 2005b; Roming et al., 2005), closing the gap between the end of the gamma-ray observations and the start of the afterglow emission. *Swift* found many surprising features in the GRB X-ray light curves(Nousek et al., 2006; Zhang et al., 2006). In particular, the X-ray light curves for $\sim 33\%$ of the GRBs detected by *Swift* display a X-ray flare (Burrows et al., 2005a; Chincarini et al., 2007, 2010; Bernardini et al., 2011; Margutti et al., 2011). X-ray flares are large rebrightenings in the X-ray light curve which occur $\sim 100 - 10^5$ sec after the gamma-ray emission. The X-ray flares in Figure 1.2 display a sudden rise in the X-ray flux by a factor $\sim 10^2 - 10^4$. They are called X-ray flares because the sudden rise in the flux is not seen in any other bands. The energy source that powers X-ray flares and the X-ray flare radiation mechanism are current open questions in the GRB field.

1.2 Brief Motivation for Research Projects Presented in This Thesis

In this thesis, we present research work on the magnetic field strength needed to produce afterglow observations, a Monte-Carlo code we wrote to

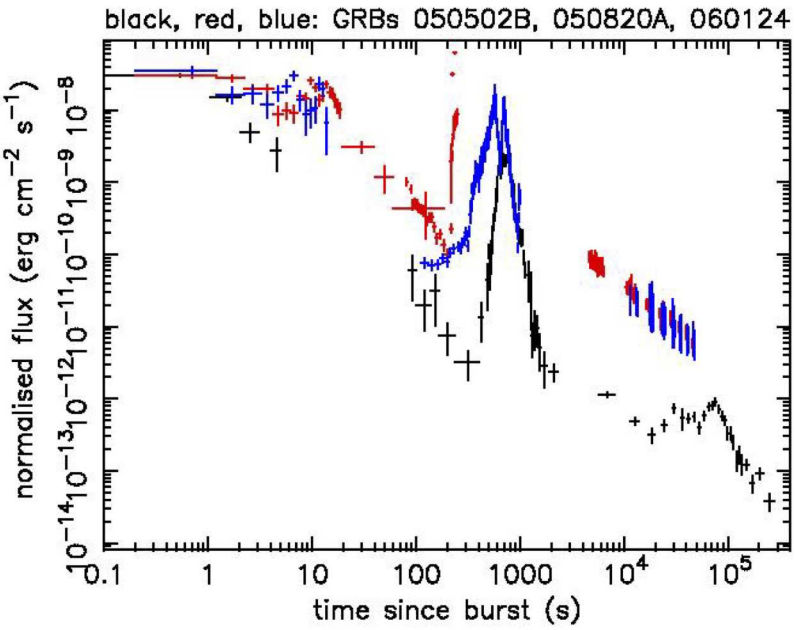

Figure 1.2: X-ray light curves for three GRBs which display X-ray flares. Figure taken from O'Brien et al. (2006a).

simulate the photospheric process and the simulation results, and a study on using optical observations to constrain the X-ray flare radiation mechanism. We now give a brief motivation for each of these projects.

1.2.1 Constraining the Magnetic Field Strength Needed to Produce the Afterglow Emission

The X-ray, optical, and radio afterglow observations are well described by synchrotron radiation produced when the jet collides with the surrounding medium. One of the open questions in the GRB field is, how much amplifica-

tion of the seed magnetic field is needed to explain the afterglow observations? Different theories for magnetic field generation in relativistic shocks predict different levels of amplification for the seed magnetic field. Thus, assuming a typical seed ISM magnetic field $\sim$ 10μG, if we could determine the magnetic field needed to produce the afterglow observations, we can infer the amount of amplification the seed magnetic field experienced. Determining the amount of amplification would then allow us to constrain the mechanism at work for generating the magnetic field in relativistic shocks. In Chapter 2 of this thesis, we use X-ray and/or optical observations from the *Swift* satellite to determine the magnetic field strength needed to produce the afterglow observations. Our study was performed for a large sample of GRBs and is systematic, i.e. we apply the same method to determine the magnetic field strength for each GRB.

1.2.2 Performing Realistic Monte Carlo Simulations of the Photospheric Process

One of the main radiation mechanisms discussed in the literature to explain the prompt gamma-ray emission is the photospheric process. The photospheric process involves the Comptonization of photons and electrons, i.e. photons and electrons undergoing multiple scatterings while the medium is still optically thick. For this project, we wrote a Monte Carlo (MC) code from scratch to simulate this process. In order to simulate it, the prompt emission observations require a photon to electron ratio $\sim 10^5$. We were able to carry out MC photospheric simulations with a realistic photon to electron ratio $\sim 10^5$ for the first time and our simulations were performed for a wide

parameter space. From our simulation results, we will be able to determine under what conditions, if any, can the photospheric model explain the prompt gamma-ray observations. In Chapter 3, we present our MC code algorithm and our MC simulation results.

1.2.3 Constraining the X-ray Flare Radiation Mechanism with Optical Observations

GRB X-ray flares have been demonstrated to have many similarities to the prompt emission. Thus, understanding the X-ray flare radiation mechanism may help us understand the prompt gamma-ray emission, one of the long standing questions in the GRB field. One of the main observational properties of X-ray flares is that although they are extremely bright in the X-ray band, they do not emit radiation in any other band. This is surprising since the *Swift* satellite has provided optical observations for many flares during the X-ray flare episode. Using the optical and X-ray observations, we determined that in order for the X-ray flare to not produce any emission in the optical band, there needs to be a self-absorption break between the optical and X-ray band. We use the location of the self-absorption frequency to determine if synchrotron, SSC, synchrotron radiation from a magnetized jet, or the photospheric process can explain the X-ray flare observations.

Chapter 2

Magnetic Fields In Relativistic Collisionless Shocks

2.1 Abstract

We present a systematic study on magnetic fields in Gamma-Ray Burst (GRB) external forward shocks (FSs). There are 60 (35) GRBs in our X-ray (optical) sample, mostly from *Swift*. We use two methods to study ϵ_B (fraction of energy in magnetic field in the FS). 1. For the X-ray sample, we use the constraint that the observed flux at the end of the steep decline is $\geq$ X-ray FS flux. 2. For the optical sample, we use the condition that the observed flux arises from the FS (optical sample light curves decline as $\sim t^{-1}$, as expected for the FS). Making a reasonable assumption on E (jet isotropic equivalent kinetic energy), we converted these conditions into an upper limit (measurement) on $\epsilon_B n^{2/(p+1)}$ for our X-ray (optical) sample, where n is the circumburst density and p is the electron index. Taking $n = 1$ cm^{-3}, the distribution of ϵ_B measurements (upper limits) for our optical (X-ray) sample has a range of $\sim 10^{-8} - 10^{-3}$ ($\sim 10^{-6} - 10^{-3}$) and median of $\sim$ few $\times 10^{-5}$ ($\sim$ few $\times 10^{-5}$). To characterize how much amplification is needed, beyond shock compression of a seed magnetic field $\sim 10\mu$G, we expressed our results in terms of an amplification factor, AF, which is very weakly dependent on n

($AF \propto n^{0.21}$). The range of AF measurements (upper limits) for our optical (X-ray) sample is $\sim 1-1000$ ($\sim 10-300$) with a median of ~ 50 (~ 50). These results suggest that some amplification, in addition to shock compression, is needed to explain the afterglow observations.

2.2 Introduction

Gamma-Ray Bursts (GRBs) are bright explosions occurring at cosmological distances which release gamma-rays for a brief time, typically on a timescale of $\sim$ few$\times$ 10 sec (e.g. Piran 2004, Gehrels et al. 2009, Zhang 2011). This short-lived emission of gamma-rays is known as the prompt emission. After the prompt emission, long-lived emission in the X-ray, optical, and radio bands (on timescales of days, months, or even years) is also observed from what is called the "afterglow". Although the mechanism for the prompt emission is currently being debated, the afterglow emission has a well-established model based on external shocks (Rees & Meszaros, 1992; Meszaros & Rees, 1993; Paczynski & Rhoads, 1993). In this framework, a relativistic jet emitted by the central engine interacts with the medium surrounding the GRB progenitor. This interaction produces two shocks; the external-reverse shock and the external-forward shock (Meszaros & Rees, 1997; Sari & Piran, 1999b). The external-reverse shock heats up the jet while the external-forward shock heats up the medium surrounding the explosion. The external-reverse shock is believed to be short-lived in the optical band (Sari & Piran, 1999a) and might have been observed, perhaps, in a few cases. The long-lived afterglow emis-

sion is interpreted as synchrotron radiation from the external-forward shock. This shock is taken to produce a power-law distribution of high energy electrons and to amplify the pre-existing seed magnetic field in the surrounding medium. These high energy electrons are then accelerated by the amplified magnetic field and emit radiation by the synchrotron process.

One of the open questions in the field of GRB afterglows is: what is the dynamo mechanism amplifying magnetic fields in the collisionless relativistic shocks involved for GRB external shocks? The magnetic field strength downstream of the shock front is expressed in terms of ϵ_B, which is defined as the fraction of energy that is in the magnetic field downstream of the shock front. With this definition, the explicit expression for ϵ_B is

$$\epsilon_B = \frac{B^2}{32\pi n m_p c^2 \Gamma^2}, \tag{2.1}$$

where B is the co-moving magnetic field downstream of the shock front, n is the density surrounding the GRB progenitor, m_p is the proton mass, c is the speed of light, and Γ is the Lorentz factor of the shocked fluid downstream of the shock front (e.g. Sari et al., 1998; Wijers & Galama, 1999; Panaitescu & Kumar, 2000). If shock compression is the only mechanism amplifying the magnetic field downstream of the shock front, then B is given by $B = 4\Gamma B_0$ (e.g. Achterberg et al., 2001), where B_0 is the seed magnetic field in the medium surrounding the GRB progenitor. Using this expression for B, ϵ_B simplifies to $\epsilon_B = B_0^2/2\pi n m_p c^2$. Using the value for the ambient magnetic field of the Milky Way galaxy $B_0 \sim$ few μG and a density for the surrounding medium of $n = 1$ cm^{-3}, ϵ_B is expected to be $\sim 10^{-9}$.

Several studies have modeled afterglow data to determine what values of the afterglow parameters best describe the observations (e.g. Wijers & Galama, 1999; Panaitescu & Kumar, 2002; Yost et al., 2003; Panaitescu, 2005). The results from previous studies show that ϵ_B ranges from $\epsilon_B \sim 10^{-5} - 10^{-1}$. These values for ϵ_B are much larger than the $\epsilon_B \sim 10^{-9}$ expected from shock compression alone and suggest that some additional amplification is needed to explain the observations. There have been several theoretical and numerical studies that have considered possible mechanisms, operating in the plasma in the medium surrounding the GRB, that can generate extra amplification for the magnetic field. The mechanisms that have been proposed are the two-stream Weibel instability (Weibel, 1959; Medvedev & Loeb, 1999; Gruzinov & Waxman, 1999; Silva et al., 2003; Medvedev et al., 2005) and dynamo generated by turbulence (Milosavljević & Nakar, 2006; Milosavljevic et al., 2007; Sironi & Goodman, 2007; Goodman & MacFadyen, 2008; Couch et al., 2008; Zhang et al., 2009; Mizuno et al., 2011; Inoue et al., 2011).

Recent results (Kumar & Barniol Duran, 2009, 2010) found surprisingly small values of $\epsilon_B \sim 10^{-7}$ for 3 bright GRBs with *Fermi*/LAT detections. These values of ϵ_B are $\sim$ 2 orders of magnitude smaller than the smallest previously reported ϵ_B value and they can be explained with the only amplification coming from shock compression of a seed magnetic field of a few 10μG [1]. Although this seed magnetic field is stronger than the one of the Milky Way

[1]The values given above of $\epsilon_B \sim 10^{-7}$ are under the assumption of $n = 1$ cm^{-3}. It is important to note that when reaching the conclusion that shock compression provides

galaxy by about a factor ~ 10, seed magnetic fields of a few 10μG have been measured before. The seed magnetic fields in the spiral arms of some gas-rich spiral galaxies with high star formation rates have been measured to be 20-30 μG (Beck, 2011). Seed magnetic fields as high as $0.5 - 18$ mG were measured in starburst galaxies by measuring the Zeeman splitting of the OH megamaser emission line at 1667 MHz (Robishaw et al., 2008).

Given this disagreement between the recent and previous results, the question regarding the amplification of magnetic fields in GRB external relativistic collisionless shocks remains unanswered. The first goal of this study is to provide a systematic determination of ϵ_B for a large sample of GRBs by using the same method to determine ϵ_B for each burst in our X-ray or optical sample. This is the first time such a large and systematic study has been carried out for ϵ_B. Knowing the value of ϵ_B for large samples will help us determine how much amplification of the magnetic field is needed to explain the afterglow observations. We mostly limit our samples to GRBs detected by the *Swift* satellite, with measured redshift. In this study, we determine an upper limit on ϵ_B for our X-ray sample and a measurement of ϵ_B for our optical sample. We use a new method to determine an upper limit on ϵ_B with X-ray data, which relies on using the steep decline observed by *Swift*

enough amplification to explain the afterglow data, Kumar & Barniol Duran (2009, 2010) did not assume a value for n. Also, the results of small $\epsilon_B \sim 10^{-7}$ values do not depend on whether or not the LAT emission is produced by the external-forward shock. These small ϵ_B values were inferred from the late time X-ray and optical data and from the constraint that the external-forward shock does not produce flux at 150 keV that exceeds the observed prompt emission flux at 50 seconds.

in many X-ray light curves. We expect that the observed flux at the end of the steep decline is larger than the predicted flux from the external-forward shock. Making reasonable assumptions about the other afterglow parameters, we are able to convert this constraint into an upper limit on ϵ_B. To determine a measurement of ϵ_B for our optical sample, we restrict our sample to light curves that show a power law decline with a temporal decay ~ 1 at early times, $\sim 10^2 - 10^3$ seconds, as expected for external-forward shock emission. We choose this selection criteria so that the optical emission is most likely dominated by external-forward shock emission. Making the same reasonable assumptions for the other afterglow parameters and using the condition that the observed flux from the optical light curve is equal to the external-forward shock flux, we are able to convert this condition into a measurement of ϵ_B. We also applied a consistency check for the bursts that are in common to our X-ray and optical samples to make sure our results for ϵ_B are correct. The second goal of this study is to determine how much amplification, in addition to shock compression, is needed to explain the results for the ϵ_B upper limits/measurements. To quantify how much amplification beyond shock compression is required by the observations, we also express the results we found for the ϵ_B upper limits (measurements) for our X-ray (optical) sample in terms of an amplification factor.

This paper is organized as follows. We begin in Section 2.3 by presenting a review of the values previous studies have found for the microphysical afterglow parameters ϵ_e (the fraction of energy in electrons in the shocked

plasma) and ϵ_B. In Section 2.4 (Section 2.5), we present the method we use to determine an upper limit (measurement) on ϵ_B and apply it to our X-ray (optical) sample of GRBs. In Section 2.6, we use the GRBs that are in common to both samples to perform a consistency check. We search for a possible correlation between the kinetic energy of the blastwave and ϵ_B in Section 2.7. In Section 2.8, we write our results for ϵ_B for our X-ray and optical samples in terms of an amplification factor, which quantifies how much amplification – beyond shock compression – is required by the observations. Lastly, in Section 4.8, we discuss our results and present our conclusions. The convention we use for the specific flux f_ν, the flux per unit frequency ν, is $f_\nu \propto \nu^{-\beta} t^{-\alpha}$. In this convention, β is the spectral decay index and α is the temporal decay index. For a GRB at a given redshift z, when calculating the luminosity distance to the GRB, d_L, we used the Cosmological parameters $H_0 = 71$ km/sec/Mpc, $\Omega_m = 0.27$, and $\Omega_\Lambda = 0.73$.

2.3 Literature Review Of Values Of ϵ_e and ϵ_B

The flux observed from the external-forward shock depends on 6 parameters. These parameters are E, n, s, ϵ_e, ϵ_B, and p. E is the isotropic equivalent kinetic energy of the jet and n is the number density of the surrounding medium. The density is taken to be spherically symmetric and to decrease with r as $n(r) \propto r^{-s}$, where s is a constant determining the density profile of the surrounding medium and r is the distance from the center of the explosion. Two cases are usually considered for the density profile: $s = 0$

and $s = 2$, which respectively correspond to a constant density medium and a wind medium. The microphysical parameters are ϵ_e and ϵ_B, where ϵ_e (ϵ_B) is the fraction of energy in the electrons (magnetic field) in the shocked fluid. The microphysical parameters are taken to be constant throughout the afterglow emission. A power law distribution of electrons, $dN_e/d\gamma_e \propto \gamma_e^{-p}$ with $\gamma_e \geq \gamma_i$, where γ_e is the Lorentz factor of the electrons, γ_i is the minimum Lorentz factor of the electrons, and N_e is the number of electrons, is assumed to be produced when the external-forward shock interacts with the surrounding medium. The power-law index of the electron distribution, p, is a constant known as the electron index.

In practice, it is very difficult to determine the values of the 6 afterglow parameters. The value of p and the density profile of the surrounding medium (whether we have a $s = 0$ or $s = 2$ medium) can be determined from observations of the afterglow spectral decay and temporal decay of the light curve with the so-called "closure" relations (e.g. Zhang et al., 2006). The remaining 4 afterglow parameters are more difficult to determine. What is needed to determine these 4 parameters is observations of the afterglow emission in the 4 different spectral regimes of the synchrotron afterglow spectrum (we will discuss the afterglow synchrotron spectrum in more detail in Section 2.4.4). In practice, most GRBs do not have this wealth of observations. In order to determine these 4 parameters, previous works have either focused only on determining the afterglow parameters for bursts with high quality data, spanning all portions of the synchrotron spectrum, or have applied various simplifying

assumptions.

We performed a literature search for papers that determine values for ϵ_e and ϵ_B to get an idea of what typical values previous works have found. Different authors applied different techniques for finding ϵ_e and ϵ_B. When displaying the results from the literature, we did not discriminate against any method and simply plotted every value we found. However, we did not consider works that made simplifying assumptions when determining ϵ_e and ϵ_B, such as equipartition of proton and electron energy (ϵ_e). The GRBs for which we found ϵ_e and ϵ_B values are shown in Table A.1 in Appendix A. Except for GRB 080928, all the GRBs in our sample have radio, optical, and X-ray observations, allowing for a determination of all the afterglow parameters. We included GRB 080928 in our sample because ϵ_e and ϵ_B were able to be uniquely determined from optical and X-ray observations (Rossi et al., 2011).

The ϵ_e values we found in the literature for 29 GRBs are shown in the histogram in the left panel of Figure 2.1. There is a narrow distribution for ϵ_e; it only varies over one order of magnitude, from $\sim 0.02 - 0.6$, with very few GRBs reported to have $\epsilon_e < 0.1$. The mean of this distribution is 0.24 and the median is 0.22. About 62% of the GRBs in this sample have $\epsilon_e \sim 0.1 - 0.3$. These results for ϵ_e are also supported by recent simulations of relativistic magnetized collisionless electron-ion shocks presented in Sironi & Spitkovsky 2011, where they found $\epsilon_e \sim 0.2$. The narrow distribution of ϵ_e values from the literature and the results from recent simulations both show that ϵ_e does not change by much from GRB to GRB.

The ϵ_B values we found in the literature for 30 GRBs are show in the histogram in the right panel of Figure 2.1. Comparing the two histograms in Figure 2.1, we can immediately see that there is a much wider range in the distribution of ϵ_B, with ϵ_B ranging from $\sim 3.5\times10^{-5}-0.33$. A noticeable peak, containing about 24% of the bursts, is seen in the bin with $-1 < \log_{10}(\epsilon_B) < -0.5$. Two other peaks, each containing about 17% of the GRBs, are seen in the bins with $-2 < \log_{10}(\epsilon_B) < -1.5$ and $-4 < \log_{10}(\epsilon_B) < -3.5$. The mean of this distribution is 6.3×10^{-2} and the median is 1.0×10^{-2}. The important point of the ϵ_B histogram is that ϵ_B varies over 4 orders of magnitude, showing that ϵ_B has a wide distribution and is an uncertain parameter.

2.4 Upper Limit On ϵ_B With *Swift* X-ray Light Curves

2.4.1 Constraining ϵ_B With The X-ray Light Curve Steep Decline

One interesting property found by *Swift* (Gehrels et al., 2004b) is that at early times, about 50% of the light curves detected by the XRT (X-ray Telescope, Burrows et al., 2005a) display a very rapid decline in flux, known as the steep decline (Gehrels et al., 2009). The flux during the steep decline typically decays as t^{-3} and it usually lasts $\sim 10^2 - 10^3$ sec. By extrapolating the BAT (Burst Alert Telescope, Barthelmy et al., 2005b) emission to the X-ray band, O'Brien et al. 2006b showed that there is a continuous transition between the end of the prompt emission and the start of the steep decline phase. This important conclusion lead to the interpretation that the X-ray steep decline has an origin associated with the end of the prompt emission.

The favored interpretation for the origin of the steep decline is high latitude emission (Kumar & Panaitescu, 2000). Although high latitude emission is able to explain most of the steep decline observations, some GRBs display spectral evolution during the steep decline (Zhang et al., 2007b), which is not expected. In any case, the steep decline cannot be produced by the external-forward shock. Therefore, the observed flux during the steep decline should be larger than or equal to the flux produced by the external-forward shock. We do however assume that the time at which the steep decline typically ends, at about $10^2 - 10^3$ seconds, is past the deceleration time[2]. For our upper limit on ϵ_B with X-ray data, we will use the expression for the flux from the external-forward shock, which uses the kinetic energy of the blastwave given by the Blandford and McKee solution (Blandford & McKee, 1976). Since this solution is only valid for a decelerating blastwave, we need to be past the deceleration time for it to be applicable.

Theoretically, it is expected that that the deceleration time occurs before the end of of the steep decline. Depending on the density profile of the surrounding medium, the deceleration time $t_{\rm dec}$ is given by

$$t_{\rm dec} = \begin{cases} (220 \text{ sec}) E_{53}^{1/3} n_0^{-1/3} \Gamma_2^{-8/3} (1+z) & s = 0 \\ (67 \text{ sec}) E_{53} A_{*,-1}^{-1} \Gamma_2^{-4} (1+z) & s = 2 \end{cases} \tag{2.2}$$

(e.g. Panaitescu & Kumar, 2000). In these expressions, Γ is the Lorentz factor of the shocked fluid, z is the redshift, and we have adopted the usual notation

[2]The deceleration time marks the time when about half of the kinetic energy of the blastwave has been transferred to the surrounding medium.

$Q_n \equiv Q/10^n$. For $s = 2$, the proportionality constant of the density, A, is normalized to the typical mass loss rate and stellar wind velocity of a Wolf-Rayet star, which is denoted by A_* and is defined as $A_* \equiv A/(5 \times 10^{11}$ g cm$^{-1})$ (Chevalier & Li, 2000). For typical GRB afterglow parameters of $E_{53} = 1$, $n_0 = 1$ (or $A_* = 0.1$ for $s = 2$), $\Gamma_2 = 3$, and $z = 2.5$, the deceleration time is under 100 seconds for both $s = 0$ and $s = 2$. Although there can be a large uncertainty in the afterglow parameters E and n, Γ is the most important parameter when calculating $t_{\rm dec}$ since $t_{\rm dec}$ has a very strong dependence on Γ. For $s = 0$ ($s = 2$), even if we take extreme parameters for E and n, such as a high kinetic energy of $E_{53} = 100$ and a low density of $n = 10^{-3}$ cm^{-3} ($A_* = 10^{-2}$), with a typical $\Gamma_2 = 3 - 4$ (e.g. Molinari et al., 2007; Xue et al., 2009; Liang et al., 2010), $t_{\rm dec}$ is still a few hundred seconds. Thus, since the deceleration time is less than the typical time at which the steep decline ends, the onset of the external-forward shock emission occurs before the end of the steep decline.

Observationally, the deceleration time is also seen to occur before the end of the steep decline for many GRBs. If the dominant contribution to the light curves at early times is the external-forward shock, the light curve is expected to rise as a power law, reach a peak, and then decline as a power law, with the peak signifying the deceleration time. In Liang et al. 2010, a sample of optical light curves that display this peak is studied. In their Figure 1, for each GRB, they display both the optical light curve and the X-ray light curve. For all their bursts that display a steep decline in the X-ray light curve

(except for GRB 080303 and GRB 081203A), it can be seen that the peak of the optical light curve occurs before the end of the X-ray steep decline. We did not include GRB 080330 and GRB 081203A in our samples.

Since an increase in ϵ_B increases $f_{\rm ES}$ (external-forward shock flux), the condition that the X-ray flux during the steep decline should be larger than or equal to $f_{\rm ES}$ gives an upper limit on ϵ_B. Since our goal is to attain the most stringent upper limit on ϵ_B, we take this constraint at the end of the steep decline. Explicitly, the constraint we will use to find an upper limit on ϵ_B with X-ray data is

$$f_{\rm EoSD} \geq f_{\rm ES}(E, n, s, \epsilon_e, \epsilon_B, p). \tag{2.3}$$

In this inequality, $f_{\rm EoSD}$ represents the observed flux at the end of the steep decline (EoSD). We have also explicitly shown the dependence of $f_{\rm ES}$ on the afterglow parameters. We will now discuss the assumptions we make on the other afterglow parameters, which will allow us to calculate an upper limit on ϵ_B.

2.4.2 The Other Afterglow Parameters

2.4.2.1 E and ϵ_e

Although we do not know the isotropic equivalent kinetic energy of the blastwave E, we can calculate the isotropic energy released in gamma-rays during the prompt emission:

$$E^{\gamma}_{iso} = \frac{\text{fluence} \times 4\pi d_L^2}{1+z}. \tag{2.4}$$

In this equation, the fluence has units of ergs/cm^2 and it represents the flux detected in gamma-rays, integrated over the duration of the prompt emission. d_L is the luminosity distance. Since we are interested in the fluence radiated in gamma-rays, we use the fluence detected in the BAT band, ranging from 15-150 keV (Barthelmy et al., 2005b). The fluences detected by BAT for each GRB can be found in NASA's *Swift* GRB Table and Lookup website.

To convert E^{γ}_{iso} to E, we need to know the efficiency in the conversion of kinetic energy of the jet to prompt gamma-ray emission. Recent studies on the prompt emission efficiency, using X-ray light curves with plateaus detected by *Swift*, were presented in Granot et al. (2006) and Zhang et al. (2007a). For the 23 GRBs for which Zhang et al. (2007a) presented results for the efficiency (see their Table 3), more than half of them were found to have a high efficiency $\gtrsim 30\%$ [3], with a few being estimated to have an efficiency as high as 90%. A high efficiency of $\sim$90% was also found in Granot et al. (2006). However, Fan & Piran 2006 argue that bursts with X-ray plateaus should have more moderate efficiencies $\sim 10\%$. In addition, Zhang et al. (2007a) mention that the efficiencies they calculate for some bursts have large errors due to the uncertainty in the microphysical parameters ϵ_e and ϵ_B. In this work, we will

[3] In Table 3 of Zhang et al. (2007a), they present two different estimates for the efficiency. If the shallow decay of plateaus seen in X-ray light curves is due to energy injection, the more appropriate of the two estimates for the efficiency is denoted as $\eta_\gamma(t_{\rm dec})$. $\eta_\gamma(t_{\rm dec})$ represents the efficiency in gamma-ray radiation (η_γ) calculated at the deceleration time $t_{\rm dec}$.

take a standard choice and calculate E with the expression

$$E = 5E^{\gamma}_{\rm iso}. \tag{2.5}$$

From the definition of the efficiency, $\eta = E^{\gamma}_{\rm iso}/(E^{\gamma}_{\rm iso} + E)$, Equation 2.5 corresponds to an efficiency of $\sim 20\%$. At the end of Section 2.4.5, we will discuss in more detail how the uncertainty in the efficiency affects our results. For our X-ray sample (see Section 2.4.3), from Equation 2.5, we found values for E in the range of $10^{51} - 10^{54}$ ergs, with a typical value $\sim 10^{53}$ ergs. The average value of E_{53} for our X-ray sample is 2.8 and the median is 1.6. The fluence detected in the BAT band, $E^{\gamma}_{\rm iso,52}$, z, and d_{L28} for each GRB in our X-ray sample are shown in Table 2.1 [4].

For ϵ_e, we assumed a value of 0.2 for all of the GRBs in our sample. This choice for ϵ_e is justified from the results of ϵ_e with previous afterglow studies (Figure 2.1) and with recent results from simulations (Sironi & Spitkovsky, 2011), as discussed in Section 2.3.

2.4.2.2 Electron power-law index and density profile

In afterglow studies, s and p can be obtained by determining which closure relation the observed temporal and spectral decay indices satisfy. We cannot use this strategy to determine p and s for our X-ray sample since the external-forward shock flux is below the observed steep decline emission.

[4]Except for GRBs 060708, 060906, 061021, 061222A, 080906, and 081230, we obtained all the redshifts from NASA's *Swift* GRB Table and Lookup website. For the exceptions, we obtained the redshifts from the website on GRB redshifts maintained by J. Greiner.

Instead, we use a fixed p for all GRBs in our X-ray sample. We consider a small value of $p = 2.2$, a typical value of $p = 2.4$ for *Swift* GRBs (Curran et al., 2010), and a larger value of $p = 2.8$. Previous afterglow studies have found that the majority of afterglow observations are better described by a constant density medium (e.g. Panaitescu & Kumar, 2002; Schulze et al., 2011). However, there are still a number of cases where the wind medium is a better model for the afterglow observations. Therefore, we will consider both $s = 0$ and $s = 2$ when displaying the results for the upper limit on ϵ_B.

2.4.2.3 Density

The density of the medium in the vicinity of GRBs is a highly uncertain parameter. A histogram of values of n determined by previous afterglow modelling studies can be found in Figure 9 of Soderberg et al. (2006), which shows n to vary over 5 orders of magnitude, ranging from $\sim 10^{-3}$ cm^{-3} to $\sim 10^{2}$ cm^{-3}. In Section 2.4.5, we will discuss in more detail how the uncertainty in the density affects our results for the ϵ_B upper limits.

2.4.3 The X-ray Sample

For our constraint on ϵ_B with X-ray data, we only consider X-ray data detected by the XRT on board *Swift*. We used the X-ray light curves presented in Butler & Kocevski (2007b). With the exception of two cases, we only consider bursts that display a steep decline in their X-ray light curve (see below). After the end of the steep decline, GRBs display a variety of temporal decays

(Evans et al., 2009). Our sample can be divided into 4 different subgroups, based on the temporal decay after the steep decline:

1. Steep Decline To Plateau: In this subgroup, GRBs display a plateau after the steep decline ($\sim$ 73% of our sample). In Table 2.1, we display the time at the end of the steep decline in units of 10^2 sec, $t_{2,\mathrm{EoSD}}$, and the observed flux at the end of the steep decline at 1 keV, $f_{1\mathrm{keV,EoSD}}$, in μJy.

2. Steep Decline To Normal Decline: In this subgroup, GRBs display a temporal decay of $\alpha \sim 1$ after the steep decline ($\sim$ 18% of our sample). In Table 2.1, we show the time and the flux at the end of the steep decline.

3. Clear Steep Decline But Not A Clear End To The Steep Decline: In this subgroup, it cannot be determined where the steep decline ends (the XRT observations end before the steep decline ends). The following GRBs fall into this subgroup: 050315, 060202, 070419A, 071122, and 090516. For these GRBs, in Table 2.1, we show the flux and the time of the last steep decline point observed. For these GRBs, to be sure that the last steep decline point observed is past the deceleration time, we made sure that it is at a few hundred seconds.

4. No Clear Steep Decline Seen, Just Plateau: Two of the GRBs in our X-ray sample, 050401 and 060927, do not display a steep decline. The first observation of the X-ray light curve for these bursts is during the plateau.

We did not remove these GRBs from our X-ray sample because they are also part of our optical sample (bursts with both X-ray and optical data are important because they allow us to cross-check our results, see Section 2.6). For these 2 bursts, we considered the first observation in the X-ray light curve for our constraint so that we have the least amount of energy injection. We made sure that this point is at least at a few hundred seconds so that we can be confident that the onset of the external-forward shock emission has occurred. For these two bursts, we show the time and the flux of the first X-ray observation of the plateau in Table 2.1.

In addition, 25% of the GRBs in our X-ray sample display X-ray flares during the steep decline. We only consider bursts where the X-ray flare ends before the end of the steep decline because it is difficult to determine the flux and time at the end of the steep decline for bursts that show X-ray flares near the end of the steep decline. It is fine to consider these bursts because observationally, after the X-ray flare, the X-ray light curve is seen to return to the same temporal decay prior to the X-ray flare (e.g. Chincarini et al. 2007). Lastly, GRB 051221A is the only short GRB in our X-ray sample; all the other bursts in our X-ray sample are long GRBs.

Table 2.1: Properties of X-ray Sample

GRB	z	d_{L28}	Fluence $[\times 10^{-6}$ ergs/cm$^2]$	$E^{\gamma}_{\rm iso,52}$	$t_{2,\rm EoSD}$	$f_{\rm 1keV,EoSD}$ $[\mu$Jy]	$\log_{10}(\epsilon_B)$ $(s=0)$	$\log_{10}(\epsilon_B)$ $(s=2)$
050315	1.949	4.71	3.22	3.04	4	3	-5.2	-6.0
050401	2.9	7.67	8.22	15.56	2	80	-4.7	-5.4
050721	2.5	6.40	3.62	5.32	4	30	-4.2	-5.0
050803	0.422	0.71	2.15	0.10	3	10	-3.8	-5.4
050814	5.3	15.76	2.01	9.95	9	1	-5.4	-6.0

Table 2.1: Properties of X-ray Sample (Continued)

GRB	z	d_{L28}	Fluence $[\times 10^{-6}$ ergs/cm$^2]$	$E^{\gamma}_{\rm iso,52}$	$t_{2,\rm EoSD}$	$f_{\rm 1keV,EoSD}$ μJy	$\log_{10}(\epsilon_B)$ $s=0$	$\log_{10}(\epsilon_B)$ $s=2$
051221A	0.547	0.97	1.15	0.09	6	5	-3.5	-4.9
060108	2.03	4.95	0.37	0.38	6	0.8	-4.2	-5.5
060111B	2	4.86	1.60	1.58	2	8	-4.6	-5.8
060115	3.53	9.72	1.71	4.48	8	1	-5.2	-5.9
060210	3.91	10.99	7.66	23.66	8	40	-4.4	-4.7
060418	1.49	3.37	8.33	4.79	5	40	-4.3	-4.9
060502A	1.51	3.43	2.31	1.36	3	7	-4.6	-5.7
060607A	3.082	8.25	2.55	5.35	5	60	-3.6	-4.3
060707	3.425	9.37	1.60	3.99	9	3	-4.5	-5.2
060708	1.92	4.62	0.49	0.45	2	10	-3.7	-5.2
060714	2.71	7.06	2.83	4.78	3	10	-4.8	-5.7
060729	0.54	0.96	2.61	0.20	6	7	-3.8	-5.1
060814	0.84	1.65	14.60	2.71	8	8	-5.0	-5.6
060906	3.686	10.24	2.21	6.21	4	0.8	-5.9	-6.7
060926	3.208	8.66	0.22	0.49	2	4	-3.8	-5.4
060927	5.6	16.81	1.13	6.08	0.8	8	-5.3	-6.6
061021	0.3463	0.56	2.96	0.09	3	10	-3.9	-5.5
061110A	0.758	1.45	1.06	0.16	5	5	-3.6	-6.0
061121	1.314	2.88	13.70	6.19	2	40	-5.1	-5.8
061222A	2.088	5.13	7.99	8.55	2	40	-4.9	-5.7
070110	2.352	5.94	1.62	2.14	4	8	-4.3	-5.3
070306	1.497	3.39	5.38	3.12	7	4	-5.0	-5.6
070714B	0.92	1.85	0.72	0.16	4	6	-3.5	-5.0
070802	2.45	6.24	0.28	0.40	5	0.8	-4.2	-5.5
071122	1.14	2.41	0.58	0.20	8	0.8	-4.1	-5.4
080310	2.43	6.18	2.30	3.22	10	2	-4.8	-5.4
080413A	2.433	6.19	3.50	4.91	2	10	-5.1	-6.0
080430	0.767	1.47	1.20	0.19	2	10	-3.9	-5.5
080607	3.036	8.10	24.00	49.07	3	90	-5.2	-5.5
080721	2.591	6.68	12.00	18.75	0.7	900	-4.3	-5.1
080905B	2.374	6.00	1.80	2.42	2	20	-4.3	-5.4
080906	2.1	5.16	3.50	3.78	7	20	-4.0	-4.7
080916A	0.689	1.29	4.00	0.50	3	10	-4.4	-5.7
081007	0.5295	0.93	0.71	0.05	2	8	-3.5	-5.3
081008	1.9685	4.77	4.30	4.14	6	20	-4.2	-4.9
081230	2	4.86	0.82	0.81	3	6	-4.1	-5.3
090418A	1.608	3.71	4.60	3.05	2	20	-4.8	-5.8
090516A	4.109	11.66	9.00	30.08	6	10	-5.4	-5.7
090519	3.85	10.79	1.20	3.62	5	0.8	-5.4	-6.2
090529	2.625	6.79	0.68	1.09	20	0.5	-4.3	-5.1
090618	0.54	0.96	105.00	7.86	4	200	-4.9	-5.3
090926B	1.24	2.68	7.30	2.95	5	10	-4.8	-5.6
091029	2.752	7.19	2.40	4.16	6	1	-5.5	-6.2
091109A	3.076	8.25	1.60	3.35	5	2	-5.0	-5.8
100302A	4.813	14.06	0.31	1.33	8	1	-4.2	-5.2
100425A	1.755	4.14	0.47	0.37	3	7	-3.6	-5.0
100513A	4.772	13.92	1.40	5.91	9	7	-4.1	-4.8
100621A	0.542	0.96	21.00	1.58	4	20	-5.0	-5.8
100704A	3.6	9.95	6.00	16.23	6	9	-5.1	-5.5
100814A	1.44	3.23	9.00	4.85	6	9	-5.0	-5.6
100906A	1.727	4.05	12.00	9.09	3	20	-5.2	-5.9
110808A	1.348	2.98	0.33	0.16	3	3	-3.6	-5.2
110818A	3.36	9.16	4.00	9.67	20	1	-5.3	-5.5
111008A	4.9898	14.68	5.30	23.95	3	9	-5.5	-6.1
111228A	0.72	1.36	8.50	1.15	5	8	-4.8	-5.7

Table 2.1: Properties of X-ray Sample (Continued)

GRB	z	d_{L28}	Fluence $[\times 10^{-6}$ ergs/cm$^2]$	$E^{\gamma}_{\rm iso,52}$	$t_{2,\rm EoSD}$	$f_{\rm 1keV,EoSD}$ μJy	$\log_{10}(\epsilon_B)$ $s=0$	$\log_{10}(\epsilon_B)$ $s=2$

Table 2.1: This table displays the properties of our X-ray sample. The GRBs that are in bold are also part of our optical sample. The second and third columns show the redshift and the luminosity distance d_L (in units of 10^{28} cm), respectively. The fourth column shows the fluence detected by BAT in units of 10^{-6}ergs/cm^2. The next column shows $E^{\gamma}_{\rm iso,52}$, the isotropic equivalent energy released in gamma-rays during the prompt emission, in units of 10^{52} ergs. $t_{2,\rm EoSD}$ represents the time at the end of the steep decline (EoSD) in units of 10^2 seconds. The column $f_{\rm 1keV,EoSD}$ shows the specific flux at 1 keV at the end of the steep decline, in units of μJy. The last two columns show the upper limits on ϵ_B, assuming $p = 2.4$. One column shows the results for a constant density medium ($s = 0$) assuming $n = 1$ cm^{-3} (filled-in histogram in the Top-Right panel of Figure 2.2) and the other column shows the results for a wind medium ($s = 2$) assuming $A_* = 0.1$ (un-filled histogram in the Top-Right panel of Figure 2.2).

2.4.4 Expected External-Forward Shock Emission At The End Of The Steep Decline

The synchrotron afterglow spectrum consists of four power-law segments that are smoothly joined together at three characteristic frequencies of synchrotron emission (e.g. Sari, Piran, & Narayan, 1998; Granot & Sari, 2002). These three characteristic frequencies are: ν_a, the synchrotron self-absorption frequency, ν_i (also commonly referred to as ν_m), the frequency of the photons emitted by the power-law distribution of injected electrons with the smallest energy, and ν_c, the cooling frequency corresponding to electrons cooling on a dynamical time. For this work, we will only consider the standard case for the ordering of the characteristic frequencies, the slow cooling case, where

$\nu_a < \nu_i < \nu_c$. One argument against the fast cooling case ($\nu_a < \nu_c < \nu_i$) is that if the observing frequency is between ν_c and ν_i, the spectrum should be $f_\nu \propto \nu^{-1/2}$; however, the spectral index $\beta = 0.5$ disagrees with the typical observed afterglow spectral index $\beta \approx 0.9$ (e.g. Piro, 2001). The next question we need to consider is where the X-ray band lies at the end of the steep decline (here, we consider 1 keV for the X-ray band because the light curves we used are plotted at this energy). The two possibilities for the spectral regime of the X-ray band are $\nu_i < 1$ keV $< \nu_c$ or $\nu_c < 1$ keV. We rule out $\nu_c < 1$ keV with the following two arguments.

First, we compare the observed flux at the end of the steep decline, $f_{\rm 1keV,EoSD}$, to the flux predicted by the external-forward shock at the same time, if $\nu_c < 1$ keV (defined as $f_{\rm pred}$). For $s = 0$, $f_{\rm pred}$ is given by (Granot & Sari, 2002)

$$\begin{aligned} f_{\rm pred} &= 0.855(p-0.98)10^{\frac{3p+2}{4}}8.64^{\frac{3p-2}{4}}e^{1.95p} \\ &\times(1+z)^{\frac{p+2}{4}}(\bar{\epsilon}_{e,-1})^{p-1}\epsilon_B^{\frac{p-2}{4}}E_{53}^{\frac{p+2}{4}}(t_{2,\rm EoSD})^{-\frac{(3p-2)}{4}} \\ &\times d_{L28}^{-2}\nu_{14}^{-\frac{p}{2}}\ {\rm mJy}\ , \end{aligned} \tag{2.6}$$

where $\bar{\epsilon}_{e,-1} \equiv (p-2)/(p-1)\epsilon_{e,-1}$. For $\nu_c < 1$ keV, the external-forward shock flux is independent of the density and the $s = 2$ expression is almost identical. When calculating $f_{\rm pred}$, for each of the bursts in our X-ray sample, we assumed a standard $p = 2.4$, $\epsilon_e = 0.2$, and $\nu_{14} = 2.4 \times 10^3$, the frequency corresponding to 1 keV. For the parameters E, t, z, and d_L, we used the values given in Table 2.1 for each burst ($E = 5E_{iso}^{\gamma}$). The remaining parameter we need to compute

$f_{\rm pred}$ is ϵ_B. Since ϵ_B is raised to the power of $(p-2)/4$, for a typical $p \sim 2-3$, the dependence on ϵ_B is very weak. When calculating $f_{\rm pred}$, we assumed a low value of $\epsilon_B = 10^{-3}$.

We computed the ratio $f_{\rm pred}/f_{\rm 1keV,EoSD}$ for all the GRBs in our X-ray sample and found that $f_{\rm pred}/f_{\rm 1keV,EoSD} > 1$ for all the bursts and $f_{\rm pred}/f_{\rm 1keV,EoSD} > 10$ for 54/60 bursts. The mean value of $f_{\rm pred}/f_{\rm 1keV,EoSD}$ is 50 and the median value is 34. This means that the predicted flux from the external-forward shock, when $\nu_c < 1$ keV, over-predicts the observed flux at the end of the steep decline by a factor that is larger than 10 for the majority of the bursts. Therefore, the assumption that $\nu_c < 1$ keV is incorrect. This is a robust conclusion because the X-ray flux from the external-forward shock, when $\nu_c < 1$ keV, basically only depends on $\sim \epsilon_e E$ (see Equation 2.6), which cannot be decreased by a factor of > 10 without introducing serious efficiency problems in producing the prompt gamma-rays. Even if we allow for an uncertainty of a factor of $\sim 2-3$ in both ϵ_e and E, this is not enough to decrease $f_{\rm pred}/f_{\rm 1keV,EoSD}$ below 1 for the majority of bursts in our X-ray sample.

Before continuing, we want to add that $f_{\rm pred}$ (Equation 2.6) also has a dependence on the Compton-Y parameter: $f_{\rm pred} \propto (1+Y)^{-1}$. With this dependence, if the Compton-Y parameter is large, then it is possible for $f_{\rm pred}$ to decrease below $f_{\rm 1keV,EoSD}$. For a few bursts in our X-ray sample, we performed a detailed numerical calculation of the external-forward shock flux with the formalism presented in Barniol Duran & Kumar (2011), which includes a detailed treatment of Compton-Y with Klein-Nishina effects. From this calcu-

lation, we also found that $f_{\rm pred}$ over-predicts $f_{\rm 1keV,EoSD}$ by a factor larger than 10, which means that the Inverse Compton (IC) cooling of electrons producing 1 keV synchrotron photons is a weak effect (even when ϵ_B is small). Numerically, we also found that without making any assumption about the location of ν_c, solutions to the constraint $f_{\rm ES,1keV} \leq f_{1keV,EoSD}$ were only found when 1 keV $< \nu_c$ (when ϵ_B is small such that 1 keV $< \nu_c$, it turns out that IC cooling of electrons producing 1 keV photons takes place in the Klein-Nishina regime at these early times of $\sim$ few $\times$100 sec).

Another argument in favor of the spectral regime of the X-ray band being $\nu_i < 1$ keV $< \nu_c$ at the end of the steep decline comes from the extrapolation of ν_c at late times to the end of the steep decline. In Liang et al. (2008), they made fits to late time XRT light curves during the normal decline phase and they also provided the value of ν_c during the geometrical midpoint of the normal decline phase[5]. For this argument, we focus on GRBs that are in common to our X-ray sample and to the sample of Liang et al. (2008). For these bursts, we extrapolate ν_c at late times to the end of the steep decline. In Liang et al. (2008), they only considered a constant density medium, where $\nu_c \propto t^{-1/2}$. The results of the extrapolation of ν_c are shown in Table 2.2. In Table 2.2, we find that at the end of the steep decline, 1 keV $< \nu_{c,\rm EoSD}$ for all GRBs. This further confirms our choice that $\nu_i <$ 1 keV $< \nu_c$ at the end of

[5]The geometrical midpoint of the normal decline is defined by $\log_{10}t = (\log_{10}t_1 + \log_{10}t_2)/2$, where t_1 represents the time of the first observation of the normal decline and t_2 represents the time of the last observation of the normal decline.

GRB	$t_{\rm late,4}$	$t_{\rm EoSD,2}$	$\nu_{\rm c,late}$ (keV)	$\nu_{\rm c,EoSD}$ (keV)
050315	3.5	4	0.17	1.6
050401	6.9	2	4.1	77
051221A	1.7	6	4.1	22
060210	3.2	8	0.97	6.1
060502A	0.42	3	4.1	15
060714	3.5	3	3.6	39
060729	40	6	1.4	36
060814	2.0	8	4.1	21
060926	0.26	2	6.7	24
061121	1.1	2	4.2	31
070110	14	4	4	74

Table 2.2: This table shows the extrapolation of ν_c from late times to the end of the steep decline for GRBs in common to our sample and to the sample in Liang et al. (2008) (first column). The second column shows $t_{\rm late,4}$, the late time in units of 10^4 seconds at which Liang et al. (2008) determined ν_c. The third column shows $t_{\rm EoSD,2}$, the time at the end of the steep decline in units of 10^2 seconds. $\nu_{\rm c,late}$, given in keV, is the value found in Liang et al. (2008) for ν_c at $t_{\rm late}$. The last column shows $\nu_{\rm c,EoSD}$ in keV. $\nu_{\rm c,EoSD}$ is found by extrapolating $\nu_{\rm c,late}$ to $t_{\rm EoSD}$. Since Liang et al. (2008) assume a constant density medium, we take a constant density medium for all the GRBs in this sample when making the extrapolation of ν_c to $t_{\rm EoSD}$.

the steep decline[6].

The knowledge of the spectral regime regime at the end of the steep

[6]Including energy injection will make the values of $\nu_{\rm c,EoSD}$ in Table 2.2 larger, making the conclusion that $\nu_i < 1$ keV $< \nu_c$ at the end of the steep decline more robust. For the bursts that have plateaus in their X-ray light curve, energy injection needs to be considered. During the energy injection episode, E increases as $E \propto t^{1-q}$ (Zhang et al., 2006), where q is a positive constant that satisfies $0 \leq q \leq 1$. Therefore, between the end of the plateau and the end of the steep decline, since $\nu_c \propto E^{-1/2} t^{-1/2}$, $\nu_c \propto t^{-1+(q/2)}$. This time evolution of ν_c is steeper than $\nu_c \propto t^{-1/2}$ without energy injection for $s = 0$ (Liang et al. (2008) only considered $s = 0$).

decline allows us to write in an explicit expression for $f_{\rm ES}$ in Equation 2.3:

$$\frac{f_{\rm 1keV,EoSD}}{\rm mJy} \geq \begin{cases} 0.461(p-0.04)10^{\frac{3p+1}{4}}8.64^{\frac{3(p-1)}{4}}e^{2.53p} \\ \quad \times(1+z)^{\frac{p+3}{4}}(\bar{\epsilon}_{e,-1})^{p-1}\epsilon_B^{\frac{p+1}{4}}n_0^{\frac{1}{2}}E_{53}^{\frac{p+3}{4}} \\ \quad \times(t_{2,\rm EoSD})^{-\frac{3(p-1)}{4}}d_{L28}^{-2}\nu_{14}^{-\frac{(p-1)}{2}} \quad s=0 \\ \\ 3.82(p-0.18)10^{\frac{3p-1}{4}}8.64^{\frac{3p-1}{4}}e^{2.54p} \\ \quad \times(1+z)^{\frac{p+5}{4}}(\bar{\epsilon}_{e,-1})^{p-1}\epsilon_B^{\frac{p+1}{4}}A_{*,-1}E_{53}^{(p+1)/4} \\ \quad \times(t_{2,\rm EoSD})^{-\frac{(3p-1)}{4}}d_{L28}^{-2}\nu_{14}^{-\frac{(p-1)}{2}} \quad s=2. \end{cases} \tag{2.7}$$

On the left hand side of this inequality, we have the observed X-ray flux at the end of the steep decline and on the right hand side we have the expression for the external-forward shock flux when $\nu_i < 1$ keV $< \nu_c$ (Granot & Sari, 2002). The notation used for $\bar{\epsilon}_e$ and A_* is defined as $\bar{\epsilon}_{e,-1} \equiv \bar{\epsilon}_e/10^{-1}$ and $A_{*,-1} \equiv A_*/10^{-1}$. The expressions in Equation 2.7 are only valid for $p > 2$, which we consider in this work (for $p < 2$, see Bhattacharya 2001 and Resmi & Bhattacharya 2008).

Before displaying our results for the ϵ_B upper limit for our entire X-ray sample, we show a simple calculation to get an idea of what values to expect for the ϵ_B upper limits from the X-ray constraint given in Equation 2.7. For a standard $p = 2.4$, the X-ray constraint is

$$\frac{f_{\rm 1keV,EoSD}}{\rm mJy} \geq \begin{cases} 5.0\times10^{1}t_{2,\rm EoSD}^{-1.05}\epsilon_{e,-1}^{1.4}E_{53}^{1.35}n_0^{0.5}\epsilon_B^{0.85} & s=0 \\ \\ 7.0\times10^{2}t_{2,\rm EoSD}^{-1.55}\epsilon_{e,-1}^{1.4}E_{53}^{0.85}A_{*,-1}\epsilon_B^{0.85} & s=2. \end{cases} \tag{2.8}$$

For this calculation, we used the average $z = 2.5$ for *Swift* GRBs (Gehrels et al., 2009) (with a corresponding $d_{L28} = 6.4$) and ν_{14} corresponding to 1

keV. Solving for ϵ_B, the upper limit depends on the afterglow parameters as[7]

$$\epsilon_B \leq \begin{cases} 1.0 \times 10^{-2} \left(\frac{f_{1keV,\mathrm{EoSD}}}{\mathrm{mJy}}\right)^{1.18} t_{2,\mathrm{EoSD}}^{1.24} & \\ \quad \times \epsilon_{e,-1}^{-1.65} E_{53}^{-1.59} n_0^{-0.59} & s = 0 \\ & \\ 4.5 \times 10^{-4} \left(\frac{f_{1keV,\mathrm{EoSD}}}{\mathrm{mJy}}\right)^{1.18} t_{2,\mathrm{EoSD}}^{1.82} & \\ \quad \times \epsilon_{e,-1}^{-1.65} E_{53}^{-1} A_{*,-1}^{-1.18} & s = 2. \end{cases} \tag{2.9}$$

The median values for our X-ray sample for the parameters $f_{1\mathrm{keV,EoSD}}$, $t_{2,\mathrm{EoSD}}$, and E_{53} are 8×10^{-3} mJy, 4, and 1.6, respectively. Using these median values and $\epsilon_{e,-1} = 2$, the upper limit on ϵ_B becomes

$$\epsilon_B \leq \begin{cases} 2.8 \times 10^{-5} \times n_0^{-0.59} & s = 0 \\ & \\ 3.7 \times 10^{-6} \times A_{*-1}^{-1.18} & s = 2. \end{cases} \tag{2.10}$$

For a standard $n_0 = 1$ and $A_{*,-1} = 1$, it can be seen that the ϵ_B upper limit is lower for $s = 2$. This is expected because for $A_{*,-1} = 1$, there is a larger density for the surrounding medium within a typical deceleration radius of 10^{17} cm.

In Equation 2.10, the explicit dependence of the ϵ_B upper limit on the density is shown for $p = 2.4$. In the next subsection, we will display the results of the ϵ_B upper limits for our entire X-ray sample. To keep the density-dependence, we will display histograms of upper limits on the quantity $\epsilon_B n_0^{0.59}$

[7]For bursts with plateaus in their X-ray light curve, it is possible that energy injection begins before the steep decline ends. However, even with energy injection, there still exists a self-similar solution for the energy (Equation 52 of Blandford & McKee 1976). For both $s = 0$ and $s = 2$, we calculated the external-forward shock synchrotron flux with this new self-similar solution and then calculated the upper limit on ϵ_B as shown in Equation 2.9. We found that the ϵ_B upper limits are affected by less than a factor of ~ 2. Thus, even if energy injection begins before the end of the steep decline, it has very little to no effect on our ϵ_B upper limit results.

($\epsilon_B A_{*-1}^{1.18}$) for $s = 0$ ($s = 2$) for $p = 2.4$, or $\epsilon_B n_0^{2/(p+1)}$ ($\epsilon_B A_{*-1}^{4/(p+1)}$) for $s = 0$ ($s = 2$) for a general p (see Equation 2.7).

2.4.5 ϵ_B Upper Limits For Our X-ray Sample

We display the results for the upper limits (from Equation 2.7) on the quantity $\epsilon_B n_0^{2/(p+1)}$ ($\epsilon_B A_{*-1}^{4/(p+1)}$) for $s = 0$ ($s = 2$) assuming all GRBs in our X-ray sample have $p = 2.2$, 2.4, and 2.8 in the Top-Left, Top-Right, and Bottom panels of Figure 2.2, respectively. Two histograms are shown in each panel, one for $s = 0$ and the other for $s = 2$. Table 2.3 shows the mean and median upper limits on the quantity $\epsilon_B n_0^{2/(p+1)}$ ($\epsilon_B A_{*-1}^{4/(p+1)}$) for $s = 0$ ($s = 2$) for each histogram. For the remainder of this section, we assume a standard $n_0 = 1$ ($A_{*-1} = 1$) for $s = 0$ ($s = 2$) when discussing our results for the ϵ_B upper limits.

The ϵ_B upper limit histograms show a wide distribution. For a constant density (wind) medium, all the histograms show a distribution ranging from $\sim 10^{-6} - 10^{-3}$ ($\sim 10^{-7} - 10^{-4}$). For a constant density (wind) medium, the mean and median ϵ_B upper limit values are $\sim$ few $\times 10^{-5}$ ($\sim$ few $\times 10^{-6}$). Assuming a different value of p does not have a significant effect on the distributions of the ϵ_B upper limits for our X-ray sample. For both the $s = 0$ and $s = 2$ cases, when changing p, the mean and median ϵ_B upper limit values change by less than a factor ~ 2. Although previous afterglow studies also showed a wide distribution for ϵ_B (Figure 2.1), our distribution of ϵ_B upper limits is shifted towards lower values. Unlike Figure 2.1, which shows that many GRBs have

been reported to have $\epsilon_B \sim 10^{-3} - 10^{-1}$, none of our histograms of ϵ_B upper limits show an ϵ_B upper limit larger than 10^{-3}.

We now discuss how our assumptions on the afterglow parameters can affect the distribution of ϵ_B upper limits. For this discussion, we will take a typical $p = 2.4$; Equation 2.9 shows how the ϵ_B upper limit depends on the other afterglow parameters. The strongest dependence is on ϵ_e, which is raised to the power of -1.65. However, as we displayed in Figure 2.1, according to previous studies, the distribution of ϵ_e values is narrow, with the ϵ_e values ranging only over one order of magnitude. In addition, $\sim 62\%$ of the bursts have $\epsilon_e \sim 0.1 - 0.3$. From Figure 2.1, a likely error in ϵ_e from our assumed $\epsilon_e = 0.2$ is a factor ~ 2. From Equation 2.9, an error in ϵ_e by a factor ~ 2 will only lead to an error in the ϵ_B upper limit by a factor ~ 3. For a constant density (wind) medium, the ϵ_B upper limit depends on E as $E^{-1.59}$ (E^{-1}). We assumed an efficiency of $\sim 20\%$ in the conversion of kinetic energy to prompt gamma-ray radiation. Recent studies have found higher values for the efficiency (Granot et al. 2006, Zhang et al. 2007a, see however, Fan & Piran 2006). In Zhang et al. 2007a, the mean (median) efficiency they reported is $\sim 37\%$ ($\sim 32\%$). Taking the efficiency to be $\sim 30\% - 40\%$ instead of $\sim 20\%$ would lead to an error in E by a factor $\sim 2 - 3$. From Equation 2.9, an error in E by a factor $\sim 2 - 3$ would lead to an error in the ϵ_B upper limit by a factor $\sim 3 - 6$ ($\sim 2 - 3$) for a constant density (wind) medium. Lastly, the largest source of uncertainty for the ϵ_B upper limits is the density, since it has been reported to have a range $\sim 10^{-3}$ cm$^{-3} - 10^{2}$ cm^{-3}. For a constant

density (wind) medium, the ϵ_B upper limit depends on the density as $n^{-0.59}$ ($A_*^{-1.18}$). For $s = 0$ ($s = 2$), we assumed a standard $n = 1$ cm^{-3} ($A_* = 0.1$). An error in the density by a factor $\sim 10^3$ ($\sim 10^2$) will lead to an error in the ϵ_B upper limit by a factor ~ 60 (~ 230).

In summary, the expected errors in ϵ_e and E of a factor $\sim 2-3$ will not change the ϵ_B upper limits by an order of magnitude. On the other hand, the density is a very uncertain parameter and an error in the density by $\sim 2-3$ orders of magnitude will lead to an error in the ϵ_B upper limits by $\sim 1-2$ orders of magnitude.

Two additional parameters that can affect our ϵ_B upper limits are: 1. ξ, the fraction of electrons accelerated to a power-law distribution and 2. f, which is a factor that takes into account the degeneracy for a set of afterglow parameters. For a set of parameters E, n, ϵ_e, ϵ_B, ξ producing the observed external-forward shock flux, another set of primed parameters $E' = E/f$, $n' = n/f$, $\epsilon'_e = f\epsilon_e$, $\epsilon'_B = f\epsilon_B$, $\xi' = f\xi$ can also produce the observed external-forward shock flux (Eichler & Waxman, 2005). Afterglow studies usually assume $\xi = f = 1$ for simplicity but $\xi \leq 1$ and $m_e/m_p \leq f \leq 1$ (Eichler & Waxman, 2005), where m_e (m_p) is the electron (proton) mass. The external-forward shock flux depends on ξ and ϵ_B as $f_\nu \propto \xi^{2-p}\epsilon_B^{(p+1)/4}$ (Leventis et al., 2012). From this dependence, we find that the ϵ_B upper limit $\propto \xi^{4(p-2)/(p+1)}$. Thus, including ξ will decrease the values of our ϵ_B upper limits. Values of ξ have not been determined for GRB external-forward shocks so we cannot quantify by how much the ϵ_B upper limit values will decrease.

Including f will also decrease the values of the ϵ_B upper limits since $\epsilon'_B = f\epsilon_B$ and $f < 1$. Like ξ, values of f have also not been determined from afterglow observations. The largest effect f can have on the ϵ_B upper limit values is decrease them by a factor of $m_p/m_e \sim 2000$. For the remainer of this paper, we will be conservative and continue to assume $\xi = f = 1$, but we should keep in mind that considering ξ and f will decrease the values of the ϵ_B upper limits.

2.5 Measurement Of ϵ_B With Optical Light Curves

2.5.1 ϵ_B Determination With Optical Data

The light curves we consider for our optical sample decline with a temporal decay index $\alpha \sim 1$ from early times, $\sim 10^2 - 10^3$ sec, as expected for the external-forward shock emission (see Section 2.5.2). Since the light curves of these bursts are likely dominated by the external-forward shock, this means that the observed optical flux is an actual measurement of the external-forward

shock flux, that is[8]

$$f_{\rm obs} = f_{\rm ES}(E, n, \epsilon_e, \epsilon_B, p, s). \tag{2.11}$$

Later in this section we will use this condition to determine ϵ_B for the bursts in our optical sample. We want to stress that we determine ϵ_B for the optical sample. This is in contrast to the X-ray sample, which only allowed us to determine an upper limit on ϵ_B.

2.5.2 The Optical Sample

Our optical sample consists of 35 GRBs. 33/35 of the bursts triggered *Swift* and the remaining two bursts, 050502A and 080603A, were detected by INTEGRAL (INTErnational Gamma-Ray Astrophysics Laboratory, Winkler et al. 2003). Table 2.4 shows properties of our optical sample. With a few exceptions, most of the GRBs in our optical sample have a known redshift[9].

[8] At late times, $\sim 10^3 - 10^5$ sec, many X-ray light curves decline with $\alpha \sim 1$: the "normal" decline. If this segment arises from the external-forward shock, then ϵ_B can be determined as described in this Section for our optical sample. However, this is not straightforward since energy injection (as evidenced by the plateau phase) should be considered. Also, one can attempt to use the upper limit on ϵ_B, found in Section 2.4, to calculate a lower limit on ν_c during the normal decline and compare this to the observed spectral regime (1 keV $< \nu_c$ or 1 keV $> \nu_c$). However, there are two difficulties with this ν_c consistency check: 1. several "closure relations" are simultaneously satisfied within 2-σ for most of our sample (due to large errors in the spectral and temporal indices at late times, which can be found in Evans et al. (2007, 2009)). 2. for the bursts that uniquely satisfy one closure relation, ν_c cannot be determined precisely since Klein-Nishina suppression is weaker at late times and ν_c depends strongly on n when Compton-Y is considered.

[9] The redshifts were taken from NASA's *Swift* GRB Table and Lookup website (exceptions are GRB 071003 (Perley et al., 2008) and GRBs 050502A and 071025 (J. Greiner's website)). Three GRBs (050721, 070420, 060111B) in our optical sample do not have a known redshift. For GRB 050721 and GRB 070420, we assumed the average redshift of 2.5 for *Swift* GRBs (Gehrels et al., 2009). The redshift for GRB 060111B was approximated as 2 in Stratta et al. (2009).

Table 2.4: Optical Sample Properties

GRB	z	d_{L28}	Fluence $[\times 10^{-6}$ ergs/cm$^2]$	$E^{\gamma}_{\rm iso,52}$	α_O	Ref.	t_2	$f_{2\rm eV}$ [mJy]	$\log_{10}(\epsilon_B)$ $(s=0)$
050401	2.9	7.67	8.22	15.55	0.80 ± 0.03	[1]	0.72	0.3	-5.5
050502A	3.793	10.59	1.4	4.12	1.16 ± 0.03	[2]	1	5	-4.5
050525A	0.606	1.10	15.3	1.45	1.12 ± 0.05	[3]	34.56	0.5	-4.3
050721	2.5	6.40	3.62	5.32	1.29 ± 0.06	[4]	20	0.2	-5.0
050730	3.97	11.19	2.38	7.53	0.89 ± 0.05	[17]	7.5	0.57	-3.9
050802	1.71	4.00	2.00	1.49	0.82 ± 0.03	[1]	3.6	0.5	-3.5
051111	1.55	3.54	4.08	2.52	1.00 ± 0.02	[2]	30	0.4	-3.8
051221A	0.5465	0.97	1.15	0.09	0.96 ± 0.03	[5]	100	0.02	-3.4
060111B	2	4.86	1.60	1.58	1.18 ± 0.05	[6]	2	0.4	-5.2
060210	3.91	10.99	7.66	23.65	1.03 ± 0.06	[2]	10	0.1	-6.0
060418	1.49	3.37	8.33	4.78	1.13 ± 0.02	[7]	2	8	-4.6
060607A	3.082	8.25	2.55	5.34	1.20 ± 0.03	[7]	2	10	-4.2
060904B	0.703	1.32	1.62	0.21	1.00 ± 0.18	[17]	5.5	0.58	-3.5
060908	2.43	6.18	2.80	3.91	$1.05^{+0.03}_{-0.03}$	[8]	2	2	-4.5
060927	5.6	16.81	1.13	6.08	1.21 ± 0.06	[2]	0.5	2	-5.5
061007	1.26	2.74	44.4	18.48	1.70 ± 0.02	[7]	2	50	-6.0
061110B	3.44	9.42	1.33	3.34	1.64 ± 0.08	[2]	20	0.02	-5.9
061121	1.314	2.88	13.7	6.19	0.82 ± 0.02	[7]	4	0.5	-4.7
061126	1.159	2.47	6.77	2.39	0.89 ± 0.02	[2]	10	0.2	-4.6
070318	0.84	1.65	2.48	0.46	0.96 ± 0.03	[7]	20	0.2	-3.7
070411	2.954	7.84	2.70	5.27	0.92 ± 0.04	[2]	20	0.07	-4.7
070420	2.5	6.40	14.0	20.56	0.81 ± 0.04	[2]	3	0.8	-4.7
070714B	0.92	1.85	0.72	0.16	0.83 ± 0.04	[2]	10	0.03	-3.7
071003	1.6	3.69	8.3	5.45	1.466 ± 0.006	[9]	0.6	20	-5.7
071025	5.2	15.41	6.5	31.26	1.27 ± 0.04	[10]	20	0.02	-6.8
071031	2.692	7.00	0.9	1.5	0.97 ± 0.06	[11]	10.5	0.4	-3.4
071112C	0.823	1.61	3.00	0.53	0.95 ± 0.02	[12]	10.5	0.003	-6.3
080603A	1.688	3.94	1.1	0.80	0.99 ± 0.07	[13]	30	0.1	-3.6
080607	3.036	8.10	24.0	49.04	1.65	[14]	3	0.2	-8.0
080721	2.591	6.68	12.0	18.74	1.22 ± 0.01	[5]	3	10	-5.0
080810	3.35	9.13	4.60	11.06	1.23 ± 0.01	[7]	3	30	-3.9
080913	6.7	20.72	0.56	3.92	1.03 ± 0.02	[15]	10	0.02	-5.2
081008	1.967	4.76	4.30	4.13	0.96 ± 0.03	[16]	2	3	-4.1
090313	3.375	9.21	1.40	3.41	1.25 ± 0.08	[17]	20	2	-3.4
090418A	1.608	3.71	4.60	3.05	1.21 ± 0.04	[7]	2	0.8	-5.5

Table 2.4: Optical Sample Properties (Continued)

GRB	z	d_{L28}	Fluence [$\times 10^{-6}$ ergs/cm^2]	$E^{\gamma}_{\rm iso,52}$	α_O	Ref.	t_2	$f_{2\rm eV}$ [mJy]	$\log_{10}(\epsilon_B)$ ($s=0$)

Table 2.4: The bursts in bold are also part of our X-ray sample and the two bursts in italics were detected by INTEGRAL, instead of *Swift*. The redshift and the corresponding luminosity distance in units of 10^{28} cm, d_{L28}, are shown in the second and third columns, respectively. The fluence, in units of 10^{-6}ergs/cm^2, is shown in the fourth column. In the next column we show the isotropic equivalent energy released in gamma-rays during the prompt emission in the units of 10^{52} ergs, $E^{\gamma}_{\rm iso,52}$. The temporal decay of the optical light curve, α_O, is shown in the sixth column. The reference where we found each optical light curve and α_O is shown in the seventh column. The time in units of 10^2 seconds, and the flux in mJy of the data point we used to determine ϵ_B are shown in the next two columns. For 050730 and 060904B, we display the time and flux at the peak of the optical light curve that are given in Melandri et al. (2010) (we could not find a optical light curve in units of specific flux in the literature for these two bursts). In the last column we show the ϵ_B measurements for $n = 1$ cm^{-3} and p determined from α_O (See Bottom-Right panel of Figure 2.3). References for light curves and α_O: [1] = Panaitescu et al. (2006) [2] = Melandri et al. (2008) [3] = Panaitescu (2007) [4] = Antonelli et al. (2006) [5] = Schulze et al. (2011) [6] = Stratta et al. (2009) [7] = Panaitescu & Vestrand (2011) [8] = Covino et al. (2010) [9] = Perley et al. (2008) [10] = Perley et al. (2009) [11] = Krühler et al. (2009) [12] = Uehara et al. (2010) [13] = Guidorzi et al. (2011) [14] = Perley et al. (2011) [15] = Greiner et al. (2009) [16] = Yuan et al. (2010) [17] = Melandri et al. (2010).

With the exception of the only short GRB in our optical sample, GRB 051221A, all the optical light curves in our sample decline before 3500 seconds. Considering early times has the advantage of minimizing possible energy injection. Our optical sample can be separated into 4 different subgroups, depending on the temporal behavior of the light curve before the $\alpha \sim 1$ decay as follows.

1. Light Curves With A Peak At Early Times: The light curves of this subgroup are characterized by a power law rise, reaching a peak, and then a power law decline with $\alpha_O \sim 1$ ($\sim$43% of our sample). The peak of the light curve is believed to be due to the deceleration time. For the bursts in this subgroup, we show the temporal decay of the optical light curve after the peak and the flux and the time of the second data point after the peak in Table 2.4. We take the second data point to be confident that the optical light curve is declining.

2. Single Power Law Decay From Early Times: In this subgroup, the optical light curve shows a decline as a single power law with $\alpha \sim 1$ from the beginning of the observations ($\sim$ 40% of our sample). We display the temporal decay of the optical light curve and the time and the flux of the second data point observed in Table 2.4.

3. Optical Light Curves With Plateaus At Early Times: The optical light curves of 3 bursts in our optical sample (GRBs 050525A, 060210, and 070411) display plateaus at early times. The plateaus in our optical sample are short, with the longest plateau lasting under 3500 seconds. After the plateau ends, the light curves of these 3 bursts show a decay $\alpha_O \sim 1$, as expected for the external forward-shock emission. In Table 2.4, for these 3 bursts, we show the temporal decay after the plateau and the time and the flux of the second data point after the plateau.

4. Light Curves With Possible Reverse Shock Emission At Early Times: 3

GRBs in our optical sample (060111B, 060908, and 061126) show possible emission from the reverse shock. The light curves in this subgroup show an initial steep decline at early times, characteristic of the reverse shock, and then transition to a more shallow decay of $\alpha \sim 1$ that is more typical for the external-forward shock emission. For these GRBs, in Table 2.4 we show the temporal decay of the light curve and the time and flux of the second data point after the possible reverse shock emission.

2.5.3 Optical External-Forward Shock Spectral Regime and Afterglow Parameter Assumptions

When referring to the optical band, we will use 2 eV since most of the light curves in our optical sample are either plotted at 2eV or were observed in the R filter. As we did with the X-ray sample, we will only consider the slow cooling ordering of the synchrotron characteristic frequencies, $\nu_a < \nu_i < \nu_c$. Because the optical light curve is declining at the time we are considering, the optical band must be above ν_i at this time. In Section 2.4.4, we argued that the X-ray band is between ν_i and ν_c at the end of the steep decline at a few 100 sec; therefore, the optical band must also be in this spectral regime at the early times ($\sim 10^2 - 10^3$) sec we are considering. The expression we will use to determine the optical external-forward shock flux is also Equation 2.7; however, we will have an equality (instead of an inequality), we replace $f_{\rm 1keV,EoSD}$ with $f_{\rm 2eV}$ (which represents the specific flux observed at 2 eV), and use ν_{14} corresponding to 2 eV.

The other afterglow parameters are determined as in Section 2.4.2: $\epsilon_e = 0.2$ and with z and the fluence[10], we obtain $E^{\gamma}_{\rm iso}$ and use $E = 5E^{\gamma}_{\rm iso}$. As with our X-ray sample, we will display our ϵ_B results with $p = 2.2$, 2.4, and 2.8. We can also determine p by using the temporal decay of the optical light curve, α_O, which is shown in Table 2.4 for each burst (optical spectrum is not always available, so we cannot use the closure relations for the optical sample). In order to have $p > 2$ for all of the bursts in our optical sample, we only consider a constant density medium when determining p with α_O ($\alpha_O = 3(p-1)/4$ for $s = 0$ and $\alpha_O = (3p-1)/4$ for $s = 2$). Lastly, as we did for our X-ray sample, to keep the density-dependence, we will plot the quantity $\epsilon_B n_0^{2/(p+1)}$ ($\epsilon_B A_{*-1}^{4/(p+1)}$) for $s = 0$ ($s = 2$).

2.5.4 ϵ_B Results For Optical Sample

We display the results for the measurements (from Equation 2.7) on the quantity $\epsilon_B n_0^{2/(p+1)}$ ($\epsilon_B A_{*-1}^{4/(p+1)}$) for $s = 0$ ($s = 2$) assuming all the GRBs in our optical sample have $p = 2.2$, 2.4, and 2.8 in the Top-Left, Top-Right, and Bottom-Left panels of Figure 2.3, respectively. Two histograms are shown in each panel, one for $s = 0$ and the other for $s = 2$. We also use α_O to determine p (assuming $s = 0$) and compare the results to the ones obtained with $p = 2.4$ and $s = 0$ (Bottom-Right panel of Figure 2.3). In Table 2.3, we display a

[10]For the two bursts detected by INTEGRAL, the fluence in Table 2.4 is in the 20-200 keV band of the instrument IBIS (Imager on-Board the INTEGRAL Satellite, Ubertini et al. (2003)): GRB 050502A (Gotz & Mereghetti, 2005) and GRB 080603A (Guidorzi et al., 2011).

summary of the mean and median values of the measurements of the quantity $\epsilon_B n_0^{2/(p+1)}$ ($\epsilon_B A_{*-1}^{4/(p+1)}$) for $s = 0$ ($s = 2$) for each histogram. For the remainder of this section, we assume a standard $n_0 = 1$ ($A_{*-1} = 1$) for $s = 0$ ($s = 2$) when discussing our results for the ϵ_B measurements for our optical sample.

For a constant density (wind) medium, the mean and median ϵ_B measurements are $\sim$ few $\times 10^{-5}$ ($\sim$ few $\times 10^{-6}$) The mean and median ϵ_B measurements only change by a factor of a few when assuming a different value of p. To determine if assuming a standard $p = 2.4$, as opposed to determining p for each burst from α_O, significantly affects the distribution of ϵ_B measurements, we compared the two histograms in the Bottom-Right panel of Figure 2.3 with a Kolmogorov-Smirnov (KS) test. The null hypothesis of the KS test is that the two histograms are drawn from the same distribution. We test this null hypothesis at the 5% significance level. The KS test confirmed the null hypothesis that the two histograms are consistent with being drawn from the same distribution.

As with the ϵ_B upper limits from X-ray data, the mean and median ϵ_B measurements decrease by about an order of magnitude when assuming a wind medium as opposed to a constant density medium. Compared to the distribution of ϵ_B upper limits we attained from X-ray data, the ϵ_B measurements from optical data show a much wider distribution. For a constant density (wind) medium, the ϵ_B measurements range from $\epsilon_B \sim 10^{-8}$–10^{-3} ($\epsilon_B \sim 10^{-9}$–10^{-3}). Also, since we used the same equation (Equation 2.7) to find both the upper limits on ϵ_B with X-ray data and the ϵ_B measurements with optical data, the

discussion at the end of Section 2.4.5 on how the uncertainty in the afterglow parameters and the parameters ξ and f can affect the distribution of ϵ_B upper limits also applies to the distributions of ϵ_B measurements we presented in this section. In addition, since ξ and f are less than unity, including these two parameters will mean that our ϵ_B measurements are effectively upper limits on ϵ_B.

2.5.5 Comparison Of Our Results On ϵ_B To Previous Studies

We performed a KS test between our optical ϵ_B measurements and the results from previous studies on ϵ_B (Figure 2.1). For our ϵ_B results, we used the optical ϵ_B measurements with $n = 1$ cm^{-3} and p determined from α_O (filled-in histogram in Bottom-Right panel of Figure 2.3; the ϵ_B values are shown in Table 2.4). The result of the KS test is that the null hypothesis is rejected. The P-value, which measures the probability that the null hypothesis is still true, is 2.1×10^{-9}. This result shows that the rejection of the null hypothesis is statistically significant. It is not surprising that the null hypothesis was rejected. The distribution from the previous studies is very inhomogeneous, with the values for ϵ_B being drawn from many different studies with different methodologies. Also, comparing the histogram in Figure 2.1 to the filled-in histogram in the Bottom-Right panel of Figure 2.3, a couple of significant differences can be seen. The range for the histogram of ϵ_B values found in the literature is $\sim 10^{-5}-10^{-1}$, whereas the range for our ϵ_B results is $\sim 10^{-8}-10^{-3}$. The mean and median values for these two histograms are also significantly

different. The mean (median) value for the ϵ_B histogram from the literature, 6.3×10^{-2} (1.4×10^{-2}), is a factor $\sim$ 700 ($\sim$ 600) times larger than the mean (median) ϵ_B value of the histogram with our results, which is 9.5×10^{-5} (2.4×10^{-5}).

One assumption that is commonly made in afterglow modeling studies is equipartition between ϵ_e and ϵ_B. As we discussed in Section 2.3, the results for ϵ_e from the literature and the results from recent simulations of relativistic collisionless shocks support $\epsilon_e \sim 0.2$. From this result, many works assume $\epsilon_B \sim 10^{-2} - 10^{-1}$. However, there is no physical argument to expect equipartition. Our distribution of ϵ_B upper limits and measurements, although wide, supports that there is no equipartition between electron and magnetic energies because none of the ϵ_B upper limits or measurements in our samples has a value larger than $\epsilon_B \sim$ few $\times 10^{-3}$. Another source of error that can lead to differences in ϵ_B values is differences in the determination of the spectral regime for the optical band. We took it to be between ν_i and ν_c, but it is also possible for the optical band to be above ν_c at late times (e.g. Panaitescu & Kumar, 2002; Cenko et al., 2010). Another source for error is energy injection. We did not consider energy injection as a source of error because only 3/35 of the bursts in our optical sample show plateaus (and these plateaus are short). The X-ray and optical light curves of many bursts show plateaus and in these cases energy injection needs to be considered. Also, errors in our determination of fluxes and times from X-ray and optical light curves can also lead to small errors in ϵ_B. In summary, the main assumption we made when

determining ϵ_B is an efficiency of $\sim 20\%$ in the conversion of kinetic energy to gamma-ray energy, and we did not assume equipartition between ϵ_e and ϵ_B. Different authors have made different assumptions that can have a large effect on the results for ϵ_B.

Lastly, for a few bursts, we checked if our method of determining ϵ_B is consistent with the values determined for ϵ_B with other techniques. GRBs 980519 and 990123, discussed in the afterglow modelling study of Panaitescu & Kumar 2002, have optical light curves that decline as a power-law before the jet-break. The optical band for both of these bursts was determined to be in the spectral regime $\nu_i < 2$ eV $< \nu_c$. Applying our technique to find a ϵ_B measurement for both of these bursts and using the value of n reported in Panaitescu & Kumar 2002 for both of these bursts, we find that these bursts have $\epsilon_B \sim 10^{-5}$, consistent with the results reported in Panaitescu & Kumar 2002 for both of these bursts within a factor of a few. The small differences in ϵ_B values can be accounted for by differences in the coefficients used for the external-forward shock flux.

2.6 GRBs In Common To Both Our X-ray And Optical Samples

14 bursts we considered are both in our X-ray and in our optical sample (GRB number is in bold in the first columns of Tables 2.1 and 2.4). In this section, we verify for these bursts that the X-ray ϵ_B upper limit is above the optical ϵ_B measurement. For the optical data, we will use the ϵ_B measurements

with p determined from α_O and $n = 1$ cm^{-3} (filled-in histogram in the Bottom-Right panel of Figure 2.3). For the X-ray data, in this section, we will also consider $n = 1$ cm^{-3} ($s = 0$) and we will use the value of p determined from α_O [11]. The comparison between the X-ray ϵ_B upper limits and the optical ϵ_B measurements is shown in Figure 2.4. This plot shows that all the X-ray ϵ_B upper limits are above the optical ϵ_B measurements.

2.7 E vs. ϵ_B Correlation?

We now use the ϵ_B measurements from our optical sample to determine if there is a correlation between E and ϵ_B. The 3 bursts studied in Kumar & Barniol Duran 2009, 2010 have small values of ϵ_B, consistent with shock compression of a seed magnetic field $B_0 \sim$ few $\times 10\mu$G. One property that distinguishes these 3 GRBs is that they were particularly energetic, with $E^{\gamma}_{\rm iso} \sim 10^{53} - 10^{54}$ ergs. Could the large energy intrinsic to these 3 bursts explain why these 3 bursts have low ϵ_B values? We investigate this possibility in Figure 2.5 by plotting the values of E and ϵ_B for all the bursts in our optical sample.

For the energy of each burst, we assumed an efficiency of $\sim 20\%$ ($E = 5E^{\gamma}_{\rm iso}$) in the conversion of the kinetic energy of the jet to gamma-ray radiation; the observables involved in calculating E are the gamma-ray

[11] 10 out of 14 of these bursts have optical data before 1000 seconds. For these 10 bursts, we can use the optical data to check if they satisfy the assumption we made in Section 2.4.1, $t_{\rm dec} < t_{\rm EoSD}$. 9 of these 10 GRBs do satisfy this assumption; for the remaining GRB (080721), we are not able to check this assumption because the first optical observation (at 100 sec.) is after the end of the steep decline ($t_{\rm EoSD} = 70$ sec).

fluence and z. For the ϵ_B measurements, we used the values with p determined from α_O and $n = 1$ cm^{-3}. The observables involved in determining ϵ_B are the observed specific optical flux and the time. In Figure 2.5, we also show the best fit line[12]. This fit shows that an increase in E leads to a decrease in ϵ_B. The correlation coefficient of the fit is 0.62, indicating that there is a weak correlation between E and ϵ_B. A value of the correlation coefficient close to 1 would indicate a strong correlation. The P-value of the correlation is 1.2×10^{-4} (3.8σ significance), indicating that there is a small probability that the correlation occurred by chance.

Although many points show large deviations from the best fit line, the scatter of the points may be reduced or increased by the uncertainty in the afterglow parameters. An error in the efficiency would affect the values of E and an error in ϵ_e, the efficiency, or n would affect the ϵ_B measurements (see Section 2.4.5 for a discussion on how the ϵ_B measurements would be affected when an error in a afterglow parameter is made). It is possible that the uncertainty in E and ϵ_B can reduce or increase the scatter and make the correlation between E and ϵ_B stronger or weaker.

[12]From Equation 2.7, it may be expected that E and ϵ_B are correlated. This is not necessarily true because each burst has a different value for the observed quantities f_ν and t. In addition, since p was determined from α_O, each burst has a different p. We also checked if E and ϵ_B were correlated when assuming a fixed $p = 2.4$. From Equation 2.9, we would expect the slope of the line to be -1.59. The best fitting line for $p = 2.4$ is $\log_{10}(\epsilon_B) = -0.77\log_{10}(E_{53}) - 4.53$, with the slope of the line being -0.77 ± 0.24 and the y-intercept being -4.53 ± 0.16. The slope of this line is more than 3σ away from -1.59, showing that there is no expected correlation between E and ϵ_B for our methodology of determining ϵ_B.

2.8 Magnetic Field Amplification Factor For X-ray And Optical Results

In Sections 2.4-2.6, we presented our results for the strength of the magnetic field downstream of the shock front in terms of the afterglow parameter ϵ_B. If shock compression was the only mechanism amplifying the ambient magnetic field (assuming a standard $B_0 \sim$ few μG and a standard $n = 1$ cm^{-3}), then $\epsilon_B \sim 10^{-9}$ is expected. Most of the bursts in our distributions of ϵ_B upper limits and measurements have values larger than $\epsilon_B \sim 10^{-9}$. These results suggest that amplification of the magnetic field, in addition to shock compression, is needed to explain the afterglow observations. In this section, we will present our results in terms of an amplification factor, which quantifies the amplification that is needed, beyond shock compression, to explain the observations.

If shock compression were the only mechanism amplifying the seed magnetic field B_0, then $B = 4\Gamma B_0$. To quantify how much additional amplification of the ambient magnetic field is needed, beyond shock compression, we define the amplification factor, AF, as

$$AF \equiv \frac{B}{4B_0\Gamma}. \tag{2.12}$$

AF is a constant that satisfies $AF \geq 1$ since $B \geq 4B_0\Gamma$. $AF = 1$ means than the observed B is consistent with the only amplification arising from seed magnetic field shock compression. The expression for ϵ_B is $\epsilon_B = B^2/32\pi m_p c^2 n\Gamma^2$.

With the definition for AF, ϵ_B is

$$\epsilon_B = (AF)^2 \times \frac{B_0^2}{2\pi n m_p c^2}. \tag{2.13}$$

We note that ϵ_B is given by $(AF)^2$ times the ϵ_B we would get if shock compression were the only mechanism amplifying the magnetic field.

We will now use Equation 2.13 and our previous results for the X-ray ϵ_B upper limits to determine an upper limit on AF. In Section 2.4.5, if we assumed a standard $n = 1$ cm^{-3}, we were able to attain an upper limit on ϵ_B for a constant density medium [13]. We will refer to these ϵ_B upper limits as $\overline{\epsilon_B}(p, n_0 = 1)$. In the notation $\overline{\epsilon_B}(p, n_0 = 1)$, the bar over ϵ_B signifies that this is an upper limit on ϵ_B, the p in the parenthesis shows that the ϵ_B upper limit depends on the value of p we used, and the $n_0 = 1$ shows that we assumed $n = 1$ cm^{-3}. With this notation, we can keep the dependence of the ϵ_B upper limit on n (see Equation 2.7):

$$\epsilon_B < \frac{\overline{\epsilon_B}(p, n_0 = 1)}{n_0^{2/(p+1)}}. \tag{2.14}$$

Combining Equation 2.13 and Equation 2.14, the expression for the upper limit on AF is

$$AF < \frac{1.0 \times 10^4 [\overline{\epsilon_B}(p, n_0 = 1)]^{1/2}}{B_{0,10\mu\mathrm{G}} n_0^{(1-p)/(2p+2)}}, \tag{2.15}$$

where $B_{0,10\mu\mathrm{G}} \equiv B_0/10\mu$G. One advantage to expressing the results of the magnetic field downstream of the shock front in terms of AF is that AF

[13] We will only consider a constant density medium when displaying the results for the amplification factor. We will show in Equation 2.15 that AF has a weak dependence on the density.

depends weakly on n. For a standard $p = 2.4$, $AF \propto n^{0.21}$. On the other hand, there is a strong dependence on B_0, $AF \propto B_0^{-1}$.

2.8.1 Amplification Factor Upper Limit For Our X-ray Sample

We will now show the results for the AF upper limits we obtained from Equation 2.15. Since the amplification factor has a weak dependence on the density, we will assume a standard $n_0 = 1$ when displaying the results for the AF upper limits. When plotting the results for AF, we will keep the dependence on B_0 and plot the quantity $(AF)B_{0,10\mu\mathrm{G}}$. In the left and right panels of Figure 2.6, we show the upper limits on the quantity $(AF)B_{0,10\mu\mathrm{G}}$ for a fixed $p = 2.4$ and $p = 2.2$, 2.8, where the values of $\overline{\epsilon_B}(p, n_0 = 1)$ used in Equation 2.15 were shown in Top-Right, Top-Left, and Bottom panels of Figure 2.2, respectively. For the remainder of this section, we will assume $B_0 = 10\mu$G when discussing the results for the AF upper limits.

The mean and median values of the AF upper limits are summarized in Table 2.5. The mean (median) AF upper limits range from $AF \sim 60 - 80$ ($AF \sim 40 - 60$). The AF upper limit histograms show a wide distribution, with a range of ~ 10 to ~ 300. To determine if assuming a different value of p has a significant effect on the distribution of AF upper limits, we performed a KS test between the histograms in the right panel of Figure 2.6. The KS test confirmed the null hypothesis, leading us to conclude that the AF upper limit results are not sensitive to the value of p we assume.

We now discuss how an error in each of the afterglow parameters can

affect our results for the AF upper limits. For this discussion, we will assume $p = 2.4$. From Equation 2.15, AF $\propto \sqrt{\overline{\epsilon_B}(p = 2.4, n_0 = 1)} B_0^{-1} n^{0.2}$ and from Equation 2.9, $\epsilon_B \propto \epsilon_e^{-1.6} E^{-1.6} n^{-0.6}$. From these two expressions, AF $\propto \epsilon_e^{-0.8} E^{-0.8} n^{0.2} B_0^{-1}$. We note that compared to the ϵ_B upper limit (Equation 2.9), the AF upper limit has a weaker dependence on ϵ_e, E, and n. As we discussed at the end of Section 2.4.5, a likely error in ϵ_e is a factor of ~ 2; this error in ϵ_e will translate into an error in the AF upper limits by a factor of only ~ 2. For the energy, we assumed an efficiency $\sim 20\%$ and a likely error in the efficiency is a factor $\sim 2 - 3$ (see Section 2.4.5); this error in the efficiency would lead to an error in the AF upper limits by only a factor ~ 2. One advantage to expressing the results of the magnetic field downstream of the shock front in terms of AF is that AF has a very weak dependence on n. An error in n by a factor $\sim 10^3$ (see Section 2.4.5) from our assumed $n = 1$ cm^{-3} will only lead to an error in the AF upper limits by a factor ~ 4. The price to pay for a weak n dependence is a linear dependence on B_0, with AF $\propto B_0^{-1}$. B_0 is an uncertain parameter that likely varies from GRB environment to GRB environment and it is the largest source of uncertainty for AF.

2.8.2 Amplification Factor Measurement For Our Optical Sample

As we discussed in Section 2.5.2, for our optical sample, we found a measurement for ϵ_B instead of an upper limit. This will allow us to determine a measurement for AF. To do this, we will use Equation 2.15, but in this case we have an equality instead and we have $\epsilon_B(p, n_0 = 1)$ instead of $\overline{\epsilon_B}(p, n_0 = 1)$.

The notation $\epsilon_B(p, n_0 = 1)$ denotes the ϵ_B measurements for our optical sample from Section 2.5.4 if we assume a standard $n = 1$ cm^{-3}. Also, as with the X-ray sample, we only consider $s = 0$ when calculating the AF measurements and assume a fixed $n = 1$ cm^{-3}. In the left panel of Figure 2.7, we show the results for the measurements on the quantity $(AF)B_{0,10\mu\mathrm{G}}$ for p determined from α_O and also assuming $p = 2.4$. In the right panel of Figure 2.7, we show the measurements on the quantity $(AF)B_{0,10\mu\mathrm{G}}$ for $p = 2.2$ and $p = 2.8$. For the remainder of this section, we will assume $B_0 = 10\mu$G when discussing the results for the AF measurements.

A summary of the mean and median AF measurements for our optical sample is shown in Table 2.5. To determine if assuming a standard $p = 2.4$, as opposed to determining p from α_O for each burst, has a statistically significant effect on the distribution of AF measurements, we performed a KS test between the two histograms in the left panel of Figure 2.7. The KS test confirmed the null hypothesis. The mean (median) AF measurements for the optical histograms range from ~ 40 to ~ 130 (~ 20 to ~ 100). Compared to the AF upper limit histograms, the AF measurement histograms show a wider distribution, ranging from $AF \sim 1$ to $AF \sim 1000$. Also, since we used the same expression to determine the AF upper limits and measurements (Equation 2.15), the discussion at the end of Section 2.8.1 on how an error in one of the afterglow parameters can affect the AF upper limits also applies to the AF measurements[14].

[14] ξ and f also affect our AF results. To account for ξ, since the ϵ_B upper

2.9 Discussion And Conclusions

In this work, we presented a systematic study on the magnetic field downstream of the shock front for large samples of GRBs (60 in our X-ray sample and 35 in our optical sample). We expressed the strength of the downstream magnetic field in terms of both the afterglow parameter ϵ_B and a amplification factor, denoted by AF, which quantifies how much amplification, beyond shock compression of the seed magnetic field, is needed to explain the downstream magnetic field. This is the first time a large and systematic study has been carried out to study ϵ_B and to determine how much amplification of the seed magnetic field is required by the observations. For our X-ray (optical) sample, we determined an upper limit (measurement) for both ϵ_B and AF. The upper limits on ϵ_B and AF for our X-ray sample were found from the constraint that the observed flux at the end of the steep decline is greater than or equal to the external-forward shock flux. This is a new method to constrain ϵ_B that relies on the steep decline emission, which has been observed by *Swift* for many GRBs. Our optical sample was restricted to light curves that decline with $\alpha \sim 1$ from the early times $\sim 10^2 - 10^3$ sec, as expected for the external-forward shock emission. We found the measurements for ϵ_B and

limit/measurement is $\propto \xi^{4(p-2)/(p+1)}$ and the AF upper limit/measurement is $\propto (\overline{\epsilon_B}(p, n_0 = 1))^{1/2}$, $AF \propto \xi^{2(p-2)/(p+1)}$. To account for f, since $AF \propto (\overline{\epsilon_B}(p, n_0 = 1))^{1/2}$, $AF \propto f^{1/2}$. Thus, including ξ and f will decrease the values of the AF upper limits/measurements. Taking the lowest possible value for f, the AF upper limits/measurements can decrease by up to a factor ~ 40. This would make $\sim 50\%(\sim 60\%)$ of the bursts in our X-ray (optical) sample consistent with shock compression. In addition, as with the ϵ_B measurements, since ξ and f are less than unity, including these two parameters will mean that our AF measurements will become upper limits on AF.

AF for our optical sample from the condition that the observed flux is equal to the external-forward shock flux.

The condition used for our X-ray (optical) sample was converted into an upper limit (measurement) on the quantity $\epsilon_B n^{2/(p+1)}$ for $s = 0$ or $\epsilon_B A_{*-1}^{4/(p+1)}$ for $s = 2$ by assuming a $\sim 20\%$ efficiency in the conversion of kinetic energy to prompt gamma-ray radiation. To find an upper limit (measurement) on ϵ_B for our X-ray (optical) sample, we assumed a standard $n = 1$ cm^{-3} ($A_* = 0.1$) for the density for a constant density (wind) medium. A discussion on how the uncertainty in the afterglow parameters affects our results for ϵ_B can be found at the end of Section 2.4.5. The largest source of uncertainty for our results on ϵ_B is the density, since the value of the density has been observed to vary over many orders of magnitude and its precise value is not known for each GRB (see Section 2.4.2). For the bursts that are both in our X-ray and optical samples, we also applied a consistency check to make sure our results for ϵ_B are correct (see Section 2.6).

From Table 2.3, for a constant density (wind) medium, most of the ϵ_B upper limit and measurement histograms have a median value $\sim$ few $\times 10^{-5}$ ($\sim$ few $\times 10^{-6}$). These results imply that half of the bursts in both our X-ray and optical samples have a ϵ_B value $\sim$ few $\times 10^{-5}$ or lower. Assuming $n = 1$ cm^{-3} and $B_0 \sim$ few $\times \mu$G, shock compression is only able to produce $\epsilon_B \sim 10^{-9}$. Although $\epsilon_B \sim 10^{-9}$ is 4 orders of magnitude lower than $\epsilon_B \sim 10^{-5}$, $\epsilon_B \sim 10^{-5}$ is smaller by $\sim 2-4$ orders of magnitude compared to the majority of previously reported ϵ_B values (Figure 2.1), which are $\epsilon_B \sim 10^{-3} - 10^{-1}$.

Assuming $B_0 \sim 10\mu$G, $\epsilon_B \sim$ few $\times 10^{-5}$ corresponds to $AF \sim 50$ (Equation 2.15). Our result of a median $\epsilon_B \sim$ few $\times 10^{-5}$ shows that the majority of the bursts in our X-ray and optical samples only require a weak amplification beyond shock compression, by a factor ~ 50 or lower.

The near equipartition $\epsilon_B \sim 0.01 - 0.1$ determined near the shock front by theoretical studies and Particle-In-Cell (PIC) simulations (Medvedev & Loeb, 1999; Chang et al., 2008; Martins et al., 2009; Keshet et al., 2009; Lemoine, 2013; Sironi et al., 2013) stands in contrast with our median results of $\epsilon_B \sim$ few $\times 10^{-5}$. PIC simulations of relativistic collisionless shocks performed by Chang et al. 2008 and Keshet et al. 2009 found that the magnetic field generated near the shock front decays with distance downstream of the shock front. Lemoine 2013 and Lemoine et al. 2013 studied the effects that this decaying magnetic field has on the shock accelerated electrons radiating afterglow emission downstream of the shock front. The main effect is that electrons with different Lorentz factors cool in regions with different magnetic fields, with the higher (lower) energy photons being emitted by electrons that are closer (further) from the shock front (Lemoine et al., 2013). Considering the decay of the downstream magnetic field, Lemoine et al. (2013) modelled the afterglow data of 4 GRBs that have extended emission at energies > 100 MeV (detected by *Fermi*-LAT) and also X-ray, optical, and radio data. Their afterglow modelling results for the X-ray, optical, and radio data found $\epsilon_B \sim 10^{-6} - 10^{-4}$, consistent with our results for the median ϵ_B upper limits and measurements attained from X-ray and optical data.

Our next main result relates to the distribution of ϵ_B values. One property the ϵ_B values from the literature shared with our optical ϵ_B measurements is that they both show a wide distribution. The literature compilation (Figure 2.1) showed $\epsilon_B \sim 10^{-5} - 10^{-1}$ and our optical ϵ_B measurement histograms showed an even wider distribution, ranging from $\epsilon_B \sim 10^{-8} - 10^{-3}$ ($\epsilon_B \sim 10^{-9} - 10^{-3}$) for a constant density (wind) medium. One possibility we investigated to explain the wide distribution of ϵ_B values is whether bursts with smaller ϵ_B values are more energetic than bursts with larger ϵ_B values (Figure 2.5). Although the bursts in our optical sample did show the trend that bursts with larger E have a smaller ϵ_B, the correlation was weak, with a correlation coefficient of 0.62 and a P-value of 1.2×10^{-4} (3.8σ significance).

Another possibility to explain the wide distribution of ϵ_B relates to the uncertainty in the environmental parameters (B_0 and n) in the medium surrounding GRBs. One possibility to explain bursts with values of $\epsilon_B \sim 10^{-5} - 10^{-3}$, under the interpretation of weak amplification beyond shock compression, is that they occurred in environments with particularly high seed magnetic fields. Since $\epsilon_B \propto B_0^2$, an increase in B_0 by an order of magnitude will lead to an increase in ϵ_B by two orders of magnitude. A weak amplification beyond shock compression of $AF \sim 50$ (as inferred for the bursts with $\epsilon_B \sim$ few $\times 10^{-5}$) and a strong $B_0 \sim 10\mu\mathrm{G} - 100\mu\mathrm{G}$ yields $\epsilon_B \sim 10^{-5} - 10^{-3}$ (see Equation 2.15). We note that for this estimate we assumed $n = 1$ cm^{-3}, but as we discussed in Section 2.8, the amplification factor has a weak dependence on the density. This possibility, that the larger values of ϵ_B may be explained by

bursts going off in environments with particularly strong B_0, will be discussed further in Barniol Duran 2013 (in preparation).

In addition to many bursts in our optical sample having particularly large $\epsilon_B \sim 10^{-5} - 10^{-3}$, there were also some bursts in our optical sample that have particularly low ϵ_B values. For p determined from α_O and $n = 1$ cm^{-3} (Bottom-right panel of Figure 2.3), GRBs 071025 and 071112C have $\epsilon_B \sim 10^{-7}$ and GRB 080607 has $\epsilon_B \sim 10^{-8}$. Assuming $n = 1$ cm^{-3} and $B_0 = 10\mu$G, these bursts with $\epsilon_B \sim 10^{-8} - 10^{-7}$ are consistent with shock compression of a seed magnetic field of a few 10 μG being the only amplification necessary to explain the observations.

Lastly, we mention that a similar conclusion for radio observations of supernova remnants (SNRs) was reached in Thompson et al. (2009). Like GRB afterglow emission, SNR emission arises from a blastwave interacting with the surrounding medium, but at non-relativistic speeds. Thompson et al. (2009) found that starburst galaxies have strong ambient magnetic fields ~ 1 mG and they concluded that shock compression of this strong seed magnetic field is enough to explain the radio emission from SNRs. On the other hand, for normal spiral galaxies with ambient magnetic fields $\sim 5 - 10\mu$G, they concluded that additional amplification beyond shock compression by a factor $\sim 3 - 7$ was necessary to explain the radio emission from SNRs.

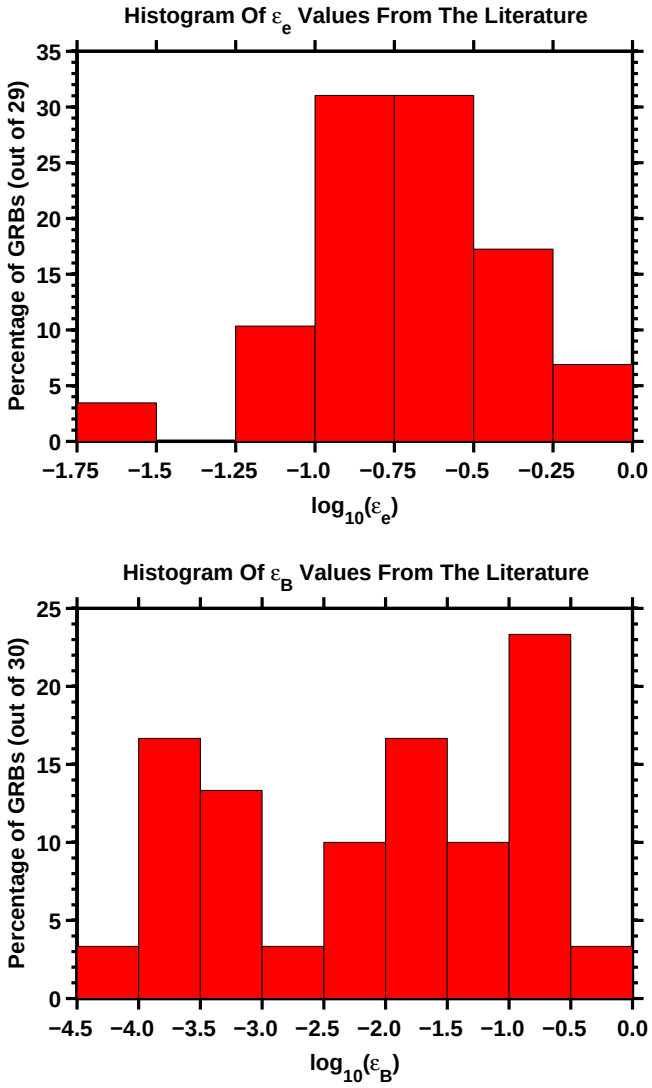

Figure 2.1: *Top Panel:* Histogram of the distribution of ϵ_e values we found in the literature (Table A.1 in Appendix A). *Bottom Panel:* Histogram of the distribution of ϵ_B values we found in the literature (Table A.1 in Appendix A)

X-ray ($s = 0$)	$p = 2.2$	$p = 2.4$	$p = 2.8$	
Mean	1.1×10^{-4}	7.2×10^{-5}	6.1×10^{-5}	
Median	4.2×10^{-5}	2.8×10^{-5}	2.0×10^{-5}	
X-ray ($s = 2$)	$p = 2.2$	$p = 2.4$	$p = 2.8$	
Mean	7.9×10^{-6}	5.5×10^{-6}	5.6×10^{-6}	
Median	4.0×10^{-6}	3.2×10^{-6}	3.4×10^{-6}	
Opt. ($s = 0$)	$p = 2.2$	$p = 2.4$	$p = 2.8$	p from $\alpha_{\rm O}$
Mean	3.5×10^{-4}	1.0×10^{-4}	2.9×10^{-5}	9.5×10^{-5}
Median	1.1×10^{-4}	3.3×10^{-5}	5.5×10^{-6}	2.4×10^{-5}
Opt. ($s = 2$)	$p = 2.2$	$p = 2.4$	$p = 2.8$	
Mean	7.2×10^{-5}	2.4×10^{-5}	7.5×10^{-6}	
Median	1.2×10^{-5}	3.9×10^{-6}	8.8×10^{-7}	

Table 2.3: Mean and median ϵ_B values for the X-ray (upper limits on ϵ_B) and optical (measurements of ϵ_B) histograms shown in Figures 2.2 and 2.3. The section labeled "X-ray ($s = 0$)" ("X-ray ($s = 2$)") shows the mean and median ϵ_B upper limits assuming a constant density (wind) medium with a standard $n = 1$ cm^{-3} ($A_* = 0.1$). The columns show the value of p that was assumed. The section labeled "Opt. ($s = 0$)" ("Opt. ($s = 2$)") shows the mean and median ϵ_B measurements assuming a constant density (wind) medium with a standard $n = 1$ cm^{-3} ($A_* = 0.1$). The columns show the value of p that was assumed. The column labeled "p from α_O" shows the mean and median ϵ_B measurements with p determined from α_O. There are 60 GRBs in our X-ray sample and 35 GRBs in our optical sample.

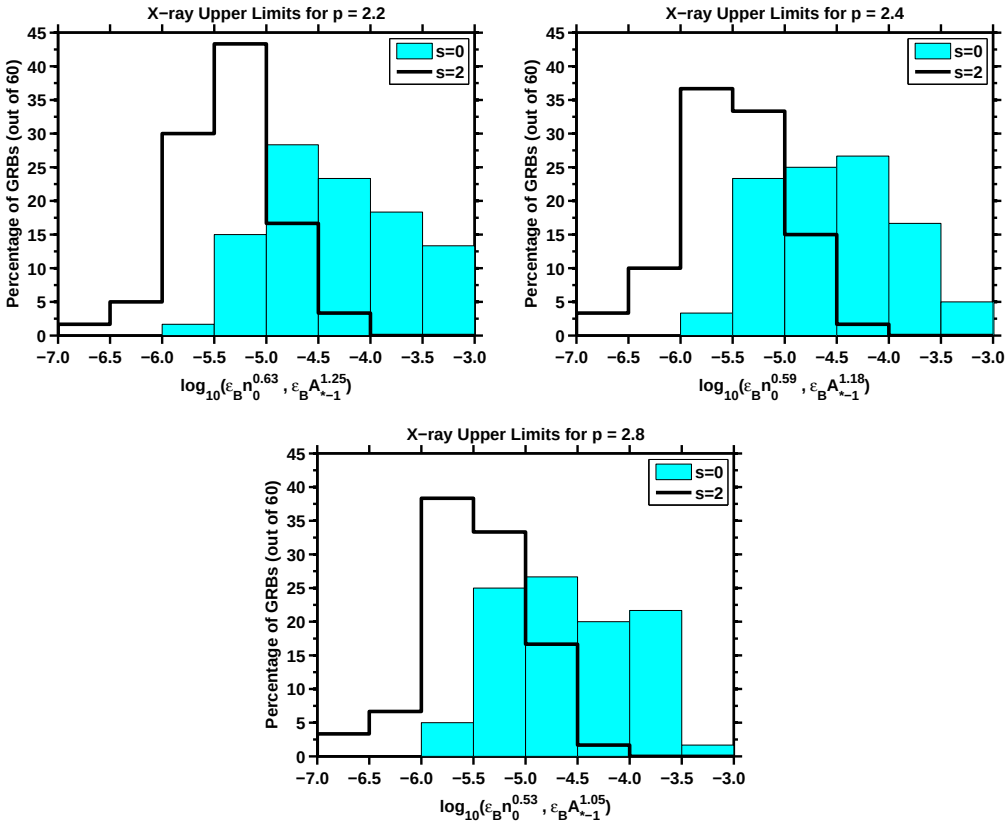

Figure 2.2: The *Top-Left*, *Top-Right*, and *Bottom* panels show the histograms of upper limits assuming $p = 2.2$, $p = 2.4$, and $p = 2.8$ respectively, for all of the GRBs in our X-ray sample (obtained with Equation 2.7). The filled-in (unfilled) histograms show upper limits on the quantity $\epsilon_B n_0^{2/(p+1)}$ ($\epsilon_B A_{*-1}^{4/(p+1)}$) for $s = 0$ ($s = 2$) assuming all the GRBs in our X-ray sample are described by a constant density (wind) medium.

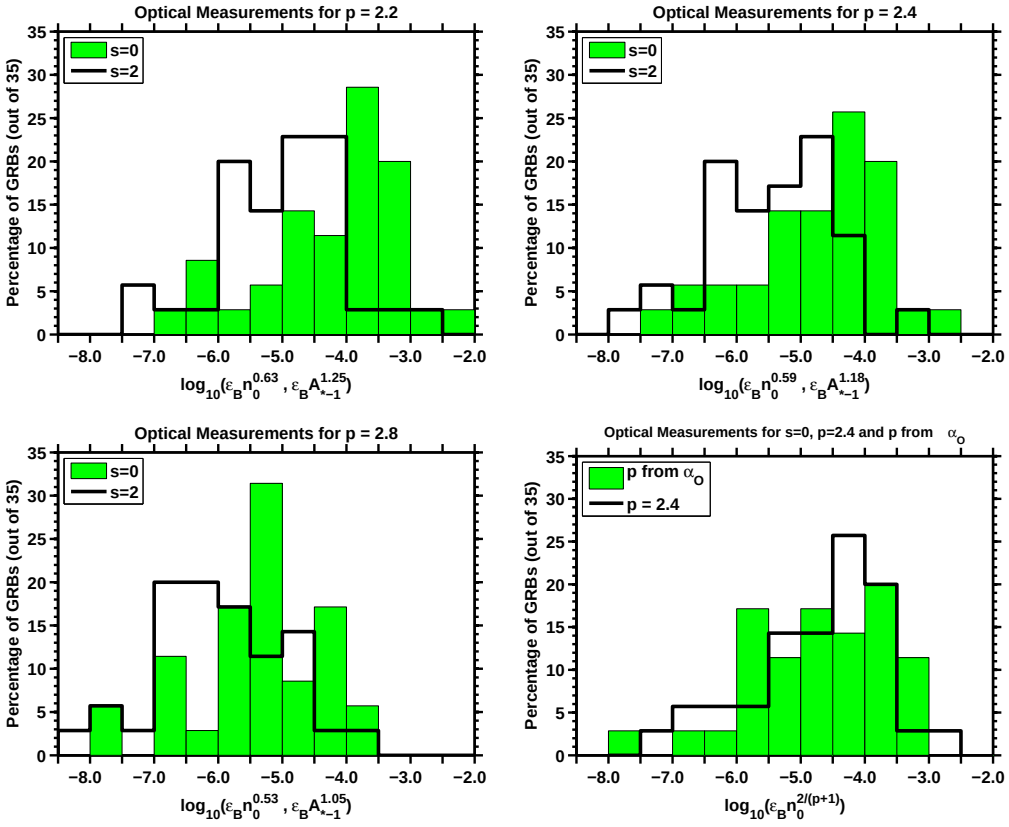

Figure 2.3: The *Top-Left*, *Top-Right*, and *Bottom-Left* panels show the histograms of measurements assuming $p = 2.2$, $p = 2.4$, and $p = 2.8$ respectively for all of the GRBs in our optical sample. The filled-in (un-filled) histograms show measurements of the quantity $\epsilon_B n_0^{2/(p+1)}$ ($\epsilon_B A_{*-1}^{4/(p+1)}$) assuming all the GRBs in our optical sample are described by a constant density (wind) medium. *Bottom-Right Panel:* The filled-in histogram shows the measurements on the quantity $\epsilon_B n_0^{2/(p+1)}$ with p determined from α_O. The un-filled histogram shows measurements on the quantity $\epsilon_B n_0^{2/(p+1)}$, assuming $p = 2.4$ for all of the bursts in our optical sample (this histogram was also shown in the Top-Right panel).

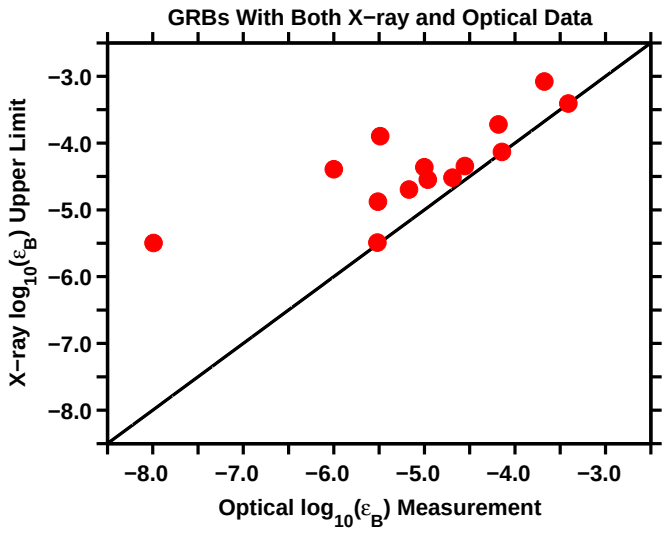

Figure 2.4: Comparison of the ϵ_B upper limits from X-ray data to the ϵ_B measurements from optical data. The 14 dots correspond to the 14 GRBs that are both in our X-ray and optical samples. The straight line indicates where the ϵ_B measurements are equal to the ϵ_B upper limits.

X-ray ($s = 0$)	$p = 2.2$	$p = 2.4$	$p = 2.8$	
Mean	84	67	62	
Median	63	51	44	
Opt. ($s = 0$)	**$p = 2.2$**	**$p = 2.4$**	**$p = 2.8$**	**p from α_O**
Mean	130	71	36	71
Median	100	56	23	48

Table 2.5: Mean and median AF values for the X-ray (upper limits on AF) and optical (measurements of AF) histograms shown in Figures 2.6 and 2.7. All the labels are the same as in Table 2.3. A constant density medium with $n = 1$ cm^{-3} (the amplification factor has a weak dependence on the density, see Section 2.8 and Equation 2.15) and a seed magnetic field $B_0 = 10\mu$G were assumed for all the bursts in our X-ray and optical samples.

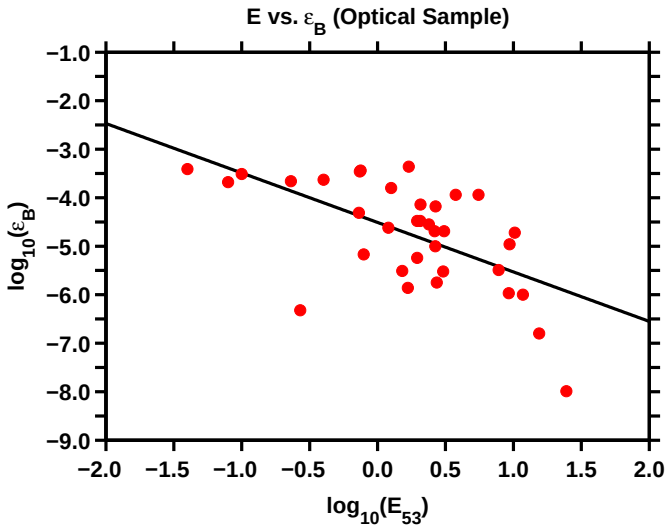

Figure 2.5: We plot the values of E and the measurements of ϵ_B to determine if they are correlated. The 35 points represent the GRBs in our optical sample and the straight line is the best fit line: $\log_{10}(\epsilon_B) = -1.02\log_{10}(E_{53}) - 4.51$, with the slope of the line being -1.02 ± 0.23 and the y-intercept of the line being -4.51 ± 0.16. The correlation coefficient of the fit is 0.62 and the P-value of the correlation is 1.2×10^{-4} (3.8σ significance). The ϵ_B measurements are for $n = 1$ cm^{-3} and p determined from α_O (shown in the filled-in histogram in the Bottom-Right panel of Figure 2.3 and Table 2.4) and the values of E were determined by assuming an efficiency $\sim 20\%$ for all the GRBs in our optical samples.

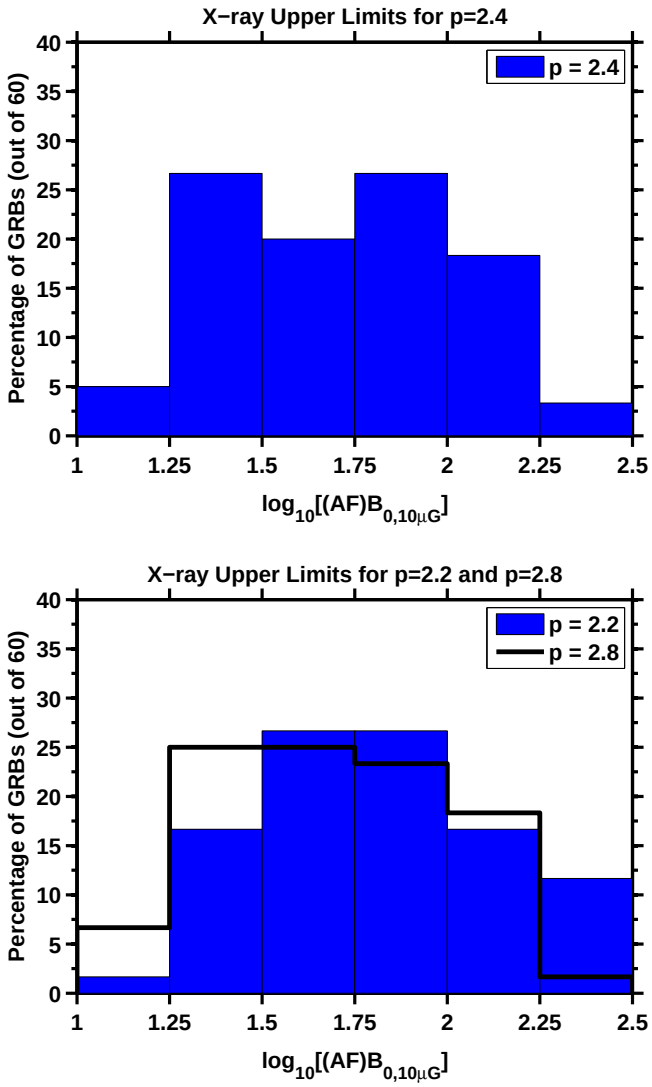

Figure 2.6: *Top Panel:* Upper limits on the quantity $(AF)B_{0,10\mu\mathrm{G}}$ for our X-ray sample assuming $p = 2.4$. *Bottom Panel:* Upper limits on the quantity $(AF)B_{0,10\mu\mathrm{G}}$ for our X-ray sample assuming $p = 2.2$ and $p = 2.8$. A fixed $n = 1\ \mathrm{cm}^{-3}$ was assumed for all of the histograms (the precise value of n is unimportant since AF has a weak dependence on n, see Section 2.8 and Equation 2.15).

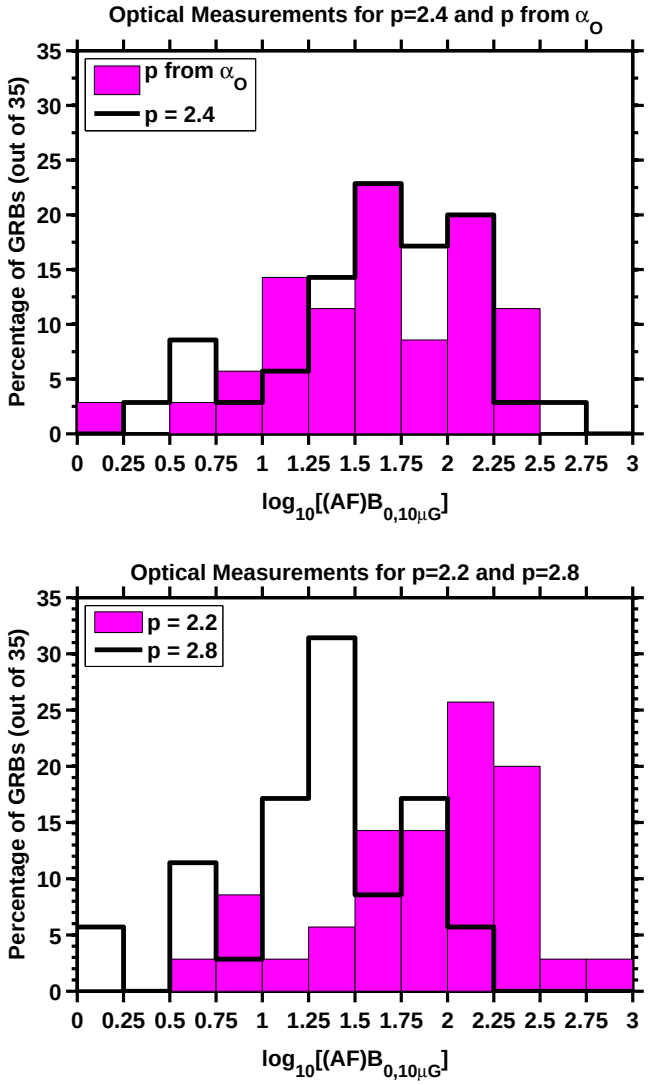

Figure 2.7: *Top Panel:* The filled-in (un-filled) histogram shows the measurements on the quantity $(AF)B_{0,10\mu\mathrm{G}}$ for p calculated from α_O ($p = 2.4$). *Bottom Panel:* The filled-in (un-filled) histogram shows the measurements on the quantity $(AF)B_{0,10\mu\mathrm{G}}$ for $p = 2.2$ ($p = 2.8$). A fixed $n = 1\ \mathrm{cm}^{-3}$ was assumed for all of the histograms (the precise value of n is unimportant since AF has a weak dependence on n, see Section 2.8 and Equation 2.15).

Chapter 3

Monte Carlo Simulations of the Photospheric Process

3.1 Abstract

We present a Monte Carlo (MC) code we wrote to simulate the photospheric process and to study the photospheric spectrum above the peak energy. Our simulations were performed with a photon to electron ratio $N_\gamma/N_e = 10^5$, as determined by observations of the GRB prompt emission. We searched an exhaustive parameter space to determine if the photospheric process can match the observed high-energy spectrum of the prompt emission. If we do not consider electron re-heating, we determined that low photon temperatures and high optical depths are the best condition for producing a power-law spectrum above the peak-energy. The cases we considered with higher photon temperatures and lower optical depths require additional energy in the electrons; we demonstrate that a power-law spectrum can be produced if we consider electron re-heating near the photosphere. We also performed simulations for different values of N_γ/N_e and determined that the simulation results are very sensitive to N_γ/N_e. Lastly, in addition to Comptonizing a Blackbody spectrum, we also simulate the Comptonization of a $f_\nu \propto \nu^{-1/2}$ fast cooled synchrotron spectrum. The spectrum for these simulations peaks at $\sim 10^4$ keV,

with a flat spectrum $f_\nu \propto \nu^0$ below the peak energy.

3.2 Introduction

One of the major open questions in the GRB field is, what is the radiation mechanism that produces the observed broken power-law gamma-ray spectrum, i.e. the Band function (Band et al., 1993). The three main mechanisms that have been used to try and reproduce the Band spectrum are synchrotron, synchrotron self-Compton (SSC), and the photospheric process (See Piran, 2004; Zhang, 2014; Kumar & Zhang, 2015, for reviews). In this work, we focus on the photospheric process (Goodman, 1986; Paczynski, 1990; Thompson, 1994b; Ghisellini & Celotti, 1999; Mészáros & Rees, 2000; Mészáros et al., 2002; Rees & Mészáros, 2005; Thompson et al., 2007), which involves photons undergoing multiple scatterings with hot electrons below the photosphere (Comptonization). Although not a necessary condition for the Comptonization of photons, studies on the photospheric process typically consider the photons to initially have a Blackbody (BB) spectrum, with the peak of the BB spectrum taken to match the observed peak energy of the prompt emission. With an initial seed BB spectrum, the goal of the photospheric process is to broaden the BB spectrum so that it matches the observed Band function. In this work, we focus on photospheric models where the broadening is due to hot electrons scattering photons to higher energies multiple times (Pe'er et al., 2006; Giannios, 2008; Lazzati & Begelman, 2010; Toma et al., 2011; Lazzati et al., 2013; **?**; **?**; Chhotray & Lazzati, 2015), instead of photospheric models

where the broadening is due to geometrical effects (Pe'er, 2008; Pe'er & Ryde, 2011; Mizuta et al., 2011; Ruffini et al., 2013; Bégué et al., 2013; Lundman et al., 2013; Ito et al., 2014; Bégué & Iyyani, 2014); see Vereshchagin 2014 and Pe'er 2015 for reviews.

The basic picture of the photospheric process is as follows. The photons are assumed to be produced below the photosphere. At an optical depth $\tau \sim$ few - 100, a dissipation event is assumed to occur, which accelerates the electrons to mildly relativistic or relativistic speeds [1]. In the photospheric model, the average energy of the photons is taken to be much smaller than the average energy of the electrons. Thus, while the outflow is still optically thick, the photons and electrons undergo multiple scatterings and a photon gains energy from the electrons until its energy reaches the average electron energy or until it escapes the photosphere. The Comptonization of BB photons by hot electrons is predicted to produce a power-law spectrum above the BB peak because only a fraction f of the photons get scattered once by a hot electron to higher energies, only a fraction f^2 of the photons get scattered twice by a hot electron to higher energies, and so on (Lazzati & Begelman, 2010; Ghisellini, 2013). Once the outflow reaches the photospheric radius, the medium becomes optically thin and the photons escape the outflow. The resulting observed spectrum is a peak determined by the BB temperature of

[1]The dissipation events discussed in the literature for the photospheric process are magnetic reconnection (Thompson, 1994b; Giannios & Spruit, 2005; Giannios, 2006, 2012) and internal shocks (Daigne & Mochkovitch, 2002; Lazzati & Begelman, 2010; Toma et al., 2011; Lazzati et al., 2013).

photons and it has a power-law above the peak energy[2].

An important quantity needed to simulate the photospheric process is the ratio of photons to electrons, which we now estimate for the prompt emission. The kinetic energy of the GRB jet is $E_{KE} = N_p m_p c^2 \Gamma$, where N_p is the number of protons and we consider the kinetic energy of the jet to be carried primarily by protons. Then, taking most of the photons during the prompt emission to have an energy near the peak energy of the spectrum ($E_{\rm pk}$), the energy radiated in gamma-rays is $E_\gamma = N_\gamma E_{\rm pk}$. With these two expressions, we can calculate the ratio of E_γ to E_{KE}:

$$\frac{E_\gamma}{E_{KE}} = \frac{N_\gamma E_{\rm pk}}{N_p m_p c^2 \Gamma}. \tag{3.1}$$

Taking $N_p = N_e$ (if few electron-positron pairs are created in the GRB jet, then $N_p \approx N_e$ due to charge neutrality) and defining the efficiency in the conversion of kinetic energy of the jet to prompt radiation as $\eta = E_\gamma/(E_\gamma + E_{KE})$, we can solve for the photon to electron ratio N_γ/N_e (Chhotray & Lazzati, 2015)

$$\frac{N_\gamma}{N_e} = 10^6 \left(\frac{\eta}{1-\eta}\right) \left(\frac{\Gamma}{300}\right) \left(\frac{E_{\rm pk}}{300\ {\rm keV}}\right)^{-1}. \tag{3.2}$$

In this expression, we have normalized Γ and $E_{\rm pk}$ to typical values. Taking an efficiency $\eta \sim 10\%$, the photon to electron ratio is $N_\gamma/N_e \sim 10^5$. Thus, a ratio

[2]One of the major difficulties of the photospheric model is reproducing the typically observed low-energy spectrum $f_\nu \propto \nu^0$. In this work, we ignore the low-energy spectrum issue and focus on the high-energy spectrum. For detailed discussions on the low-energy index of the photospheric process, see Vurm et al. 2013; Lundman et al. 2013; Deng & Zhang 2014.

of photons to electrons $\sim 10^5$ is required to simulate the photospheric process (Lazzati & Begelman, 2010; Chhotray & Lazzati, 2015).

Previous MC photospheric works have demonstrated that there is a power-law above the peak of the spectrum for $N_\gamma/N_e \sim 10^1 - 10^4$, where N_γ (N_e) is the number of photons (electrons) considered (Lazzati & Begelman, 2010; Chhotray & Lazzati, 2015). However, whether the power-law above the peak of the spectrum is a robust feature of the photospheric model is still in question since realistic simulations with $N_\gamma/N_e = 10^5$ have not been performed. We developed a new MC photospheric code capable of performing simulations for realistic GRB N_γ/N_e ratios. In this work, we present results for MC photospheric simulations with $N_\gamma/N_e = 10^5$ for the first time and we perform an exhaustive parameter space search to determine if the photospheric process can produce the observed high-energy spectral index of the Band function. In addition, we include adiabatic cooling of photons and electrons, which was neglected by previous MC photospheric codes (Lazzati & Begelman, 2010; Chhotray & Lazzati, 2015).

Another possible source for the seed photons is the synchrotron process. Therefore, in addition to considering the Comptonization of a BB spectrum of photons, we also consider the Comptonization of a seed photon spectrum $f_\nu \propto \nu^{-1/2}$, the expected synchrotron spectrum when electrons are in the fast cooling regime (Sari et al., 1996; Ghisellini et al., 2000). We use our MC photospheric code to study how Comptonization modifies this seed spectrum.

This work is organized as follows. In Section 3.3, we describe the algo-

rithm of our MC photospheric code (the expressions for the implementation can be found in the Appendices). In Section 4.7.1.2, we discuss the parameters we explore for our MC photospheric simulations with a seed BB spectrum. The simulation results for the Comptonization of a seed BB spectrum are discussed in Section 3.5 and the interpretation of these results is discussed in Section 3.6. In Section 3.7, we discuss the parameters we explore for our simulations on the Comptonization of a seed $f_\nu \propto \nu^{-1/2}$ spectrum, the results for these simulations, and the interpretation of these results. Lastly, in Section 3.8, we discuss our conclusions.

3.3 Description of Monte Carlo Photospheric Code

In this section, we give an overview of our MC photospheric code algorithm. The details for implementation can be found in the Appendices. Our code was written in the C++11 programing language and we used the GCC version 4.9.2 compiler. Under 9 GB of RAM are needed for a simulation with 10^8 photons and a simulation initialized at $\tau_{\rm initial} = 2$ takes under 2 hours in a regular desktop Linux machine (see definition of $\tau_{\rm initial}$ below). Lastly, we note that our code is not parallelized; each scattering event between a photon and an electron is performed one by one.

3.3.1 Input Parameters for Simulations with Seed BB Photons

The input parameters for our MC photospheric simulations with a seed BB spectrum of photons are described below. In Section 3.7, we will discuss the

input parameters for the simulations with a $f_\nu \propto \nu^{-1/2}$ seed spectrum. In the discussion below and throughout this work, unprimed (primmed) quantities refer to quantities in the observer (jet-comoving) frame.

- Γ — The bulk Lorentz factor of the outflow. We consider a typical $\Gamma = 300$ for GRBs (Molinari et al., 2007; Xue et al., 2009; Liang et al., 2010).

- L — The isotropic equivalent kinetic luminosity of the outflow. We consider $L = 10^{52}$ ergs/sec (Liang et al., 2007; Wanderman & Piran, 2010).

- N_e — The number of electrons in a simulation. We consider $N_e = 10^3$, the same number of electrons as previous MC photospheric simulations (Lazzati & Begelman, 2010; Chhotray & Lazzati, 2015). In Section 3.3.5, we explicitly show that 10^3 electrons are enough to get an accurate representation for a electron distribution.

- Electron Distribution — We consider three different distributions for the electrons: 1. mono-energetic electrons (all electrons initialized to the same electron Lorentz factor γ'_e), with the initial γ'_e of the electrons as the input parameter. 2. Maxwell-Boltzmann (MB) distribution of electrons with the electron temperature T'_e as an input parameter. 3. Power-Law distribution of electrons $dN_e/d\gamma'_e \propto (\gamma'_e)^{-p}$ ranging from $\gamma'_{e,1}$ to $\gamma'_{e,2}$, with the electron Lorentz factors $\gamma'_{e,1}$, $\gamma'_{e,2}$, and the electron index p as input parameters.

- $\tau_{\rm initial}$ — The optical depth corresponding to the distance from the central engine where the photons are initialized (see Equation 3.3). We consider $\tau_{\rm initial} = 2, 8, 16$.

- N_γ — The number of photons in a simulation. Since we typically consider $N_e = 10^3$, to reach $N_\gamma/N_e = 10^5$, we consider $N_\gamma = 10^8$ for our simulations.

- $T_\gamma^{'}$ — The photons are initialized to have a Blackbody (BB) distribution with temperature $T_\gamma^{'}$.

- $N_{\rm collect}$ — The number of photons collected for the output spectrum. We consider $N_{\rm collect} = N_\gamma/3$ for our simulations as in Lazzati & Begelman 2010 since considering $N_{\rm collect} = N_\gamma/3$ allows for enough scatterings to occur so that the electrons can cool by IC scatterings. By plotting the first $N_\gamma/3$ photons that escape the photosphere for an output spectrum, we are plotting a time-averaged spectrum.

3.3.2 Initializing Electrons and Photons

The first step of our MC photospheric simulations is to initialize the electrons and photons. The only property we track in the observer frame is the position of the photons to determine if they have escaped the photosphere.

3.3.2.1 Initialization of Direction and Energy of Electrons

The directions of the N_e electrons are drawn randomly in the jet-comoving frame (see Appendix B.2.1 for algorithm). The γ_e' for each of the N_e electrons is drawn from the distribution specified in the input parameters (see Appendix B.2.2 for algorithm). We assume that the electrons are distributed uniformly in the jet and do not track their position.

3.3.2.2 Initialization of Direction, Energy, and Position of Photons

The directions of the N_γ photons are drawn randomly in the jet-comoving frame(see Appendix B.3.1 for algorithm). The energy of each of the N_γ photons in the jet-comoving frame (E_γ') is drawn from either a BB distribution with temperature $T_\gamma^{'}$ or a power-law distribution (depending on the system being investigated) (see Appendix B.3.2 for algorithm).

The origin of the coordinate system we use to track the position of the photons in the observer frame is the central engine. The N_γ photons are initially placed randomly and uniformly within an angle $\leq 1/\Gamma$ (jet opening angle) in the direction of the observer at a distance

$$R_{\rm initial} = \frac{L\sigma_T}{8\pi m_p c^3 \beta \Gamma^3 \tau_{\rm initial}}, \tag{3.3}$$

where σ_T is the Thomson cross section and $\beta = \sqrt{1-\Gamma^{-2}}$ is the speed of the outflow divided by the speed of light.

We then draw the distance s' each photon travels in the jet-comoving frame before running into an electron randomly from the probability density

$p(s') \propto \exp(-s'/\ell'_{\rm mfp})$, where $\ell'_{\rm mfp}$ is the mean free path. Inverting this probability density, s' is sampled with the formula $s' = -\ell'_{\rm mfp}\ln(\xi)$, where ξ is a uniformly distributed random number between 0 and 1. The mean free path and the electron density (n'_e) are given by

$$\ell'_{\rm mfp}(R) = \frac{1}{n'_e(R)\sigma_T} \quad (3.4)$$

$$n'_e(R) = \frac{L}{4\pi R^2 m_p c^3 \Gamma^2}, \quad (3.5)$$

where R is the distance of the photon from the central engine in the observer frame. The distance each photon travels in the jet comoving frame is then Lorentz transformed to the observer frame to determine the new location of the photon in the observer frame (see Appendix B.3.3 for algorithm).

3.3.3 Adiabatic Cooling of Photons and Electrons

As the jet expands outward, the energy of the photons and electrons decreases due to adiabatic cooling. Adiabatic cooling depends on the radial distance traveled by the jet, with the energy of the photons decreasing by a factor $r^{-2/3}$ and the kinetic energy of the electrons decreasing by a factor $r^{-2/3}$ or $r^{-4/3}$, depending on whether a electron is relativistic or sub-relativistic. This scaling is valid as long as the radial width of the jet does not change with distance, which is satisfied for highly relativistic jets below the photosphere. Thus, in between scattering events, the expressions we use to update the energy

of a photon and the γ'_e of a electron due to adiabatic cooling are

$$\frac{E'_{\gamma,f}}{E'_{\gamma,i}} = \left(\frac{R_{\rm initial} + (t_\gamma + \Delta t_\gamma)\beta_j c}{R_{\rm initial} + t_\gamma \beta_j c}\right)^{-2/3} \tag{3.6}$$

$$\frac{\gamma'_{e,f} - 1}{\gamma'_{e,i} - 1} = \left(\frac{R_{\rm initial} + (t_\gamma + \Delta t_\gamma)\beta_j c}{R_{\rm initial} + t_e \beta_j c}\right)^{2-2(4\gamma'_{e,i}+1)/(3\gamma'_{e,i})}. \tag{3.7}$$

In these equations, $R_{\rm initial}$ corresponds to the distance where the photons are initialized (Equation 3.3) and the subscript i (f) corresponds to a photon and electron property before (after) the photon travels a distance s' (in the jet comoving frame). t_γ (t_e) represents the total time elapsed for a photon (electron) in between scattering events (in the observer frame). Thus, in the time t_γ (t_e), the jet has traveled a radial distance $t_\gamma \beta_j c$ ($t_e \beta_j c$) and the radial position of the photon (electron) before the photon travels a distance s' is $R_{\rm initial} + t_\gamma \beta_j c$ ($R_{\rm initial} + t_e \beta_j c$). Δt_γ represents the time it takes a photon to travel a distance s' (in the observer frame, see Appendix B.3.3); thus, the final radial position of the photon and electron are $R_{\rm initial} + (t_\gamma + \Delta t_\gamma)\beta_j c$. Lastly, we note that the $(4\gamma'_{e,i} + 1)/(3\gamma'_{e,i})$ term in the exponent of Equation 3.7 is used to take into account that the electron adiabatic index transitions from 4/3 to 5/3 as the electron cools due to IC scatterings and adiabatic expansion.

3.3.4 Main MC Photospheric Program

The first step in our main program is to check for photons that were able to escape the photosphere ($R_{\rm photosphere}$ is defined as the radius where $\tau = 1$ in Equation 3.3) without interacting with an electron with the first s' drawn. If a photon was able to escape the photosphere, we Doppler boost its energy

to the observer frame with the Doppler factor, $\mathcal{D}E'_\gamma$, and store this energy. Otherwise, we place this photon in a priority queue data structure. Each element in the priority queue is a tuple with entries ($t_{\gamma,k}$, k), where k refers to the index of a photon in an array and $t_{\gamma,k}$ refers to the total elapsed time in between scatterings of this particular photon (in the observed frame). With the photons in a priority queue, the photon with the smallest $t_{\gamma,k}$ gets scattered first (is given priority) and then the photon with the next smallest $t_{\gamma,k}$ gets scattered next and so on (Lazzati & Begelman, 2010). Having the array index of the photon (k) allows us to access the properties of this particular photon (energy, direction, and position).

In the next part of the program, we take into account adiabatic cooling and determine whether a photon-electron scattering event will occur. We first draw one of the N_e electrons randomly. Then, we use the s' of the first photon in the priority queue (photon with smallest $t_{\gamma,k}$) to propagate this photon forward (see Appendix B.3.3 for algorithm) . After using Equations 3.6 - 3.7 to take into account adiabatic cooling, we calculate the dimensionless photon energy of this particular photon in the rest frame of this particular electron (defined as x'_i) and the cross-section for this interaction (defined as $\sigma(x'_i)$; see Appendix B.4 for algorithm). The probability that the scattering event will occur is $\sigma(x'_i)/\sigma_T$, where $\sigma(x'_i) \leq \sigma_T$. To determine if the scattering event occurs, we draw a uniformly distributed random number between 0 and 1, defined as ξ_s. If $\xi_s \leq \sigma(x'_i)/\sigma_T$, the scattering event occurs. If the scattering event occurs, we update the energy and direction of the photon (see Appendix

B.4 for algorithm) and the energy and direction of the electron (see Appendix B.5 for details) after the scattering event. Then (regardless of whether the scattering event occurred or not), we draw a new s' at the current location R of the photon with the expression $s'(R) = -\ell'_{\rm mfp}(R)\ln(\xi)$. The distance the photon travels in the jet-comoving frame is then Lorentz transformed to the observer frame to check if the photon has escaped the photosphere. If $R \geq R_{\rm photosphere}$ is satisfied, we store the energy of this photon in the observer frame ($\mathcal{D}E'_\gamma$). Otherwise, we place this photon back in the priority queue with the new $t_{\gamma,k}$. We repeat the process described in this paragraph until $N_{\rm collect}$ photons have escaped the photosphere.

3.3.5 MC Photospheric Code Tests

To test our code, we compared our simulation results to the MC photospheric code results from Lazzati & Begelman (2010). In the left panel of Figure 3.1, we compare our simulation results to the three simulations in Figure 4 of Lazzati & Begelman (2010). In this figure and throughout this work, f_ν represents the specific flux, the flux per unit frequency ν, in the observer frame. For these simulations, we use the same input parameters as Lazzati & Begelman (2010): $\Gamma = 1000$, $k_B T'_\gamma = 90$ eV, $N_\gamma = 3 \times 10^6$, $N_e = 10^3$, $N_{\rm collect} = N_\gamma/3$, mono-energetic electrons initialized to $\gamma'_e = 2$, $\tau_{\rm initial} = 2$, 8, 16, and no adiabatic cooling. There is good agreement for all the simulations. To quantify this agreement, we performed Kolmogorov-Smirnov (KS) tests. The probability that our simulations are drawn from the same distribution as

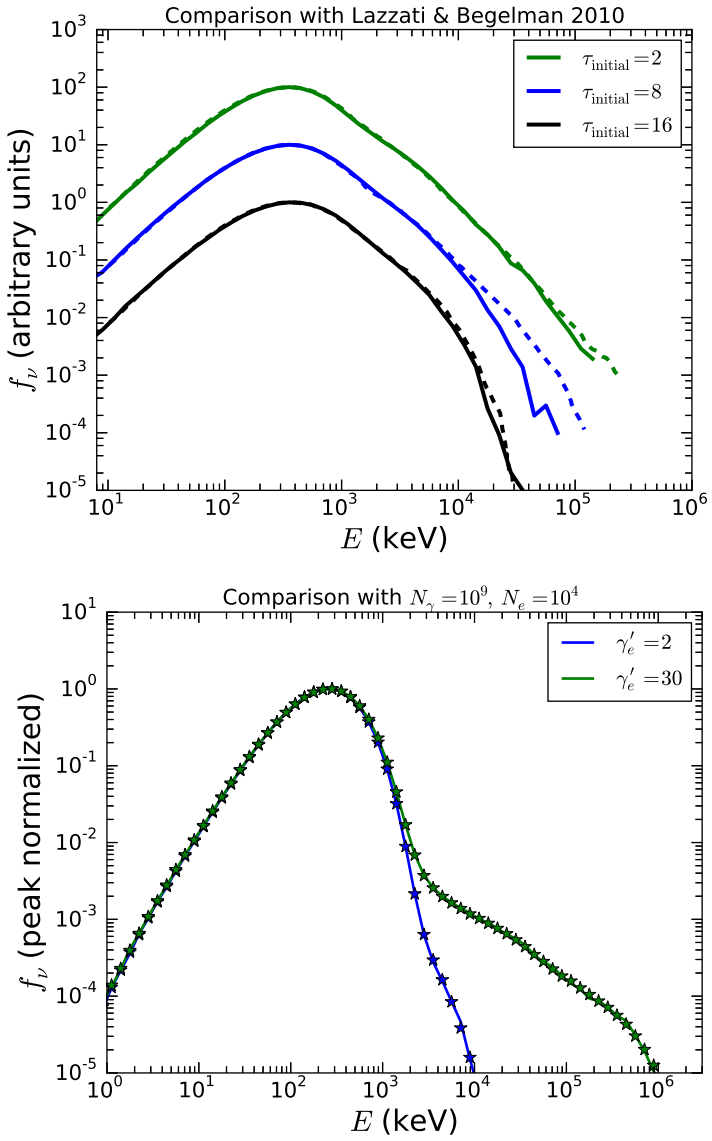

Figure 3.1: *Top Panel:* Comparison of our MC photospheric simulation results (solid lines) to those from Figure 4 of Lazzati & Begelman (2010) (dotted lines). These simulations are for the Comptonization of seed BB photons with $k_B T'_\gamma =$ 90 eV, $\Gamma = 1000$ with mono-energetic electrons with initial $\gamma'_e = 2$, $\tau_{\rm initial} = 2$, 8, 16, and no adiabatic cooling. *Bottom Panel:* Comparison of $N_\gamma = 10^9$, $N_e = 10^4$ (stars) simulation results to $N_\gamma = 10^8$, $N_e = 10^3$ (solid lines) simulation results. The simulations are for the Comptonization of seed BB photons with $k_B T'_\gamma = 300$ eV, $\Gamma = 300$ with mono-energetic electrons with initial $\gamma'_e = 2$, 30, $\tau_{\rm initial} = 2$, and adiabatic cooling.

those of Lazzati & Begelman (2010) (P-values) are 0.9999 for $\tau_{\rm initial} = 2$, 0.9862 for $\tau_{\rm initial} = 8$, and 0.9809 for $\tau_{\rm initial} = 16$. This good agreement demonstrates that our MC photospheric code is working properly.

We next perform a test to determine if 10^3 electrons are enough to represent an electron distribution. If there are not enough electrons, the photon spectrum will look very noisy. Previous MC photospheric studies (Lazzati & Begelman, 2010; Chhotray & Lazzati, 2015) found that 10^3 electrons are enough to represent an electron distribution; however, their simulations were performed for lower N_γ/N_e. To determine if 10^3 electrons are enough for our $N_\gamma/N_e = 10^5$ simulations, we perform 2 simulations with $N_\gamma = 10^9$, $N_e = 10^4$ (10 times more photons and electrons) and compared them to simulation results with $N_\gamma = 10^8$, $N_e = 10^3$ in right panel of Figure 3.1 (we used the input parameters described in Section 4.7.1.1 for mono-energetic electrons with initial $\gamma'_e = 2$, 30 $k_B T'_\gamma = 300$ eV, $\Gamma = 300$, and adiabatic cooling). From KS tests, the probability that the two $\gamma'_e = 2$ [$\gamma'_e = 30$] simulations are drawn from the same distribution is 0.9999 [0.9999]. This good agreement explicitly demonstrates that 10^3 electrons are enough for $N_\gamma/N_e = 10^5$ simulations.

3.4 Parameters Considered for MC Simulations with Seed BB Photons

We now discuss the range of parameters we consider for our simulations. The main input parameters that affect the output spectrum are $k_B T'_\gamma$ (determines the energy of the majority of the photons), γ'_e (determines energy

in the electrons), and $\tau_{\rm initial}$ (determines the average number of scatterings before a photon arrives at the photosphere). L determines the physical scales of the system by determining $R_{\rm initial}$, $R_{\rm photosphere}$, n'_e, and $\ell'_{\rm mfp}$, but it does not affect the number of scatterings or the shape of the spectrum. The main effect of Γ is to Doppler boost the photon spectrum to the observer frame. In addition, Γ also determines the physical scales of the system by determining $R_{\rm initial}$, $R_{\rm photosphere}$, n'_e, and $\ell'_{\rm mfp}$.

For our simulations, we considered $k_B T'_\gamma = 30$ eV, 100 eV, 300 eV. One way the photon temperature can affect the output spectrum is through the production of electron-positron pairs by photon annihilation, which would decrease (increase) the number of photons (electrons) in a simulation. However, since the typical photon energies we are considering $k_B T'_\gamma \sim 30$ eV-300 eV are much less than $m_e c^2$, electron-positron pair production is expected to be unimportant and we neglect it for our simulations. Another more important effect $k_B T'_\gamma$ has on the simulation results is on the cooling of electrons. The photons in the jet-comoving frame are more energetic for larger $k_B T'_\gamma$ and more energetic photons will cool the electrons faster when they undergo multiple scatterings.

γ'_e is an important parameter since it determines the available energy electrons have to transfer to photons. The smallest value we consider for γ'_e is 2. In the photospheric model, in order to avoid synchrotron cooling from the magnetic field that is expected to be present in the jet, the synchrotron emission is taken to be self-absorbed. The largest γ'_e that can be considered

is found by setting the optical depth for synchrotron self-absorption equal to 1. Below, we calculate the largest γ'_e allowed for MB and PL distributions of electrons.

For a MB distribution distribution of electrons, the synchrotron self-absorption optical depth $\tau_{\rm syn}^{\rm MB}$ is given by (Rybicki & Lightman, 1979; Lazzati & Begelman, 2010)

$$\tau_{\rm syn}^{\rm MB} = \frac{10^6}{(\gamma'_e)^5 \epsilon_B^{1/2} (E'_\gamma/1{\rm keV})^2}. \tag{3.8}$$

In this equation, $\epsilon_B = U_B/U_{\rm rad}$, where U_B ($U_{\rm rad}$) is the energy density in the magnetic field (radiation) and we note that $\tau_{\rm syn}^{\rm MB}$ depends on the energy of the photons in the comoving frame. Setting $\tau_{\rm syn}^{\rm MB} = 1$, for $\epsilon_B \sim 0.1$ (magnetic field subdominant to radiation) and $E'_\gamma \sim 300$ eV ($E'_\gamma \sim 100$ eV) [$E'_\gamma \sim 30$ eV], the upper limit we find is $\gamma'_e \sim 30$ ($\gamma'_e \sim 50$) [$\gamma'_e \sim 80$].

For a power-law distribution distribution of electrons, the synchrotron self-absorption optical depth $\tau_{\rm syn}^{\rm PL}$ is given by (Wu et al., 2003; Gou et al., 2007)

$$\begin{aligned} \tau_{\rm syn}^{\rm PL} &= \frac{e}{B'} \left(\frac{(p-1)(p+2)}{(\gamma'_1)^{-(p-1)} - (\gamma'_2)^{-(p-1)}} \right) \times \\ & \frac{2\sqrt{6}\pi^{3/2}}{9} (\gamma'_2)^{-(p+4)} \exp(-1) \sigma_T^{-1}. \end{aligned} \tag{3.9}$$

In this equation, γ'_1 (γ'_2) is the electron Lorentz factor where the power-law begins (ends) and B' is the magnetic field in the jet-comoving frame. From the expressions $U_B = (B')^2/(8\pi)$ and $U_{\rm rad} = a_{\rm rad}(T'_\gamma)^4$, $B' = (8\pi\epsilon_B a_{\rm rad})^{1/2}(T'_\gamma)^2$. Setting $\tau_{\rm syn}^{\rm PL} = 1$, taking $\gamma'_1 = 2$, $p = 2.4$, and B' corresponding to $\epsilon_B = 0.1$ and $k_B T'_\gamma =$ 300 eV ($k_B T'_\gamma =$ 100 eV) [$k_B T'_\gamma =$ 30 eV], the upper limit we

$k_B T'_\gamma$	Mono-Energetic	MB	PL Distribution
30 eV	γ'_e = 2, 30, 80	$\frac{k_B T'_e}{(\gamma_{\rm ad,el}-1)m_e c^2}$ = (2-1), (80-1)	$\gamma'_{e,1}$ = 2, $\gamma'_{e,2}$ = 80, p = 2.4
100 eV	γ'_e = 2, 30, 50	$\frac{k_B T'_e}{(\gamma_{\rm ad,el}-1)m_e c^2}$ = (2-1), (50-1)	$\gamma'_{e,1}$ = 2, $\gamma'_{e,2}$ = 50, p = 2.4
300 eV	γ'_e = 2, 10, 30	$\frac{k_B T'_e}{(\gamma_{\rm ad,el}-1)m_e c^2}$ = (2-1), (30-1)	$\gamma'_{e,1}$ = 2, $\gamma'_{e,2}$ = 30, p = 2.4

Table 3.1: γ'_e values we consider for our simulations for each value of $k_B T'_\gamma$ and the 3 different electron distributions we consider. For the MB distribution, we give the value of $k_B T'_e = (\gamma_{\rm ad,el} - 1)(\gamma'_e - 1)m_e c^2$, where $\gamma_{\rm ad,el} = (4\gamma'_e + 1)/(3\gamma'_e)$ is the electron adiabatic index, since $k_B T'_e$ measures the kinetic energy of the electrons.

found for γ'_2 is $\gamma'_2 \sim 30$ ($\gamma'_2 \sim 50$) [$\gamma'_2 \sim 80$]. Thus, for both a MB distribution and a PL distribution, the maximum γ'_e we can consider for $k_B T'_\gamma =$ 300 eV ($k_B T'_\gamma =$ 100 eV) [$k_B T'_\gamma =$ 30 eV] is ~ 30 (~ 50) [~ 80]. A summary of the values we considered for γ'_e for each value of $k_B T'_\gamma$ is given in Table 3.1.

$\tau_{\rm initial}$ affects the shape of the spectrum since it determines the average number of scatterings a photon experiences before escaping the photosphere. The average number of scatterings for a photon is $\sim 2\tau_{\rm initial}$ (Bégué et al., 2013), not $\sim (\tau_{\rm initial})^2$, since as the GRB relativistic outflow moves outward, n'_e decreases as R^2 (Equation 3.5). For our simulations, we considered $\tau_{\rm initial} =$ 2, 8, 16.

Lastly, since $N_\gamma \gg N_e$ for our simulations, the electrons rapidly cool by IC scatterings and then the electrons no longer have much energy to transfer to the photons. Thus, we also considered electron re-heating. At a given $\tau_{\rm initial}$, the total number of scatterings expected is $\sim 2\tau_{\rm initial} N_\gamma$. To re-heat the electrons, we first specify the number of re-heating events $N_{\rm rh}$ we choose to consider. Then, after $(2\tau_{\rm initial} N_\gamma)/(N_{\rm rh} + 1)$ scatterings, we re-heat the

electrons to the same distribution that they were initialized to (we divide by $N_{\rm rh}+1$ since the total number of heating events is the initial heating event plus $N_{\rm rh}$ events). We adopt this methodology to have the re-heating events evenly spaced within the total number of scatterings.

3.5 Simulation Results for Comptonization of Seed BB Spectrum

In this section, we first show our results for one dissipation event, where electrons are only accelerated once at the start of the simulation. Then, we consider electron re-heating, where the electrons are re-accelerated back to their initial distribution $N_{\rm rh}$ times.

3.5.1 Simulation Results for One Dissipation Event

In Figure 3.2, we show simulations for $\tau_{\rm initial}=2$, the three values we considered for $k_BT'_\gamma$, and mono-energetic electrons with the values of γ'_e shown in Table 3.1. As the reader many have noticed in Figure 3.1, the most striking feature of the output spectrum is the sharp drop in f_ν by ~ 2 orders of magnitude after the peak energy, $E_{\rm pk}$. Unlike previous studies for $N_\gamma/N_e = 1-10^4$, our results for $N_\gamma/N_e=10^5$ do not show a power-law immediately after the peak energy. After the drop in f_ν, the simulations with $\gamma'_e=2$ in the three panels continue to decline rapidly. On the other hand, the simulations with $\gamma'_e\sim 10-80$ in each panel display a power-law for $\sim 2-3$ decades in energy before declining rapidly again. The highest energy the photons near the

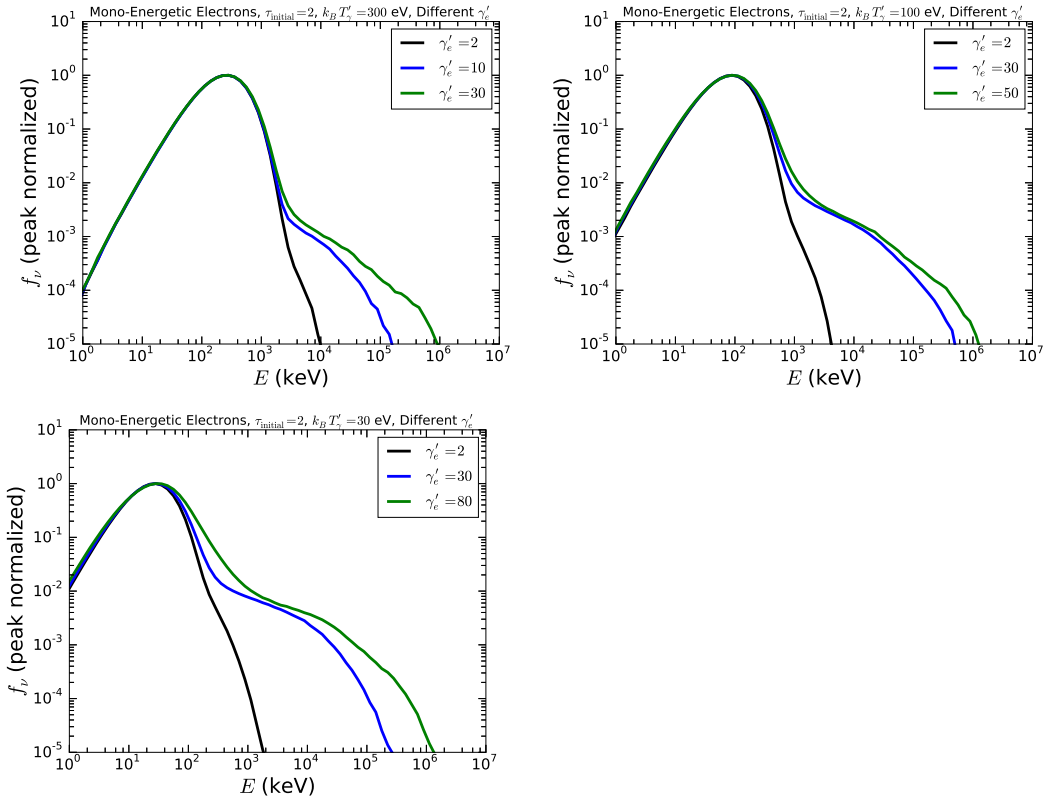

Figure 3.2: *Top-Left panel:* Simulation results for the Comptonization of seed BB photons with $k_BT'_\gamma = 300$ eV, $\Gamma = 300$ with mono-energetic electrons with initial $\gamma'_e = 2$, 10, 30 and $\tau_{\rm initial} = 2$. *Top-Right panel:* Same as *Top-Left panel* for $k_BT'_\gamma = 100$ eV, $\Gamma = 300$ and mono energetic electrons with initial $\gamma'_e = 2$, 30, 50. *Bottom-Left panel:* Same as *Top-Left panel* for $k_BT'_\gamma = 30$ eV, $\Gamma = 300$ and mono energetic electrons with initial $\gamma'_e = 2$, 30, 80.

BB peak can attain after one scattering is $\sim 4 \times (100 \text{ eV})\Gamma(\gamma_e')^2 \sim 10^5$ keV for $\gamma_e' \sim 50$. Once the photons reach these energies, IC scattering is highly Klein-Nishina (KN) suppressed, leading to an exponential decay in the spectrum for higher energies.

In Figure 3.3, we show simulation results for $\tau_{\text{initial}} = 2$, the three values we considered for $k_B T_\gamma'$, and the largest γ_e' we considered for each distribution in Table 3.1. In each panel, the PL distribution simulations display the least broadened spectrum. This is due to the fact that the PL distribution contains the least energetic electrons among these three distributions. The mono-energetic and MB electron distribution simulations show similar results since the two distributions are similar; the MB distribution has an average γ_e' very close to the γ_e' value we consider for the mono-energetic electrons. After the sharp drop in f_ν in each panel, all the simulations display a single power-law spectrum for ~ 3 decades in energy.

In Figure 3.4, we show simulation results for $\tau_{\text{initial}} = 2$, 8, 16, the three values of $k_B T_\gamma'$ we considered, and MB electrons with the largest value we considered for γ_e' (see Table 3.1). In addition, in each panel, we also plot the energy spectrum $f_\nu = EN_E$ of the kinetic energies of the electrons at the end of each simulation in the observer frame, i.e. $m_e c^2(\gamma_e - 1)\Gamma$. Increasing τ_{initial} has two effects on the output spectrum: decreasing the number of photons at higher energies and increasing the broadening of the spectrum. For larger τ_{initial}, the additional scatterings allow for the high-energy photons to transfer energy back to the electrons. The increase in broadening of the spectrum from

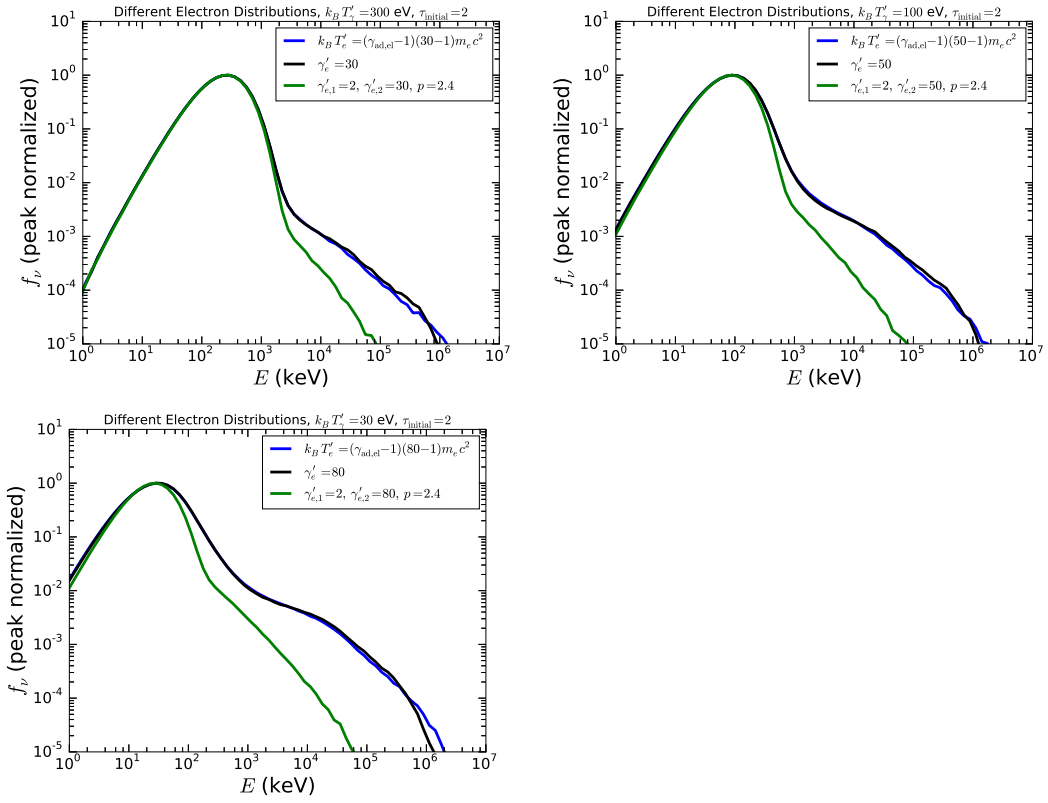

Figure 3.3: *Top-Left panel:* Simulation results for the Comptonization of seed BB photons with $k_B T'_\gamma = 300$ eV, $\Gamma = 300$ with electrons following MB, mono energetic, and PL distributions, and $\tau_{\rm initial} = 2$. For each distribution, we considered the largest value of γ'_e we can consider for $k_B T'_\gamma = 300$ eV (see discussion in Section 4.7.1.2 and Table 3.1). *Top-Right panel:* Same as *Top-Left panel* but with $k_B T'_\gamma = 100$ eV, $\Gamma = 300$. *Bottom-Left panel:* Same as as *Top-Left panel* but with $k_B T'_\gamma = 30$ eV, $\Gamma = 300$.

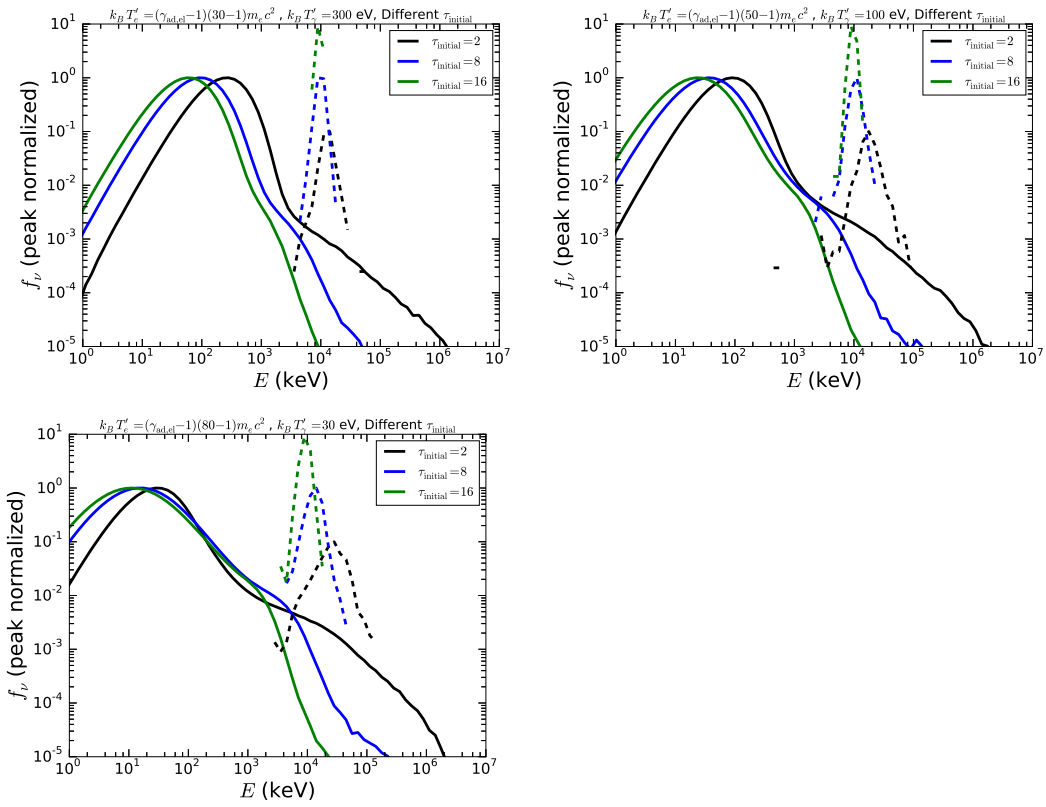

Figure 3.4: *Top-Left panel:* Simulation results for the Comptonization of seed BB photons with $k_B T'_\gamma = 300$ eV, $\Gamma = 300$ with MB electrons with initial $\gamma'_e \sim 30$ and $\tau_{\rm initial} = 2$, 8 16. The photon (electron) spectra are represented by solid (dotted) lines. For both the photons and the electrons, we are plotting their energy spectrum $f_\nu = EN_E$. The photon spectra are peak normalized and the electron spectra are shifted down by a factor of 10 for each $\tau_{\rm initial}$ to better see if there is any change as $\tau_{\rm initial}$ becomes larger. *Top-Right panel:* Same as *Top-Left panel*, but with $k_B T'_\gamma = 100$ eV, $\Gamma = 300$ and MB electrons with initial $\gamma'_e \sim 50$. *Bottom-Left panel:* Same as *Top-Left panel*, but with $k_B T'_\gamma = 30$ eV, $\Gamma = 300$ and MB electrons with initial $\gamma'_e \sim 80$.

$k_B T'_\gamma = 300$ eV (Top-Left Panel) to $k_B T'_\gamma = 30$ eV (Bottom-Left Panel) is due to a couple of effects: 1. the larger γ'_e considered for $k_B T'_\gamma = 30$ eV allows for the electrons to transfer more energy to the photons. 2. for $k_B T'_\gamma = 30$ eV, the photons have lower energy in the jet-comoving frame, and thus, cool the electrons more slowly, allowing for more photons to be upscattered to higher energies. In each panel, the simulations with larger $\tau_{\rm initial}$ have a lower peak-energy due to the adiabatic cooling of photons. In the top-left panel, the three simulations show a sharp drop in f_ν by ~ 2 orders of magnitude above the peak energy. In the top-right panel, the $\tau_{\rm initial} = 8$, 16 almost show a power-law above the peak-energy, but the spectrum still declines rapidly. Fitting a power-law to the $\tau_{\rm initial} = 8$, 16 simulations, we find a steep spectrum $f_\nu \propto \nu^{-2}$. In the bottom-left panel, the $\tau_{\rm initial} = 8$, 16 simulations show a power-law above the peak-energy, with a $f_\nu \propto \nu^{-1.2}$ spectrum, in agreement with the Band function.

The electron distributions at the end of all the simulations display a Maxwell-Boltzmann distribution. In each panel, as $\tau_{\rm initial}$ increases, the electron distributions become narrower and the electron temperature decreases. This is due to the fact that the additional scatterings allow for the electrons to transfer more energy to the photons.

In summary, we searched a wide parameter space for the photospheric process in Figures 3.2-3.4. In Figure 3.2, for $\tau_{\rm initial} = 2$, there is a sharp drop in f_ν above the peak-energy by ~ 2 orders of magnitude for all the photon temperatures and γ'_e values we considered. In Figure 3.3, we determined that

the electron distribution does not have a large impact on the simulation results. In Figure 3.4, we determined that considering a larger optical depth and a lower photon temperature broadens the BB spectrum more, with a power-law spectrum being developed above the peak-energy for the lowest photon temperature we considered ($k_B T'_\gamma =$ 30 eV). In the next subsection, we consider electron re-heating to determine the additional energy that needs to be added to the electrons of the $k_B T'_\gamma =$ 100 eV, 300 eV simulations to produce a power-law above the peak-energy.

3.5.2 Simulation Results with Electron Re-heating

In the top-left panel of Figure 3.5, we show electron re-heating results for $\tau_{\rm initial} = 5$, $k_B T'_\gamma =$ 300 eV, mildly relativistic electrons with initial $\gamma'_e \sim 2$, and $N_{\rm rh} = 10$, 100, 1000. We considered a larger $\tau_{\rm initial}$ (5 as opposed to 2) to allow a larger space for the re-heating events to occur. For $N_{\rm rh} = 10$, f_ν still drops after the peak energy by $\sim$ 2 orders of magnitude. For $N_{\rm rh} = 100$, f_ν displays a power-law above the peak energy for $\sim$ 2 decades, with a spectrum $f_\nu \propto \nu^{-1.43}$. For $N_{\rm rh} = 1000$, f_ν also displays a power-law above the peak energy for $\sim$ 2 decades, with a shallower spectrum $f_\nu \propto \nu^{-0.67}$. In the top-right panel, we show simulations results for $\tau_{\rm initial} = 5$, $k_B T'_\gamma =$ 300 eV, $\gamma'_e \sim 30$, and $N_{\rm rh} = 2$, 20, 200. For $N_{\rm rh} = 20$, 200, there is a power-law spectrum above the peak energy for $\sim$ 2 decades, with $f_\nu \propto \nu^{-1.06}$ for $N_{\rm rh} = 20$ and $f_\nu \propto \nu^{-0.34}$ for $N_{\rm rh} = 200$. In the bottom-left panel, we show electron re-heating simulations for $\tau_{\rm initial} = 5$, $k_B T'_\gamma =$ 100 eV, $\gamma'_e \sim 2$. For $N_{\rm rh} = 50$,

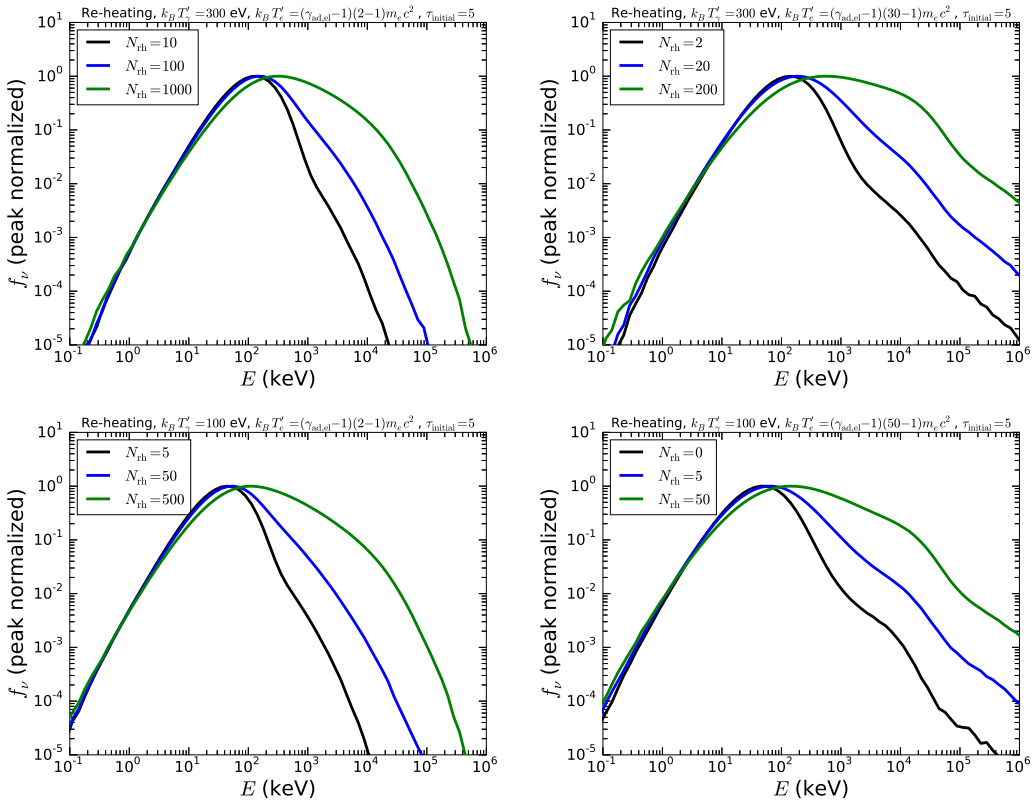

Figure 3.5: *Top-left Panel:* Simulation results for the Comptonization of seed BB photons with $k_B T'_\gamma =$ 300 eV, $\Gamma = 300$ with mildly relativistic electrons with initial $\gamma'_e \sim 2$, $\tau_{\rm initial} = 5$, and $N_{\rm rh} = 10$, 100, 1000 electron re-heating events. *Top-right Panel:* Same as top-left panel, but with $\gamma'_e \sim 30$ and $N_{\rm rh} =$ 2, 20, 200 electron re-heating events. *Bottom-left Panel:* Simulation results for the Comptonization of seed BB photons with $k_B T'_\gamma =$ 100 eV, $\Gamma = 300$ with mildly relativistic electrons with initial $\gamma'_e \sim 2$, $\tau_{\rm initial} = 5$, and $N_{\rm rh} = 5$, 50, 500 electron re-heating events. *bottom-right Panel:* Same as top-left panel, but with $\gamma'_e \sim 50$ and $N_{\rm rh} = 0$, 5, 50 electron re-heating events.

500, there is a power-law spectrum above the peak energy for ~ 2 decades, with $f_\nu \propto \nu^{-1.41}$ for $N_{\rm rh} = 50$ and $f_\nu \propto \nu^{-0.59}$ for $N_{\rm rh} = 500$. In the bottom-right panel, we show electron re-heating simulations for $\tau_{\rm initial} = 5$, $k_B T'_\gamma = $ 100 eV, $\gamma'_e \sim 50$. For $N_{\rm rh} = 5$, 50, there is a power-law spectrum above the peak energy for ~ 2 decades, with $f_\nu \propto \nu^{-1.00}$ for $N_{\rm rh} = 5$ and $f_\nu \propto \nu^{-0.44}$ for $N_{\rm rh} = 50$.

In summary, the main finding of considering electron re-heating is that there is only a $f_\nu \propto \nu^{-1}$ spectrum above the peak energy if a specific number if electron re-heating events are considered. If too few electron re-heating events are considered, there is still a sharp drop in f_ν after the peak energy and if too many electron re-heating events are considered, the high-energy spectrum will be shallower than $f_\nu \propto \nu^{-1}$.

3.6 Discussion of Results for the Comptonization of BB Photons

In this section, we first discuss an energy requirement the electrons must satisfy to have enough energy to transfer to the photons to produce a power-law spectrum above the peak-energy. This energy requirement is a necessary, but not a sufficient condition, to explain the production of a power-law spectrum above the peak-energy. To give a more detailed explanation for the simulation results, we calculate the number of photons upscattered to higher energies in a simulation and compare this to the number of photons needed to be upscattered to produce a power-law spectrum. After this calculation, we discuss the interpretation for the drop in f_ν by ~ 2 orders of magnitude, immediately after

the peak energy $E_{\rm pk}$, for the simulations with $k_B T'_\gamma \sim$ 30 eV $-$ 300 eV, one heating event, and $\tau_{\rm initial} = 2$. We also discuss the interpretation of the simulations with $k_B T'_\gamma =$ 30 eV and $\tau_{\rm initial}$ 8, 16, which show a power-law spectrum above $E_{\rm pk}$. We then apply this interpretation to the electron re-heating simulations with $k_B T'_\gamma = 100$ eV, 300 eV to estimate how many electron reheating events it takes to produce a power-law spectrum above $E_{\rm pk}$. Lastly, we discuss the dependence of the simulation results on the photon to electron ratio.

3.6.1 Energy Requirement for Power-Law Spectrum

In order to produce a power-law spectrum above the peak-energy, the electrons must have enough energy to transfer to the photons so they can populate a high-energy tail. A power-law spectrum can develop if the energy of a significant fraction of the photons near the BB peak-energy, $\sim 1/2$, can be increased by a factor ~ 2. Taking the number of photons near the BB peak to be $\sim N_\gamma$ (most of the photons are near the peak), the energy requirement the electrons must satisfy is

$$N_e m_e c^2 \gamma'_e \gtrsim 2(N_\gamma/2) k_B T'_\gamma \tag{3.10}$$

When considering $k_B T'_\gamma = 300$ eV and $k_B T'_\gamma = 100$ eV, we considered $\gamma'_e \sim 30$ and $\gamma'_e \sim 50$, respectively. For these two cases, for $N_\gamma/N_e \sim 10^5$ (as observed for the GRB prompt emission), the electrons just meet the energy requirement, making the production of a power-law spectrum difficult (in agreement with the results presented in the top two panels of Figure3.4). When considering $k_B T'_\gamma = 30$ eV, we considered $\gamma'_e \sim 80$. For this case, the energy in the electrons

is ~ 10 larger than the energy that needs to be transferred to the photons. Thus, the electrons have enough energy to transfer to the photons to produce a power-law spectrum for this case, in agreement with the results presented in the bottom-left panel of Figure3.4.

We now discuss a more detailed calculation to understand and interpret out simulation results.

3.6.2 Discussion of MC Simulation Results with One Heating Event

To understand our MC simulation results, we need to determine the number of photons that need to be upscattered to energies larger than $E_{\rm pk}$ to produce a power-law spectrum. We refer to this quantity as $N_{\rm pl}$. We then compare $N_{\rm pl}$ to the total number of photons that are upscattered to energies larger than $E_{\rm pk}$ in a MC simulation, which is given by the number of electrons in a simulation, N_e, multiplied by $N_{\rm Comp}$. $N_{\rm Comp}$ represent the number of scatterings it takes to cool an electron to a critical γ_e' at which Comptonization is no longer important. Thus, in order to produce a power-law above $E_{\rm pk}$, we need the condition

$$N_e N_{\rm Comp} \gtrsim N_{\rm pl} \tag{3.11}$$

to be satisfied. We now estimate $N_{\rm pl}$ and $N_{\rm Comp}$ for our MC simulations.

3.6.2.1 Estimating $N_{\rm pl}$

The number of photons in some bin with energy E, denoted as N_E, is given by

$$N_E = \frac{N_{\rm pk}}{E_{\rm pk}} \left(\frac{E}{E_{\rm pk}} \right)^{-\beta-1}. \tag{3.12}$$

In this equation, $N_{\rm pk}$ is the number of photons at $E_{\rm pk}$ and the spectral index β is defined in the f_ν sense, i.e. $f_\nu \propto \nu^{-\beta}$. To determine the total number of photons needed to produce a power-law above $E_{\rm pk}$, we integrate $N_E dE$ (sum over all the bins) from $E_{\rm pk}$ to infinity:

$$N_{\rm pl} = \int_{E'_{\rm pk}}^{\infty} \frac{N_{\rm pk}}{E_{\rm pk}} \left(\frac{E}{E_{\rm pk}} \right)^{-\beta-1} dE = \frac{N_{\rm pk}}{\beta}. \tag{3.13}$$

For the prompt emission, the typical high-energy spectral index is $\beta = 1.2$ (Preece et al., 2000). Thus, we approximate $N_{\rm pl} \sim N_{\rm pk}$. Since the majority of the photons in a simulation are near the peak of the BB spectrum, we approximate $N_{\rm pl} \sim N_{\rm pk} \sim N_\gamma$. With this result for $N_{\rm pl}$, we can rewrite the condition to produce a power-law above $E_{\rm pk}$ (Equation 3.11) in terms of the photon to electron ratio (N_γ/N_e):

$$N_{\rm Comp} \gtrsim \frac{N_\gamma}{N_e} \sim 1 \times 10^5. \tag{3.14}$$

In the above expression, we used $N_\gamma/N_e = 10^5$ for our MC simulations (Equation 3.2).

3.6.2.2 Condition for electron γ'_e at which Comptonization is no longer important

The Compton-Y parameter determines if the energy of a photon will change significantly after undergoing multiple scatterings with electrons in a optically thick medium. The expression for the Compton-Y parameter is (Rybicki & Lightman, 1979)

$$Y = 2\tau_{\rm initial} \times \max\left[\frac{4k_B T'_e}{m_e c^2}, \frac{4}{3}[(\gamma'_e)^2 - 1]\right], \tag{3.15}$$

where $2\tau_{\rm initial}$ is the average number of scatterings for each photon (Bégué et al., 2013) and the average fractional change of energy for a photon after a scattering event is either $4k_B T'_e/m_e c^2$ (for mildly-relativistic or sub-relativistic electrons) or $(4/3)[(\gamma'_e)^2 - 1]$ (for relativistic electrons), depending on the γ'_e of the electron. We take the transition from relativistic to mildly-relativistic speeds to occur at $\gamma'_e = 2$.

The condition Compton-$Y \gtrsim 1$ needs to be satisfied for Comptonization to be important. At the start of our MC simulations, Compton-$Y > 1$ since both $2\tau_{\rm initial}$ (we consider $\tau_{\rm initial} \geq 2$) and $\max[4k_B T'_e/m_e c^2, (4/3)([\gamma'_e]^2 - 1)]$ (we consider $\gamma'_e \geq 2$) are larger than one. However, as the simulations proceed, since $N_\gamma \gg N_e$, the electrons may cool to a point where Comptonization is no longer important. The critical condition at which Comptonization is no longer important is given by

$$2\tau_{\rm initial} \times \frac{4k_B T'_e}{m_e c^2} \sim 1. \tag{3.16}$$

Entering $k_B T'_e \sim m_e c^2(\gamma'_{e,\rm Comp} - 1)$, where $\gamma'_{e,\rm Comp}$ is the electron Lorentz factor

at which Comptonization is no longer important, we find

$$\gamma_{e,\mathrm{Comp}} = 1 + \frac{1}{8\tau_{\mathrm{initial}}}. \tag{3.17}$$

Thus, $\gamma_{e,\mathrm{Comp}} = 1.06$ for $\tau_{\mathrm{initial}} = 2$ and $\gamma_{e,\mathrm{Comp}} = 1.008$ for $\tau_{\mathrm{initial}} = 16$. With the value for $\gamma_{e,\mathrm{Comp}}$, we can now estimate N_{Comp}.

3.6.2.3 Estimating N_{Comp}

The final γ'_e ($\gamma'_{e,f}$) of an electron after a scattering event can be found from energy conservation (see Appendix B.5), which is given by

$$\gamma'_{e,f} = \frac{E'_{\gamma,i} - E'_{\gamma,f} + m_e c^2 \gamma'_{e,i}}{m_e c^2}, \tag{3.18}$$

where $E'_{\gamma,i}$ [$E'_{\gamma,f}$] is the photon energy before [after] the scattering event and $\gamma'_{e,i}$ is the electron Lorentz factor before the scattering event. As we discussed above, the average change of energy for a photon after a scattering event depends on whether $\gamma'_e > 2$ or $\gamma'_e < 2$ (Rybicki & Lightman, 1979):

$$E'_{\gamma,f} - E'_{\gamma,i} = \frac{4}{3}[(\gamma'_{e,i})^2 - 1]E'_{\gamma,i} \text{ , for } \gamma'_{e,i} > 2 \tag{3.19}$$

$$E'_{\gamma,f} - E'_{\gamma,i} = \frac{4k_B T'_e}{m_e c^2} E'_{\gamma,i} \qquad \text{, for } \gamma'_{e,i} < 2. \tag{3.20}$$

Substituting these expressions for $E'_{\gamma,f} - E'_{\gamma,i}$ into Equation 3.18, we can solve for the change in electron γ'_e after a scattering event in terms of $E'_{\gamma,i}$ and $\gamma'_{e,i}$:

$$\gamma'_{e,f} - \gamma'_{e,i} = -\frac{4E'_{\gamma,i}}{3m_e c^2}[(\gamma'_{e,i})^2 - 1] \text{ , for } \gamma'_{e,i} > 2 \tag{3.21}$$

$$\gamma'_{e,f} - \gamma'_{e,i} = -\frac{4E'_{\gamma,i}}{m_e c^2}[\gamma'_{e,i} - 1] \qquad \text{, for } \gamma'_{e,i} < 2. \tag{3.22}$$

In Equation 3.22, for $\gamma'_{e,i} < 2$, we used $k_B T'_e \sim m_e c^2(\gamma'_{e,i} - 1)$ for the electron temperature. If we define the change in electron γ'_e per scattering as $d\gamma'_e/dN$, we can re-write Equation 3.21 and Equation 3.22 in differential form:

$$\frac{d\gamma'_e}{dN} = -\frac{4E'_\gamma}{3m_e c^2}[(\gamma'_e)^2 - 1] \text{ , for } \gamma'_e > 2 \tag{3.23}$$

$$\frac{d\gamma'_e}{dN} = -\frac{4E'_\gamma}{m_e c^2}[\gamma'_e - 1] \quad \text{ , for } \gamma'_e < 2. \tag{3.24}$$

In the above expressions, E'_γ represents the energy of the photon in the jet-comoving frame before the scattering event. Solving these differential equations, we find

$$N_{\text{Cool,Rel}} = \frac{3m_e c^2}{8E'_\gamma} \ln\left[\frac{(\gamma'_{e,\text{MR}} + 1)(\gamma'_{e,i} - 1)}{(\gamma'_{e,\text{MR}} - 1)(\gamma'_{e,i} + 1)}\right] \text{ , for } \gamma'_{e,i} > 2 \tag{3.25}$$

$$N_{\text{Cool,MR}} = \frac{m_e c^2}{4E'_\gamma} \ln\left[\frac{(\gamma'_{e,i} - 1)}{(\gamma'_{e,\text{Comp}} - 1)}\right] \quad \text{ , for } \gamma'_{e,i} \leq 2. \tag{3.26}$$

In Equation 3.25, $N_{\text{Cool,Rel}}$ represents the number of scatterings it takes to cool a relativistic electron with $\gamma'_{e,i} > 2$ to $\gamma'_{e,\text{MR}} = 2$. After an electron cools below $\gamma'_{e,\text{MR}} = 2$, $N_{\text{Cool,MR}}$ represents the number of scatterings it takes to cool a mildly-relativistic (MR) electron from $\gamma'_{e,i} \leq 2$ to $\gamma'_{e,\text{Comp}}$.

For our simulations, we considered $\gamma'_{e,i} \geq 2$. If we consider $\gamma'_{e,i} > 2$, to compute N_{Comp}, we first need to compute the number of scatterings it takes to cool an electron to $\gamma'_{e,\text{MR}} = 2$ (Equation 3.25). Then, we need to compute the number of scattering it takes to cool an electron with $\gamma'_{e,i} = 2$ to $\gamma'_{e,\text{Comp}}$ (Equation 3.26). Thus, the number of scatterings it takes to cool a relativistic electron to $\gamma'_{e,\text{Comp}}$ (defined as $N_{\text{Comp,Rel}}$) is

$$N_{\text{Comp,Rel}} = N_{\text{Cool,Rel}}(\gamma'_{e,i} > 2) + N_{\text{Cool,MR}}(\gamma'_{e,i} = 2). \tag{3.27}$$

	$N_{\rm Cool,MR}(\gamma'_{e,i}=2)$ $\tau_{\rm initial}=2$	$N_{\rm Cool,MR}(\gamma'_{e,i}=2)$ $\tau_{\rm initial}=16$	$N_{\rm Cool,Rel}(\gamma'_{e,i}>2)$
$k_BT'_\gamma$ =30 eV	$\sim 10^4$	$\sim 2\times10^4$	$\sim 7\times10^3$ for $\gamma_{e,i}=80$
$k_BT'_\gamma$ =100 eV	$\sim 3\times10^3$	$\sim 6\times10^3$	$\sim 2\times10^3$ for $\gamma_{e,i}=50$
$k_BT'_\gamma$ =300 eV	$\sim 10^3$	$\sim 2\times10^3$	$\sim 7\times10^2$ for $\gamma_{e,i}=30$

Table 3.2: Values of $N_{\rm Comp}$ for the simulations we presented in Figures 3.2-3.4. $N_{\rm Comp,MR}$ and $N_{\rm Comp,Rel}$ were calculated with Equation 3.26 and Equation 3.27, respectively.

On the other hand, for a mildly-relativistic electron with $\gamma'_{e,i}\leq 2$, the number of scatterings it takes to cool an electron from $\gamma'_{e,i}$ to $\gamma'_{e,\rm Comp}$ (defined as $N_{\rm Comp,MR}$) is simply found by computing $N_{\rm Cool,MR}$ (Equation 3.26). We give a summary of the values of $N_{\rm Comp}$ for the simulations we presented in Figures 3.2-3.4 in Table 3.2. When using Equation 3.25 and 3.26 to calculate $N_{\rm Cool,Rel}$ and $N_{\rm Cool,MR}$, we assume $E'_\gamma\sim k_BT'_\gamma$, i.e. that the electrons cool mostly by scattering photons near the BB peak. This is not a bad approximation since most of the photons are near the BB peak.

3.6.2.4 Interpretation of MC Simulation Results with One Heating Event

From the estimates we provided in Table 3.2 for $N_{\rm Comp}$ at $\tau_{\rm initial}=2$, for $k_BT'_\gamma\sim 30$ eV $-$ 300 eV and initial $\gamma'_e\sim 2-80$, $N_{\rm Comp}\sim 2000-10000<(N_\gamma/N_e)$ (Equation 3.14). Thus, not enough photons are upscattered to energies above $E_{\rm pk}$ to produce a power-law spectrum. The fraction of photons that can be upscattered to energies larger than $E_{\rm pk}$ is given by

$$\text{Fraction of upscattered photons } = \frac{N_eN_{\rm Comp}}{N_\gamma}=\frac{N_{\rm Comp}}{(N_\gamma/N_e)}, \tag{3.28}$$

where $N_e N_{\rm Comp}$ is the total number of photons upscattered to energies larger that $E_{\rm pk}$ and N_γ is the number of photons near the peak of the BB spectrum. For $\tau_{\rm initial} = 2$, $N_{\rm Comp}/[N_\gamma/N_e] \sim 10^{-2}$. Since only $\sim 10^{-2}$ of the photons near the BB peak are upscattered to higher energies, this result explains why f_ν drops by ~ 2 orders of magnitude and then a power-law spectrum begins to develop (Figures 3.2-3.3).

We now apply our analytical estimates to the simulations results for $\tau_{\rm initial} = 16$ presented in Figure 3.4. For $k_B T'_\gamma \sim 100$ eV $- 300$ eV and $\tau_{\rm initial} = 16$, $N_{\rm Comp} \sim 3000 - 6000 < N_\gamma/N_e$ (Table 3.2). Thus, we do not expect a power-law spectrum to form above the peak energy, in agreement with the simulation results in Top-Left and Top-Right panels of Figure 3.4. For $k_B T'_\gamma =$ 30 eV and $\tau_{\rm initial} = 16$, $N_{\rm Comp} \sim 2 \times 10^4$ (Table 3.2). Since $N_{\rm Comp}$ is less that N_γ/N_e by a factor of 5, we do not expect a power-law spectrum to form above $E_{\rm pk}$. However, our analytical estimate assumes that the electrons only cool, and does not consider the possibility that an electron can gain energy by interacting with an energetic photon. If the γ'_e of the electron rises to $\gamma'_e \sim 2$, it can upscatter ~ 20000 more photons to higher energies since $N_{\rm Cool,MR} \sim 20000$ for $k_B T'_\gamma =$ 30 eV, $\gamma'_e = 80$, and $\tau_{\rm initial} = 16$ (Table 3.2). In Figure 3.6, we show the evolution of γ'_e for 3 electrons in the simulation. Initially, the 3 electrons cool from $\gamma'_e = 80$ to $\gamma'_e \sim 1$. However, there are ~ 5 instances where the γ'_e of the electron rises to $\gamma'_e \sim 2$. Thus, the number of photons that are upscattered to larger energies is increased by ~ 5, which give us $N_{\rm Comp} \sim N_\gamma/N_e$ (Equation 3.14), and explains why the $\tau_{\rm initial} = 16$ simulations in the Bottom-Left panel

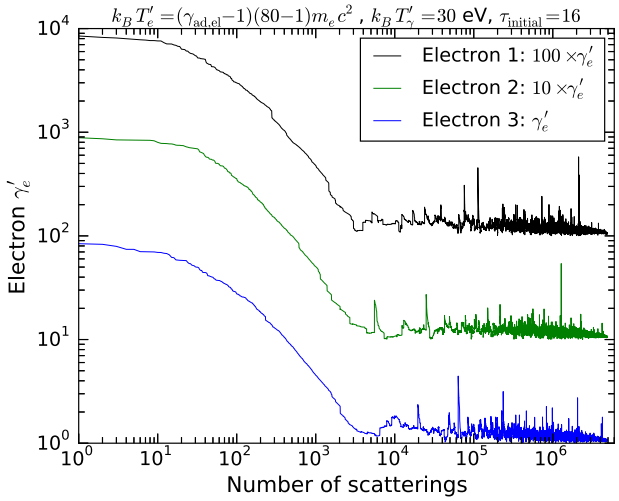

Figure 3.6: Evolution of γ'_e for 3 electrons from the $\tau_{\rm initial} = 16$ simulations shown in the Bottom-Left panel of Figure 3.4. The γ'_e of the electrons were offset by a factor of 10 to better see the evolution of γ'_e for each electron. Each of the spikes for γ'_e represents an episode when an electron interacts with an energetic photon, causing the energy of the electron to increase by a large factor.

of Figure 3.4 show a power-law spectrum above $E_{\rm pk}$.

3.6.3 Discussion of MC Simulation Results with Electron Reheating

In this subsection, we use the results for $N_{\rm pl}$ and $N_{\rm Comp}$ to understand the electron re-heating simulations with $k_B T'_\gamma = 100$ eV - 300 eV presented in Figure 3.5. We estimate $N_{\rm rh,min}$, the minimum number of re-heating events needed to produce a power-law spectrum above $E_{\rm pk}$.

3.6.3.1 Estimating $N_{\rm rh,min}$

With $N_{\rm rh}$ electron re-heating events, the number of photons that can be upscattered to higher energies is $\sim N_{\rm rh} N_e N_{\rm Comp}$. $N_{\rm rh,min}$ is found by the condition where just enough photons are upscattered to energies larger than $E_{\rm pk}$ to produce a power-law spectrum, i.e.

$$N_{\rm rh,min} N_e N_{\rm Comp} = N_{\rm pl}. \tag{3.29}$$

Using the result $N_{\rm pl} \sim N_\gamma$, the condition for $N_{\rm rh,min}$ can be re-written in terms of the photon to electron ratio:

$$N_{\rm rh,min} \sim \frac{N_\gamma / N_e}{N_{\rm Comp}}. \tag{3.30}$$

For $k_B T'_\gamma = 300$ eV and $\gamma'_{e,i} \sim 2 - 30$, $N_{\rm Comp} \sim 2000 - 3000$ (Table 3.2); thus we estimate $N_{\rm rh,min} \sim 30 - 50$. $N_{\rm rh,min}$ is within a factor of a few of the simulations in the top panels of Figure 3.5, which show a power-law above the peak-energy for $N_{\rm rh} \sim 20 - 100$. For $k_B T'_\gamma = 100$ eV and $\gamma'_{e,i} \sim 2 - 50$,

$N_{\rm Comp} \sim 5000 - 8000$ (Table 3.2); thus we estimate $N_{\rm rh,min} \sim 10 - 20$. $N_{\rm rh,min}$ is within a factor of a few of the simulations in the bottom panels of Figure 3.5, which show a power-law above the peak-energy for $N_{\rm rh} \sim 5 - 50$.

3.6.4 Dependence of Comptonization of Seed BB Simulation Results on N_γ/N_e

In this subsection, we perform a quick set of simulations at $\tau_{\rm initial} = 2$ to explore the dependence of the simulation results on N_γ/N_e. In the left panel (right panel) of Figure 3.7, we show simulations results for $k_B T'_\gamma =$ 300 eV, $\Gamma = 300$, $N_\gamma/N_e = 10^2, 10^3, 10^4, 10^5$, $\tau_{\rm initial} = 2$, and mono-energetic electrons with initial $\gamma'_e = 2$ ($\gamma'_e = 30$). For $N_\gamma/N_e = 10^2$ we considered $N_e = 10^6$, for $N_\gamma/N_e = 10^3$ we considered $N_e = 10^5$, etc. This was done to keep $N_\gamma = 10^8$ so that the simulation output spectrum can have more photons and thus a higher signal to noise. For initial $\gamma'_e = 2$ (left panel of Figure 3.7), the spectrum shows a sharp drop above the peak energy for $N_\gamma/N_e = 10^4$. For $N_\gamma/N_e = 10^3$, the spectrum shows a power-law with $f_\nu \propto \nu^{-1.60}$ and for $N_\gamma/N_e = 10^2$ the spectrum also shows a power-law with $f_\nu \propto \nu^{-0.80}$. For initial $\gamma'_e = 30$ (right panel of Figure 3.7), the spectrum shows a sharp drop above the peak energy for $N_\gamma/N_e = 10^4$. For $N_\gamma/N_e = 10^3$, there is a power-law spectrum $f_\nu \propto \nu^{-0.70}$ and for $N_\gamma/N_e = 10^2$ the spectrum is very shallow. The difference in the simulation results with N_γ/N_e can be understood from a energetics perspective. Equation 3.10, the minimum energy the electrons must have to transfer to the photons to produce a power-law spectrum, can be rewritten in

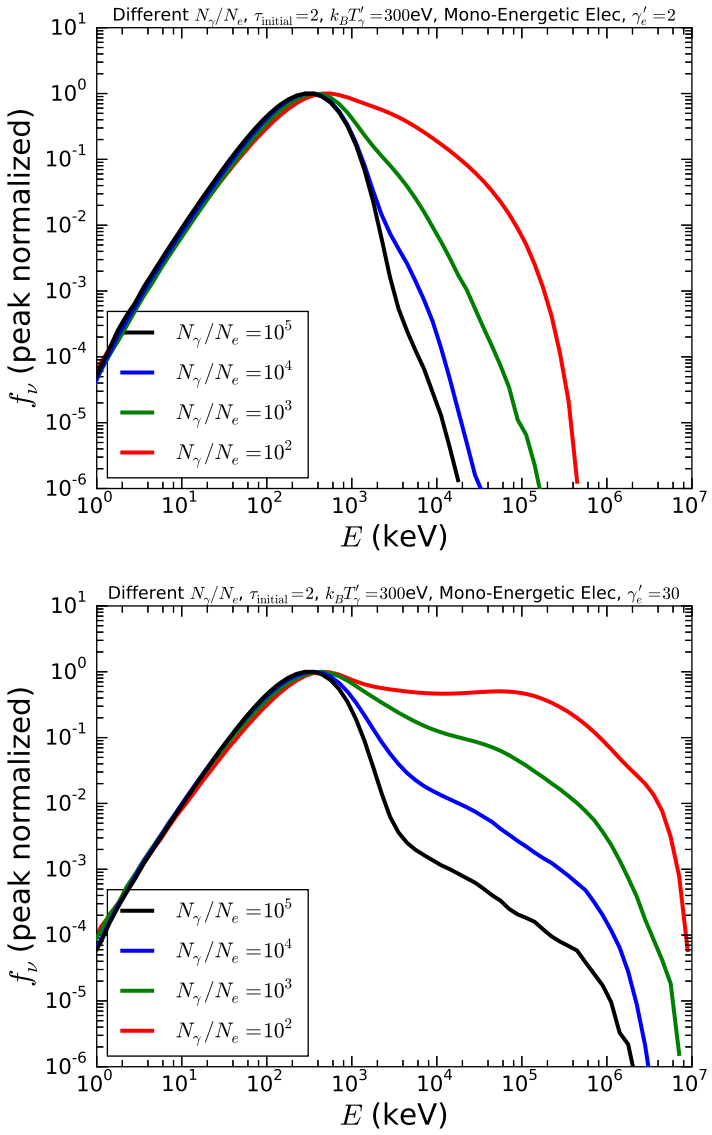

Figure 3.7: *Top Panel:* Simulation results for the Comptonization of seed BB photons with $k_BT'_\gamma =$ 300 eV, $\Gamma = 300$ with mildly relativistic electrons with initial $\gamma'_e = 2$, four different values for the photon to electron ratio, and $\tau_{\rm initial} = 2$. *Bottom Panel:* Same as Left Panel but with mono-energetic electrons with initial $\gamma'_e = 30$.

terms of the photon to electron ratio:

$$\frac{m_e c^2 \gamma'_e}{N_\gamma / N_e} \gtrsim k_B T'_\gamma. \tag{3.31}$$

Thus, for a fixed $k_B T'_\gamma$, an increase in N_γ/N_e makes it more difficult to produce a power-law spectrum above the peak-energy, as demonstrated in both panels of Figure 3.7. These results highlight the strong dependence of the simulation results on N_γ/N_e and the importance of performing simulations with $N_\gamma/N_e = 10^5$.

Lastly, we note that Lazzati & Begelman (2010) also show a couple of simulation results for mono-energetic electrons with $\gamma'_e = 2$, $\tau_{\rm initial} = 2$, and $N_\gamma/N_e = 10^4$ in their Figures 5-6. Their results for $N_\gamma/N_e = 10^4$ also show a significant dip above the peak energy by a factor ~ 50. However, our simulation results in the left panel of Figure 3.7 for $\gamma'_e = 2$ with $N_\gamma/N_e = 10^4$ display a drop in f_ν above $E_{\rm pk}$ by a factor ~ 100. This difference in the dip in f_ν above the peak energy can be explained by the fact that Lazzati & Begelman (2010) considered a value for $k_B T'_\gamma$ smaller than the $k_B T'_\gamma$ value we considered by a factor of 2. Since $N_{\rm Cool,MR} \propto 1/E'_\gamma$ (Equation 3.26), a smaller value for $k_B T'_\gamma$ by a factor of 2 implies that twice as many photons will be upscattered to larger energies (Equation 3.28). Thus, the $N_\gamma/N_e = 10^4$ presented in Lazzati & Begelman (2010) are consistent with our analytical estimates and with our simulation results for $N_\gamma/N_e = 10^4$.

3.7 Comptonization of Synchrotron $f_\nu \propto \nu^{-1/2}$ Spectrum

In this section, we consider a $f_\nu \propto \nu^{-1/2}$ seed spectrum, instead of BB seed spectrum, as expected for electrons producing synchrotron emission in the fast cooling regime (Ghisellini et al., 2000). We study how Comptonization modifies this spectrum with our MC photospheric code. In the next subsection, we describe the input parameters for these simulations.

3.7.1 Input Parameters for Simulations with Seed $f_\nu \propto \nu^{-1/2}$ Spectrum

For most of the input parameters, we considered the same values as those we considered for the Comptonization of a seed BB spectrum (discussed in Section 4.7.1.1). We considered $\Gamma = 300$, $L = 10^{52}$ ergs/sec, $\tau_{\rm initial} = 2$, 5, 8, 16, $N_e = 10^3$, $N_\gamma = 10^8$ to reach $N_\gamma/N_e = 10^5$, and $N_{\rm collect} = N_\gamma/3$. For the $f_\nu \propto \nu^{-1/2}$ seed spectrum, the input parameters are $E'_{1,\gamma}$ and $E'_{2,\gamma}$, the energy where the $f_\nu \propto \nu^{-1/2}$ spectrum begins and ends, respectively, in the jet-comoving frame. Thus, in the observer frame, the $f_\nu \propto \nu^{-1/2}$ spectrum begins and ends at $E_{1,\gamma} = \Gamma E'_{1,\gamma}$ and $E_{2,\gamma} = \Gamma E'_{2,\gamma}$. As we will discuss in the next subsection, the effect of Comptonizing a $f_\nu \propto \nu^{-1/2}$ spectrum is to flatten it to $f_\nu \propto \nu^0$, reminiscent of the low-energy spectrum of the prompt emission. Since the observed $f_\nu \propto \nu^0$ spectrum for the prompt emission extends from $\lesssim$ 10 keV to $E_{\rm pk} =$ 300 keV, we considered values of $E_{1,\gamma} <$ 10 keV and $E_{2,\gamma} = E_{\rm pk}$.Thus, we considered $E'_{1,\gamma} =$ 10 eV/Γ, 300 eV/Γ and $E'_{2,\gamma} =$ 300 keV/Γ. For the electron distribution, we considered MB electrons with $k_B T'_e \sim (20 -$

$1)m_e c^2$, $\sim (200-1)m_e c^2$, and $\sim (2000-1)m_e c^2$. Since the seed spectrum was only flattened to $f_\nu \propto \nu^0$ for $k_B T'_e \sim (2000-1)m_e c^2$, we only display the simulation results for this value of $k_B T'_e$. Lastly, we note that we do not consider electron re-heating, i.e. the electrons are only accelerated once at the start of the simulations.

3.7.2 Simulation Results for Comptonization of $f_\nu \propto \nu^{-1/2}$ Seed Spectrum

In the left panel (right panel) of Figure 3.8, we show the results for the Comptonization of a seed $f_\nu \propto \nu^{-1/2}$ spectrum with $E_{1,\gamma} = 10$ eV ($E_{1,\gamma} = 300$ eV), $E_{2,\gamma} = 300$ keV, MB electrons with $k_B T'_e \sim (2000-1)m_e c^2$, and $\tau_{\rm initial} = 2,\ 5,\ 8,\ 16$. In addition, in both panels, we also plot the energy spectrum $f_\nu = EN_E$ of the kinetic energies of the electrons in the observer frame, i.e. $m_e c^2(\gamma_e - 1)\Gamma$, at the end of each simulation. We will first discuss the results for the electron distributions. At the end of the $\tau_{\rm initial} = 2$ simulations, the electron distributions peak at $k_B T'_e \sim 100$ keV (in the jet-comoving frame) for both panels. As $\tau_{\rm initial}$ increases, $k_B T'_e$ doesn't change by much; at the end of the $\tau_{\rm initial} = 16$ simulation $k_B T'_e \sim 50$ keV for both panels. On the other hand, the photon spectrum changes significantly as $\tau_{\rm initial}$ increases. For both panels, at the end of the $\tau_{\rm initial} = 2$ simulations, most of the photons are still near $E_{1,\gamma}$, where most of the photons in the seed spectrum are initially present. However, as $\tau_{\rm initial}$ increases, more and more photons begin to be upscattered to energies $\sim 10^4$ keV. For both panels, at the end of the $\tau_{\rm initial} = 16$, the spectrum is flat from ~ 1 keV to $\sim 10^4$ keV. After $\sim 10^4$ keV, the spectrum declines rapidly

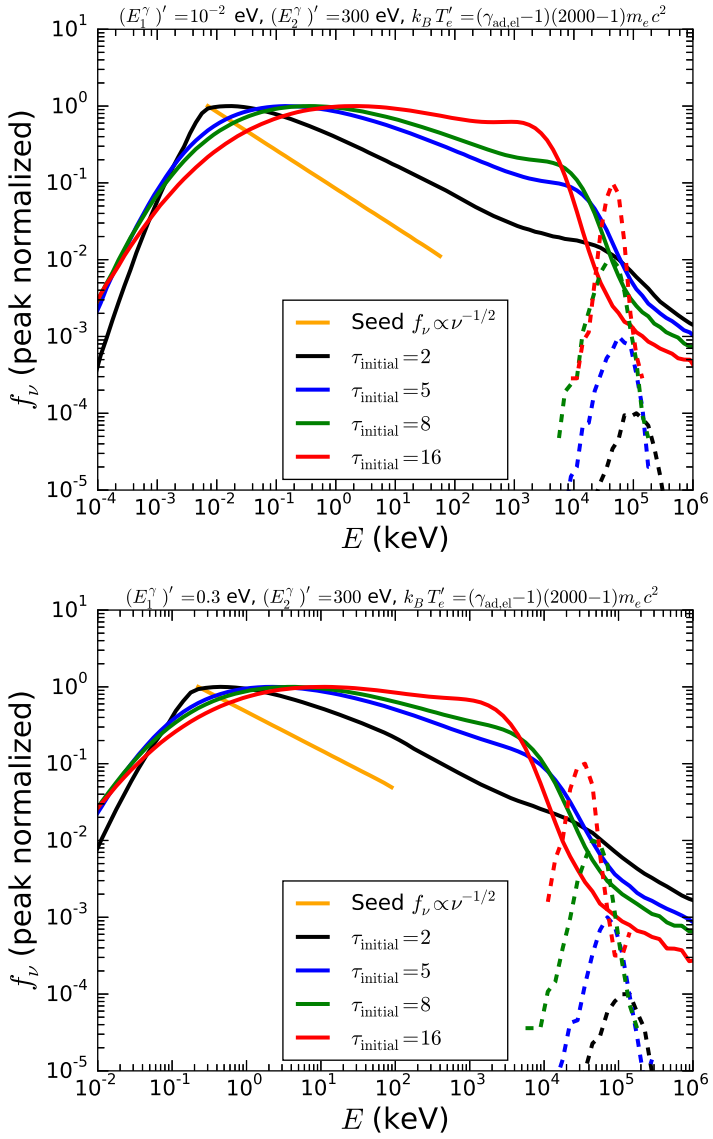

Figure 3.8: *Top Panel:* Simulation results for the Comptonization of a seed $f_\nu \propto \nu^{-1/2}$ spectrum ($E'_{1,\gamma} = 10^{-2}$ eV, $E'_{2,\gamma} = 300$ eV) with MB electrons with $k_B T'_e \sim (2000-1)m_e c^2$ and $\tau_{\rm initial} = 2$, 5, 8, 16. *Bottom Panel:* Same as Left Panel, but with $E_{1,\gamma} = 0.3$ eV.

for all of the simulations. After the rapid decline, there are a significant number of photons with energies $\gtrsim 10^5$ keV for all of the simulations. These photons remain at these energies since they are highly Klein-Nishina suppressed and cannot transfer their energy back to the electrons.

We now discuss the basic interpretation for the flattening of the spectrum as $\tau_{\rm initial}$ increases. From Equation 3.17, for $\tau_{\rm initial} = 16$, the γ_e' at which Comptonization is no longer important is $\gamma_{e,\rm Comp} = 1.008$. At the end of the $\tau_{\rm initial} = 16$ simulations, $k_B T_e' \sim$ 50 keV. Using $k_B T_e' \sim m_e c^2(\gamma_e - 1)$, $\gamma_e' \sim 1.1 > \gamma_{e,\rm Comp}$. Thus, Comptonization is still important for the $\tau_{\rm initial} = 16$ simulations and the photons are still gaining energy from the electrons. The photons will gain energy from the electrons until they reach the energy of the electrons. For the seed $f_\nu \propto \nu^{-1/2}$ spectrum, initially there are more photons at lower energies near $E_{1,\gamma}$. However, as $\tau_{\rm initial}$ increases, the additional scatterings allow for more photons at lower energies to be upscattered to higher energies and they also allow for more photons to reach the energy of the electrons. The spectrum flattens because more photons are being removed from lower energies and being placed at high energies near the energy of the electrons. If we considered $\tau_{\rm initial} > 16$, if Compton-Y remains greater than 1, eventually all the photons will be upscattered to energies close to the energy of the electrons. The photon spectrum will no longer look flat, but will instead be peaked at the energy of the electrons.

Lastly, we note that although the simulation output spectra for $\tau_{\rm initial} = 16$ in both panels of Figure 3.8 are very similar to the low-energy spectrum for

the prompt emission, these simulation results cannot explain it. The spectrum peaks at the energy of the electrons, which have an energy ~ 50 keV in the jet-comoving frame and thus an energy ~ 50 keV $\times 300 \sim 10^4$ keV in the observer frame ($\Gamma = 300$). In order for the spectrum to break at ~ 300 keV in the observer frame, the electrons would need to have an energy ~ 1 keV in the jet-comoving frame.

3.8 Conclusions

In this work, we presented our methodology for our MC photospheric code and our simulation results for a wide parameter space with a realistic photon to electron ratio $N_\gamma/N_e = 10^5$, as expected for the GRB prompt emission. Our goal was to determine if the photospheric process can explain the observed high-energy spectrum $f_\nu \propto \nu^{-1.2}$ of the prompt emission. For these simulations, we considered the Comptonization of a seed BB spectrum. If electron re-heating is not considered, we determined that considering both low photon temperatures and large optical depths $\sim 10 - 20$ is best for producing a power-law spectrum above the BB peak energy for the following two reasons: 1. low temperature photons cool electrons more slowly, allowing more photons to be upscattered to higher energies. 2. At larger optical depths, the average number of scatterings a photon experiences is larger, allowing for more photons to be upscattered to higher energies. On the other hand, the output spectrum for the cases we considered with higher photon temperatures and low optical depths display a sharp drop in f_ν above the peak energy by ~ 2 orders

of magnitude. These cases require additional energy in the electrons and we demonstrated that if we consider electron re-heating, a power-law spectrum above the peak-energy can be produced.

One issue with the simulations with a low photon temperature and a large optical depth is that it may be difficult to match the peak-energy of the prompt emission since adiabatic cooling of photons decreases the BB peak-energy by a large factor for large optical depths. Thus, considering electron re-heating near the photosphere with a large photon temperature ($\sim$ 100 keV in the observer frame) may be the best solution for explaining the prompt emissions observations with the photospheric model.

We also performed photospheric simulations for different values of N_γ/N_e and demonstrated that the simulation results have a strong dependence on the photon to electron ratio. This result highlights the important of performing realistic photospheric simulations with $N_\gamma/N_e = 10^5$.

In addition, we also used our MC photospheric code to study how Comptonization modifies a $f_\nu \propto \nu^{-1/2}$ seed spectrum, as expected for synchrotron when electrons are in the fast cooling regime. For large optical depths, the effect is to flatten the spectrum to $f_\nu \propto \nu^0$, reminiscent of the low-energy spectrum of the Band function. However, these simulation results cannot explain the low-energy spectrum of the prompt emission since the simulation output spectrum peaks at $\sim 10^4$ keV, much larger than the ~ 300 keV peak energy of the prompt emission.

Chapter 4

Constraining The X-ray Flare Mechanism with Optical Observations

4.1 Abstract

We study Gamma-Ray Burst (GRB) X-ray flares with coincident optical observations during the X-ray flare. For 8 X-ray flares, we determined that the X-ray flare peak-flux, extrapolated to the optical band with a $f_\nu \propto \nu^{1/3}$ optically-thin Synchrotron/SSC (Synchrotron Self-Compton) spectrum, over-produces the observed optical flux by a factor $\gtrsim 2$. Thus, the synchrotron and SSC processes require a self-absorption break between the optical and the X-ray band to be compatible with the optical observations. We performed a parameter space search for synchrotron, SSC, synchrotron from a Poynting jet, and Monte Carlo simulations for the photospheric process to determine if these mechanisms can explain the flare observations. Synchrotron and SSC face problems: the variability time of the synchrotron solutions is much shorter than the observed flare variability time and the synchrotron component of SSC over-produces the observed optical flux. Synchrotron from a Poynting jet and the Photospheric process both have a wide parameter space that explains the flare observations. Thus, a Poynting jet and a baryonic jet can both explain the X-ray flare observations, with the photospheric process being the best

candidate for a baryonic jet.

4.2 Introduction

One of the most puzzling observations provided by the *Swift* satellite (Gehrels et al., 2004a) is the observation of erratic episodes of rebrightenings in the X-ray light curve following the prompt gamma-ray emission, known as X-ray flares (Burrows et al., 2005a). X-ray flares have been detected for $\sim 33\%$ of long GRBs and for $\sim 13\%$ of short GRBs (Chincarini et al., 2007, 2010; Bernardini et al., 2011; Margutti et al., 2011). During a X-ray flare episode, the flux increases by a factor $\sim 1 - 10^3$ and there are many cases where a GRB is seen to display multiple X-ray flares. The rapid rise time of the flux, with $\Delta t/t_{\rm pk} \sim 0.1$, where Δt is the duration of the flare and $t_{\rm pk}$ is the time when the flare peaks, rules out the external-forward shock as the mechanism for X-ray flares (Lazzati & Perna, 2007). Thus, X-ray flares are believed to be due to re-activation of the central engine after the prompt emission (King et al., 2005; Perna et al., 2006; Proga & Zhang, 2006; Rosswog, 2007; Lee et al., 2009; Dai et al., 2006b; Wang & Dai, 2013).

In addition to the open question on how to restart the central engine to power X-ray flares, another key open question is, what is the X-ray flare radiation mechanism? Detailed spectral studies of X-ray flares have revealed that flares have similarities to prompt gamma-ray pulses (Butler & Kocevski, 2007a; Margutti et al., 2010; Sonbas et al., 2013). Thus, understanding the X-ray flare radiation mechanism may help us understand the prompt radia-

tion mechanism, one of the long standing questions in the GRB field. One of the main challenges for studying the X-ray flare mechanism is that except in a few cases (Krühler et al., 2009; Abdo et al., 2011; Li et al., 2012; Swenson et al., 2013; Swenson & Roming, 2013), there is no signal associated with X-ray flares in other bands. In particular, it is surprising that no signal associated with X-ray flares is detected in the optical band since the UVOT (Ultra-Violet/Optical Telescope, Roming et al. (2005)) on-board the *Swift* satellite and many rapid-response ground based optical facilities have taken high quality optical observations during X-ray flare episodes (e.g. Cenko et al., 2009; Rykoff et al., 2009; Uehara et al., 2010; Gorbovskoy et al., 2012; Kopač et al., 2013; Zaninoni et al., 2013; Melandri et al., 2014).

In this work, we focus on bursts that have optical observations coincident with the flare to constrain the X-ray flare radiation mechanism. To use the coincident optical observations, we take the peak-flux of the X-ray flare and extrapolate it to the optical band and compare it to the observed optical flux. Taking the X-ray flare emission to peak in the X-ray band, the optically-thin synchrotron and SSC (Synchrotron Self-Compton) processes both predict $f_\nu \propto \nu^{1/3}$ below the peak, where f_ν is the flux per unit frequency ν. For 8 X-ray flares, we found that the predicted flux for optically thin synchrotron/SSC over-predicts the observed optical flux by a factor $\gtrsim 2$. Thus, in order to not over-produce the observed optical flux, synchrotron and SSC require a self-absorption break between the optical and the X-ray band. We perform a parameter space search to determine if the synchrotron and SSC processes

can produce a self-absorption break between the optical and X-ray band. In addition, we also perform a parameter space search for synchrotron emission from a magnetized jet and we perform Monte Carlo simulations of the photospheric process to determine if these processes can explain the X-ray flare observations.

This manuscript is organized as follows. In Section 4.3, we describe the extrapolation of the X-ray flare peak flux to the optical band in more detail and we present our sample of 8 flares that require a self-absorption break between the optical band and the X-ray band (observations are shown in Appendix C). In Section 4.4, Section 4.5, and Section 4.6 we discuss the results for our parameter space search for synchrotron, SSC, and synchrotron from a Poynting jet, respectively. In Section 4.7, we discuss the results of our Monte Carlo simulations for the photospheric process. Lastly, in Section 4.8, we discuss our conclusions.

4.3 X-ray Flares with Self-Absorption break between Optical and X-ray band

4.3.1 Extrapolating X-ray flare peak-flux to Optical band

We performed a literature search for X-ray flares that have a measured spectrum, optical observations coincident with the X-ray flare episode, and a measured redshift. A number of studies have used observations from *Swift's* XRT (X-ray Telescope, Burrows et al. 2005b), which has an observing band from 0.3-10 keV, to determine the spectrum for X-ray flares with high signal

to noise (e.g. Falcone et al., 2006; Pagani et al., 2006; Goad et al., 2007; Morris et al., 2007; Butler & Kocevski, 2007a; Falcone et al., 2007; Margutti et al., 2010; Chincarini et al., 2010). The two models that best fit the X-ray flare spectrum are the Band function (Band et al., 1993) and a single-power law (Falcone et al., 2007), with most flares being better fit by a single power-law. In addition, some studies have found a photospheric component in the X-ray flare spectrum (Larsson et al., 2011; Friis & Watson, 2013). The spectrum of the 8 X-ray flares in our sample were better fit by either a Band function or a single power-law.

To extrapolate the X-ray flare emission to the optical band, we obtained the peak specific flux for each X-ray flare at 10 keV, $f_{\rm 10keV}$, from the XRT lightcurves in Evans et al. (2010)[1]. For the X-ray flares with a Band function spectrum, we used the spectral index above $E_{\rm pk}$ (peak energy of Band function) to extrapolate $f_{\rm 10keV}$ to $E_{\rm pk}$. Below $E_{\rm pk}$, we used a $f_\nu \propto \nu^{1/3}$ spectrum to extrapolate to the optical band[2]. Defining the extrapolated flux to the optical band as $f_{\rm 2eV,pred}$ and defining the spectral index above $E_{\rm pk}$ in the f_ν sense as $\beta_{\rm B}$ ($f_\nu \propto \nu^{-\beta_{\rm B}}$), $f_{\rm 2eV,pred} = f_{\rm 10keV}(E_{\rm pk}/10{\rm keV})^{-\beta_B}(2{\rm eV}/E_{\rm pk})^{1/3}$. For the X-ray flares with a single power-law spectrum, we used the observed spectral index, β, to extrapolate $f_{\rm 10keV}$ to 0.3 keV, the low-energy end of the XRT band. The observed spectrum of the X-ray flare likely extends below 0.3 keV, but to be conservative in the extrapolation to the optical band,

[1]http://www.swift.ac.uk/burst_analyser/

[2]Most X-ray flares in our sample have $E_{\rm pk} \sim$ 1keV and the energy range 0.3 keV - $E_{\rm pk}$ is too narrow to determine the low-energy spectral index accurately.

we assumed $f_\nu \propto \nu^{1/3}$ between 2 eV and 0.3 keV. For these X-ray flares, $f_{\rm 2eV,pred} = f_{\rm 10keV}(0.3{\rm keV}/10{\rm keV})^{-\beta}(2{\rm eV}/0.3{\rm keV})^{1/3}$.

4.3.2 Sample of X-ray flares

In Appendix C, we show the optical and X-ray light curves for the 8 flares in our sample. In Table 4.1, we show some of the observational properties for these 8 X-ray flares: $t_{\rm rise}$ (rise time of flare), $t_{\rm pk}$ (time when flare peaks), z (redshift of burst), d_{L28} (luminosity distance in units of 10^{28} cm), $L_{X,50}$ (peak luminosity of the flare radiated in X-rays in units of 10^{50} ergs/sec), and $f_{\rm 2eV,corr}$ (optical flux at 2 eV, corrected for both Galactic extinction and host galaxy extinction). We also give the reference information for the optical data and the X-ray flare spectrum.

4.3.3 Flare Properties Used for Parameter Space Search

The flares in our sample can be divided into three categories: flares with a Band functions spectrum, flares with a single power-law $f_\nu \propto \nu^{-0.5}$ (GRB 060714 and GRB 080310), and flares with a single power-law spectrum steeper than $f_\nu \propto \nu^{-0.5}$ (GRB 051117A and GRB 081008). In order to describe the properties of all the flares in our sample. we will perform the parameter space search for 4 flares in our sample: GRB 060904B and GRB 061121 (both with Band function spectrum), GRB 080310, and GRB 081008.

4.4 Synchrotron Parameter Space Search

We now discuss our strategy for searching the 5D synchrotron parameter space to determine if there are solutions with ν_a between the optical band and X-ray band.

4.4.1 Methodology for Synchrotron Parameter Space Search

The 5 parameters that describe a synchrotron source are (Kumar & McMahon, 2008; Beniamini & Piran, 2013): the radius of emission R, the magnetic field strength B, the number of emitting electrons N_e, the bulk Lorentz factor of the source Γ, and taking the radiating electrons to follow a power-law distribution $dN_e/d\gamma_e \propto \gamma_e^{-p}$ (γ_e is the Lorentz factor of the electrons and p is a constant known as the electron-index), the fifth parameter is γ_i, the minimum Lorentz factor electrons must have to follow this power-law distribution. To search this 5D parameter space, we allow the following 5 parameters to be free: Γ, the flare variability time Δt, and the electron Lorentz factors γ_i, γ_a, and γ_c, corresponding to electrons radiating photons with frequencies ν_i, ν_a, and ν_c respectively, where ν_c is the cooling frequency. In addition, we also calculate the Compton-Y parameter to include inverse Compton (IC) cooling of electrons. By letting Γ, Δt, γ_i, γ_a, γ_c be free, we already know 2 of the 5 parameters that describe a synchrotron source (Γ and γ_i). We now describe how we use Γ, Δt, γ_i, γ_a, γ_c to compute R, B, N_e and the Compton-Y parameter.

With Γ and Δt, we can compute the radius of emission with the ex-

pression

$$R = 2c\Delta t\Gamma^2(1+z)^{-1}, \tag{4.1}$$

where c is the speed of light. Next, we use γ_c to compute B in terms of Compton-Y. The expression for γ_c, the electron Lorentz factor for electrons cooling on a dynamical timescale $t_{\rm dyn} = [R(1+z)]/(2c\Gamma^2)$ (in the observer frame), is

$$\gamma_c = \frac{6\pi m_e c}{\sigma_T} t_{\rm dyn}^{-1}\Gamma^{-1}B^{-2}(1+z) \times \begin{cases} (1+Y)^{-1} & \gamma_a < \gamma_c \\ (\chi(\gamma_c/\gamma_a)+Y)^{-1} & \gamma_c < \gamma_a. \end{cases} \tag{4.2}$$

In this equation, σ_T is the Thomson cross-section. When $\gamma_c < \gamma_a$, the source cannot cool by synchrotron since the synchrotron emission is self-absorbed (Granot et al., 2000; Panaitescu & Mészáros, 2000; Gao et al., 2013); thus, the cooling of electrons is dominated by IC scattering. In this regime, we calculate γ_c as in Panaitescu & Mészáros (2000). When $\gamma_c < \gamma_a$, the $(1+Y)^{-1}$ term is modified by an optical depth term: $\gamma_c \propto (\chi(\gamma_c/\gamma_a)+Y)^{-1}$, where $\chi = 1 - \exp(-\gamma_c/\gamma_a)$ (Panaitescu & Mészáros, 2000). With Equation 4.2, we can solve for B in terms of Compton-Y:

$$B = \left(\frac{6\pi m_e c}{\sigma_T}\right)^{1/2} (t_{\rm dyn})^{-1/2}\Gamma^{-1/2}(1+z)^{1/2}\gamma_c^{-1/2} \times \begin{cases} (1+Y)^{-1/2} \\ (\chi(\gamma_c/\gamma_a)+Y)^{-1/2} \end{cases}. \tag{4.3}$$

Next, we compute N_e in terms of Compton-Y. N_e enters into the synchrotron expressions from f_{ν_p}, the peak flux of the f_ν spectrum:

$$f_{\nu_p} = \frac{\sqrt{3}e^3}{4\pi m_e c^2} B N_e \Gamma d_L^{-2}(1+z). \tag{4.4}$$

To solve for N_e, we enter f_{ν_p} (Equation 4.4) into the expression for ν_a. The expression for ν_a depends on the ordering of γ_i, γ_a, γ_c; we list each expression for ν_a below (Gou et al., 2007; Shen & Zhang, 2009; Zhao et al., 2010):

$$\nu_a = \begin{cases} \left(\frac{1}{2m_e}\right)^{\frac{3}{5}} f_{\nu_p}^{\frac{3}{5}} d_L^{\frac{6}{5}} R^{-\frac{6}{5}} \Gamma^{\frac{3}{5}} (1+z)^{-\frac{9}{5}} \gamma_i^{-\frac{3}{5}} \nu_i^{-\frac{1}{5}} & \gamma_a < \gamma_i < \gamma_c \\ \left(\frac{e}{8\pi m_e^3 c}\right)^{\frac{1}{p+4}} f_{\nu_p}^{\frac{2}{p+4}} d_L^{\frac{4}{p+4}} R^{-\frac{4}{p+4}} \Gamma^{\frac{3}{p+4}} (1+z)^{-\frac{7}{p+4}} \nu_i^{\frac{p-1}{p+4}} B^{\frac{1}{p+4}} & \gamma_i < \gamma_a < \gamma_c \\ \left(\frac{1}{2m_e}\right)^{\frac{3}{5}} f_{\nu_p}^{\frac{3}{5}} d_L^{\frac{6}{5}} R^{-\frac{6}{5}} \Gamma^{\frac{3}{5}} (1+z)^{-\frac{9}{5}} \gamma_c^{-\frac{3}{5}} \nu_c^{-\frac{1}{5}} & \gamma_a < \gamma_c < \gamma_i \\ \left(\frac{e}{8\pi m_e^3 c}\right)^{\frac{1}{6}} f_{\nu_p}^{\frac{1}{3}} d_L^{\frac{2}{3}} R^{-\frac{2}{3}} \Gamma^{\frac{1}{2}} (1+z)^{-\frac{7}{6}} B^{\frac{1}{6}} \nu_c^{\frac{1}{6}} & \gamma_c < \gamma_a < \gamma_i \\ \left(\frac{e}{8\pi m_e^3 c}\right)^{\frac{1}{p+5}} f_{\nu_p}^{\frac{2}{p+5}} \left(\frac{d_L}{R}\right)^{\frac{4}{p+5}} \Gamma^{\frac{3}{p+5}} (1+z)^{\frac{-7}{p+5}} B^{\frac{1}{p+5}} \nu_i^{\frac{p-1}{p+5}} \nu_c^{\frac{1}{p+5}} & \max(\gamma_i, \gamma_c) < \gamma_a \end{cases} \tag{4.5}$$

When solving for N_e with Equation 4.5, we also enter $\nu_i = [e/(2\pi m_e c)] B \gamma_i^2 \Gamma (1+z)^{-1}$, $\nu_a = [e/(2\pi m_e c)] B \gamma_a^2 \Gamma (1+z)^{-1}$, and $\nu_c = [e/(2\pi m_e c)] B \gamma_c^2 \Gamma (1+z)^{-1}$. Simplifying this result, N_e in terms of Compton-Y is given by

$$N_e = \left(\frac{2}{\sqrt{3}\pi e}\right) R^2 B \times \begin{cases} \gamma_i^{5/3} \gamma_a^{10/3} & \gamma_a < \gamma_i < \gamma_c \\ \gamma_i^{-(p-1)} \gamma_a^{p+4} & \gamma_i < \gamma_a < \gamma_c \\ \gamma_c^{5/3} \gamma_a^{10/3} & \gamma_a < \gamma_c < \gamma_a \\ \gamma_c^{-1} \gamma_a^{6} & \gamma_c < \gamma_a < \gamma_i \\ \gamma_c^{-1} \gamma_i^{-(p-1)} \gamma_a^{p+5} & \max(\gamma_i, \gamma_c) < \gamma_a \end{cases} \tag{4.6}$$

In these expressions, the dependence of N_e on Compton-Y comes from B (Equation 4.3). With N_e in terms of Compton-Y, we can now solve for Compton-Y.

The Compton-Y parameter is given by the expression

$$Y = \frac{4}{3}\left(\frac{\sigma_T N_e}{4\pi R^2}\right)\frac{\int_{N_e}\gamma_e^2 N_{\gamma_e}\,\mathrm{d}\gamma_e}{N_e}, \tag{4.7}$$

where $\tau_e = \sigma_T N_e/(4\pi R^2)$ is the optical depth to electron-scattering. The term $\int_{N_e}\gamma_e^2 N_{\gamma_e}\,\mathrm{d}\gamma_e/N_e$ represents the 2nd moment of the electron distribution divided by the total number of electrons, which can be determined from the electron distribution. Taking $p > 2$, the expressions for the electron distribution for the slow cooling ($\gamma_i < \gamma_c$) and the fast cooling ($\gamma_c < \gamma_i$) cases are given by

$$N_{\gamma_e} = \begin{cases}(p-1)\gamma_i^{-(p-1)}\gamma_e^{-p}N_e & \gamma_i < \gamma_e < \gamma_c \\ (p-1)\gamma_i^{-(p-1)}\gamma_c\gamma_e^{-p-1}N_e & \gamma_c < \gamma_e\end{cases} \tag{4.8}$$

$$N_{\gamma_e} = \begin{cases}\gamma_c\gamma_e^{-2}N_e & \gamma_c < \gamma_e < \gamma_i \\ \gamma_i^{-(p-1)}\gamma_c\gamma_e^{-p-1}N_e & \gamma_i < \gamma_e\end{cases} \tag{4.9}$$

Taking the 2nd moment of the electron distributions, we find

$$\frac{\int_{N_e}\gamma_e^2 N_{\gamma_e}\,\mathrm{d}\gamma_e}{N_e} = \begin{cases}(p-1)\gamma_i^{(p-1)}\left[\frac{\gamma_c^{3-p}}{(3-p)(p-2)} - \frac{\gamma_i^{3-p}}{(3-p)}\right] & \gamma_i < \gamma_c \\ \gamma_c(\gamma_i - \gamma_c) + \frac{\gamma_c\gamma_i}{p-2} & \gamma_c < \gamma_i\end{cases}. \tag{4.10}$$

Entering the values for $\int_{N_e}\gamma_e^2 N_{\gamma_e}\,\mathrm{d}\gamma_e/N_e$ into Equation 4.7, entering B (Equation 4.3) into the N_e (Equation 4.6), and entering N_e into Equation 4.7, Equation 4.7 now only depends on the Compton-Y parameter and on our free parameter Γ, Δt, γ_i, γ_a, γ_c. This allows us to solve Equation 4.7 numerically to determine Compton-Y. With Compton-Y, we can now find B (Equation 4.3) and N_e (Equation 4.6). Thus, we now have all the parameters that describe a synchrotron source and we use them to compute ν_a (Equation 4.5) to determine if it is between the optical and X-ray band.

4.4.2 Free Parameter Ranges for 5D Parameter Space Search

We consider a very broad space for the 5D parameter space search. The range we consider for each parameter is: $2 < \Gamma < 1000$, 10^{-4} sec $< \Delta t < 10^2$ sec, $2 < \gamma_a < 10^6$, $2 < \gamma_i < 10^6$, and $2 < \gamma_c < 10^6$.

4.4.3 Constraints for Valid Synchrotron Solutions

In addition to producing ν_a between the optical and X-ray band, we also require that synchrotron solutions match the observed spectral index, the observed X-ray flux, and have an optical flux below the observed optical flux. Above the peak energy of the f_ν spectrum, the synchrotron spectrum is either $f_\nu \propto \nu^{-p/2}$ (satisfied when $\max(\nu_a, \nu_i, \nu_c) < \nu$), $f_\nu \propto \nu^{-(p-1)/2}$ (satisfied when $\max(\nu_a, \nu_i) < \nu < \nu_c$), or $f_\nu \propto \nu^{-0.5}$ (satisfied when $\max(\nu_a, \nu_c) < \nu < \nu_i$) (Granot & Sari, 2002). Thus, for three of the four flares we consider for our parameter space search (Section 4.3.3), which have a spectrum $f_\nu \propto \nu^{-1.47}$, $f_\nu \propto \nu^{-1.4}$, $f_\nu \propto \nu^{-1.51}$ (GRB 060904B, 061121, 081008, respectively), we consider both $f_\nu \propto \nu^{-p/2}$ and $f_\nu \propto \nu^{-(p-1)/2}$ when fitting their spectrum, with p determined from the spectral index. For GRB 080310, the $f_\nu \propto \nu^{-0.5}$ segments are used to fit the observed $f_\nu \propto \nu^{-0.476}$ spectrum. When $\beta = 0.5$, the spectral index cannot be used to determine p. From Table 4.1, a typical spectral index for the flares in our sample is $\beta = 1.4$. Thus, we consider both $p = 2.8$ and $p = 3.8$ for GRB 080310.

For the flares that are better fit by a Band function, we require f_{ν_p} to match $f_{E_{\rm pk}} = f_{10{\rm keV}}(10 \text{ keV}/E_{\rm pk})^{-\beta_B}$ within a factor of 2. We also require

the peak energy of the f_ν synchrotron spectrum, ν_i, ν_a, or ν_c, depending on the ordering of γ_i, γ_a, or γ_c, to match $E_{\rm pk}$ within a factor of 2. On the other hand, for the flares with a single power-law spectrum, the peak energy lies between 2 eV and 0.3 keV. For these flares, we extrapolate the flux at f_{ν_p} to 0.3 keV and require it to match $f_{0.3{\rm keV}} = f_{10{\rm keV}}(0.3\ {\rm keV}/10\ {\rm keV})^{-\beta}$ within a factor of 2. For the parameter space determined to have ν_a between the optical and the X-ray band, we use the synchrotron spectrum to find the flux at 2 eV. Below the peak energy, $f_\nu \propto \nu^{1/3}$ for $\nu_a < \nu < \min(\nu_i, \nu_c)$, $f_\nu \propto \nu^2$ for $\nu < \min(\nu_a, \nu_i)$, and $f_\nu \propto \nu^{5/2}$ for $\nu_i < \nu < \nu_a$ (Granot & Sari, 2002). We require the synchrotron flux at 2 eV to be below the observed optical flux $f_{\rm 2eV,cor}$.

In addition to describing the optical and X-ray observations, we also require that the IC component does not violate energy requirements. The energy radiated in X-rays for the flares in our sample is $\sim 10^{51} - 10^{52}$ ergs. If $Y > 1$, the energy in the IC component is larger than the energy in the synchrotron component by a factor of Y. In addition, if the 1st IC scattering is not Klein-Nishina (KN) suppressed, there will be a 2nd IC scattering, which will carry an energy larger than the synchrotron component by a factor Y^2. Multiple IC scatterings will continue, each carrying an energy larger than the previous IC scattering by a factor of Y, until the IC emission is KN suppressed, i.e. the condition $\nu_{\rm syn}(4\gamma_e^2)^N\gamma_e > m_e c^2\Gamma$, where N refers to the Nth IC scattering and $\nu_{\rm syn}$ refers to the peak energy of the f_ν synchrotron spectrum.

If $Y < 1$, we do not consider additional IC scatterings. If $Y > 1$, we

consider a synchrotron solution to be valid if $Y < 1000$ (to keep the energy budget below $\sim 10^{54} - 10^{55}$ ergs) and the 2nd IC scattering is KN suppressed. If the 2nd IC scattering is not KN suppressed, we include a 2nd IC scattering in our methodology by adding a Y^2 term to the γ_c equation (Zhao et al., 2010):

$$\gamma_c = \frac{6\pi m_e c}{\sigma_T} t_{\rm dyn}^{-1} \Gamma^{-1} B^{-2} (1+z) \times \begin{cases} (1+Y+Y^2)^{-1} & \gamma_a < \gamma_c \\ (\chi(\gamma_c/\gamma_a)+Y+Y^2)^{-1} & \gamma_c < \gamma_a. \end{cases} \quad (4.11)$$

Thus, B in terms of Compton-Y is given by

$$B = \left(\frac{6\pi m_e c}{\sigma_T}\right)^{1/2} (t_{\rm dyn})^{-1/2} \Gamma^{-1/2} (1+z)^{1/2} \gamma_c^{-1/2} \times \begin{cases} (1+Y+Y^2)^{-1/2} \\ (\chi(\gamma_c/\gamma_a)+Y+Y^2)^{-1/2} \end{cases} \quad (4.12)$$

In this equation, the top case is for $\gamma_a < \gamma_c$, the bottom case is for $\gamma_c < \gamma_a$. With this expression for B, N_e is still given by Equation 4.6. We then solve Equation 4.7 for Compton-Y, which allows us to determine B, N_e, and the synchrotron frequencies ν_i, ν_a, ν_c. We consider a solution with a 2nd IC scattering to be valid if $Y^2 < 1000$ and the 3rd IC scattering is KN suppressed. We do not include a 3rd IC scattering since for a $\nu_{\rm syn} \sim 100$ eV - 1 keV and $\gamma_e \sim 10 - 100$, it is likely KN suppressed.

4.4.4 Results for Synchrotron Parameter Space Search

In Figure 4.1, we show the parameter space of allowed solutions that satisfy the constraints discussed in Section 4.4.3 for the 4 flares we consider for our parameter space search (Section 4.3.3). We were only able to find valid solutions for the flares with a single power-law spectrum. None of the parameter

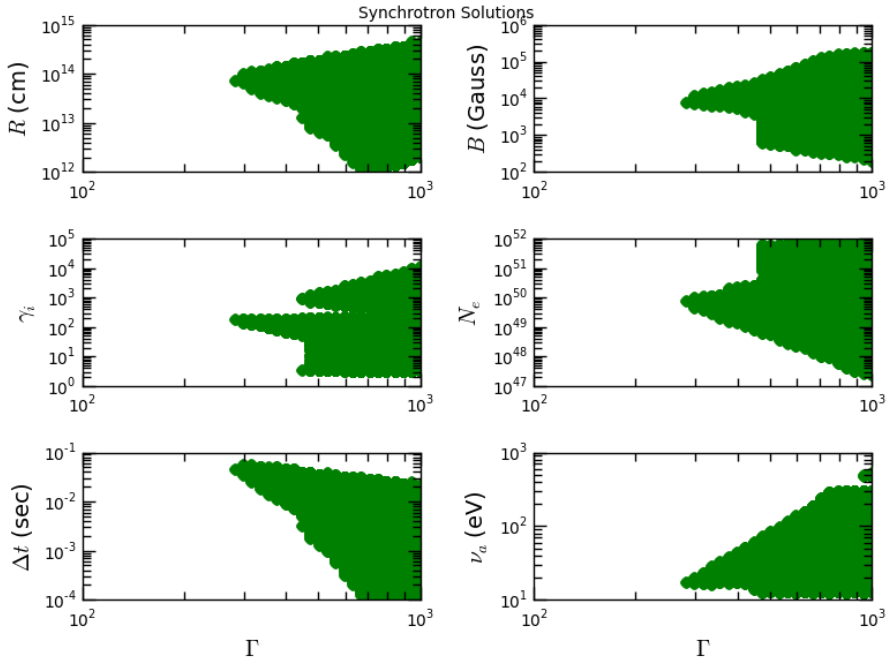

Figure 4.1: Parameter space of acceptable solutions for synchrotron for the X-ray flares in our sample.

space for the flares with a Band function spectrum produces $\nu_a > 2$ eV. This is due to the fact that to fit the X-ray observations, $f_{\nu_p} = f_{10\mathrm{keV}}(E_{\mathrm{pk}}/10\ \mathrm{keV})^{-\beta}$, with $E_{\mathrm{pk}} \sim 1$ keV for the Band function flares and E_{pk} is a free parameter between 2 eV and 0.3 keV for the flares with a single power-law spectrum. The larger f_{ν_p} for the single power-law flares requires more electrons, making self-absorption stronger. In addition, the parameter space of valid synchrotron solutions for the single power-law spectrum flares is unattractive since the allowed variability time is $\sim 10^{-4} - 10^{-1}$ sec, much smaller than the typical 10-100 sec observed flare variability time. These findings make synchrotron an unattractive mechanism to explain the X-ray flares observations for our

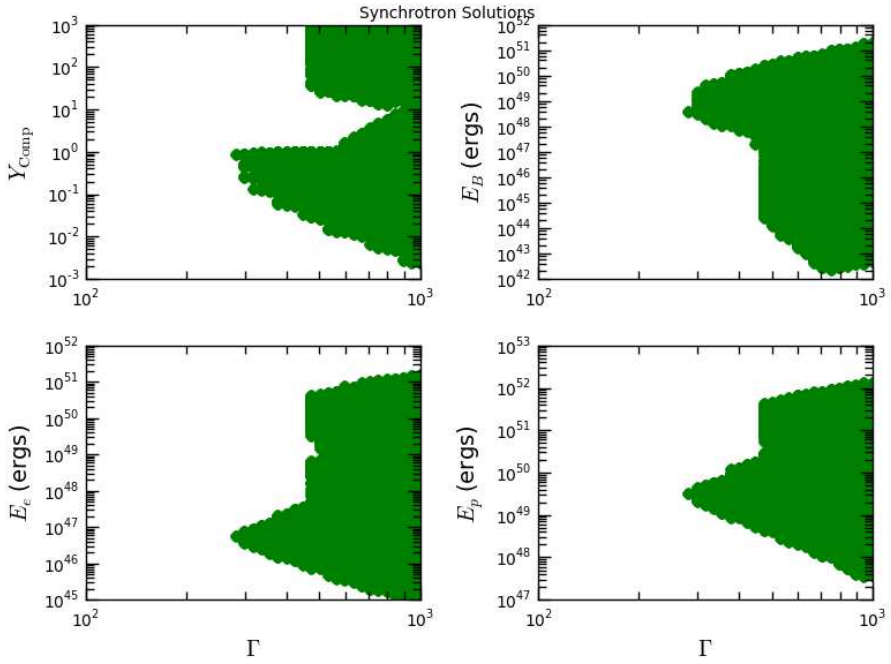

Figure 4.2: Allowed values for Compton-Y, E_B, E_e, and E_p for the synchrotron parameter space search.

sample.

In Figure 4.2, we show the values of Compton-Y and the energy in electrons (E_e), magnetic field (E_B), and cold protons (E_p) for the solutions that satisfy the synchrotron constraints. The energies were calculated with the following expressions:

$$E_e = N_e m_e c^2 \gamma_p \Gamma \tag{4.13}$$

$$E_B = \frac{1}{6} B^2 R^3 \tag{4.14}$$

$$E_p = N_e m_e c^2 \Gamma, \tag{4.15}$$

where γ_p is the electron Lorentz factor at the peak of the f_ν synchrotron

spectrum.

4.5 SSC Parameter Space Search

In this section, we discuss our strategy for searching the 5D SSC parameter space to determine if SSC can explain the observations of the X-ray flares in our sample.

4.5.1 Methodology for SSC Parameter Space Search

The 5 parameters that describe a SSC source are also Γ, R, B, N_e, γ_i. For the SSC parameter space search, we first calculate the seed synchrotron photon field with the synchrotron methodology described in Section 4.4. Thus, we continue to take Γ, Δt, γ_i, γ_a, γ_c as free parameters. As with synchrotron, we also consider multiple scatterings for SSC until the IC emission is KN suppressed. In addition to including the 1st scattering and the 2nd scattering, we also consider a 3rd IC scattering for SSC; to include it, we add a Y^3 term to γ_c:

$$\gamma_c = \frac{6\pi m_e c}{\sigma_T} t_{\rm dyn}^{-1} \Gamma^{-1} B^{-2} (1+z) \times \begin{cases} (1+Y+Y^2+Y^3)^{-1} & \gamma_a < \gamma_c \\ (\chi(\gamma_c/\gamma_a)+Y+Y^2+Y^3)^{-1} & \gamma_c < \gamma_a. \end{cases} \tag{4.16}$$

Thus, B in terms of Compton-Y is given by

$$B = \sqrt{\frac{6\pi m_e c}{\sigma_T}} (t_{\rm dyn})^{-1/2} \Gamma^{-1/2} (1+z)^{1/2} \gamma_c^{-1/2} \times \begin{cases} (1+Y+Y^2+Y^3)^{-1/2} \\ (\chi(\gamma_c/\gamma_a)+Y+Y^2+Y^3)^{-1/2} \end{cases} \tag{4.17}$$

In this equation, the top case is for $\gamma_a < \gamma_c$, the bottom case is for $\gamma_c < \gamma_a$. As before, with this expression for B, N_e is still given by Equation 4.6. We then solve Equation 4.7 for Compton-Y, which allows us to determine B, N_e, and the synchrotron frequencies ν_i, ν_a, ν_c. We then use the electron Lorentz factors γ_i, γ_a, γ_c and ν_i, ν_a, ν_c to calculate the IC scattered frequencies. We did not include a 4th IC scattering since it is likely KN suppressed.

For SSC, we require that $\nu_a^{\rm IC}$ (IC scattered self absorption frequency) is between the optical and X-ray band. The break frequencies for the SSC spectrum are given in Table 4.2. In addition, as for synchrotron, we require the SSC spectrum to be consistent with the X-ray and optical observations. The peak specific flux of the SSC spectrum ($f_{\nu_p}^{\rm IC}$) is given by

$$f_{\nu_p}^{\rm IC} = 3\tau_e f_{\nu_p}, \tag{4.18}$$

where $\tau_e = (\sigma_T N_e)/(4\pi R^2)$ and f_{ν_p} is the peak synchrotron flux (Equation 4.4). The major differences between the synchrotron and SSC spectrum are 1. The number of break frequencies: If $\min(\gamma_i, \gamma_a, \gamma_c) \neq \gamma_a$, there are only 2 break frequencies in the SSC spectrum. 2. For $\max(\gamma_i, \gamma_a, \gamma_c) \neq \gamma_a$, $f_\nu \propto \nu^1$ for $\nu < \nu_a^{\rm IC}$ and when $\max(\gamma_i, \gamma_a, \gamma_c) = \gamma_a$, $f_\nu \propto \nu^1$ for $\nu < \nu_{a,1}^{\rm IC}$. In addition, above $f_{\nu_p}^{\rm IC}$, the SSC spectrum is slightly curved since the SSC spectrum is approximately the synchrotron spectrum multiplied by a logarithmic ($\ln(\nu)$) term (Panaitescu & Mészáros, 2000; Sari & Esin, 2001; Gao et al., 2013). However, we neglect this slight curvature and approximate the SSC spectrum above $f_{\nu_p}^{\rm IC}$ as power-law segments. Thus, if $\max(\gamma_i, \gamma_a, \gamma_c) \neq \gamma_a$, above the peak energy, the SSC

spectrum is either $f_\nu \propto \nu^{-p/2}$ (satisfied when $\max(\nu_a^{\rm IC}, \nu_i^{\rm IC}, \nu_c^{\rm IC}) < \nu$), $f_\nu \propto \nu^{-(p-1)/2}$ (satisfied when $\max(\nu_a^{\rm IC}, \nu_i^{\rm IC}) < \nu < \nu_c^{\rm IC}$), or $f_\nu \propto \nu^{-0.5}$ (satisfied when $\max(\nu_a^{\rm IC}, \nu_c^{\rm IC}) < \nu < \nu_i^{\rm IC}$) (Gao et al., 2013). When $\max(\gamma_i, \gamma_a, \gamma_c) = \gamma_a$, $f_\nu \propto \nu^{-p/2}$ for $\nu > \nu_{a,2}^{\rm IC}$, $f_\nu \propto \nu^{-(p-1)/2}$ for $\nu_{a,1}^{\rm IC} < \nu < \nu_{a,2}^{\rm IC}$ and $\gamma_i < \gamma_c < \gamma_a$, and $f_\nu \propto \nu^{-1/2}$ for $\nu_{a,1}^{\rm IC} < \nu < \nu_{a,2}^{\rm IC}$ and $\gamma_c < \gamma_i < \gamma_a$ (Panaitescu & Mészáros, 2000).

4.5.2 Constraints for Valid SSC Solutions

To fit the observed spectral index, as with the synchrotron parameter space search, we continue to consider both the $f_\nu \propto \nu^{-p/2}$ and $f_\nu \propto \nu^{-(p-1)/2}$ segments for GRBs 060904B, 061121, 081008 and the $f_\nu \propto \nu^{-0.5}$ segments for GRB 080310 with both $p = 2.8$ and $p = 3.8$. To match the observed X-ray flux, for the flares with a Band function, we require $f_{\nu_p}^{\rm IC}$ to match $f_{E_{\rm pk}} = f_{10{\rm keV}}(10\ {\rm keV}/E_{\rm pk})^{-\beta_B}$ within a factor of 2 and the SSC break frequency at $f_{\nu_p}^{\rm IC}$ to match $E_{\rm pk}$ within a factor of 2. For the flares with a single power-law spectrum, we extrapolate $f_{\nu_p}^{\rm IC}$ to 0.3 keV and require it to match $f_{0.3{\rm keV}} = (0.3\ {\rm kev}/10\ {\rm keV})^{-\beta}$ within a factor of 2. For the solutions with $\nu_a^{\rm IC}$ between the optical and X-ray band, we also require that both the SSC and the synchrotron flux at 2 eV are below the observed optical flux $f_{2{\rm eV,cor}}$. To find the SSC flux below the peak energy, we use the SSC spectrum below the peak energy: for $\max(\gamma_i, \gamma_a, \gamma_c) \neq \gamma_a$, $f_\nu \propto \nu^{1/3}$ for $\nu_a^{\rm IC} < \nu < \min(\nu_i^{\rm IC}, \nu_c^{\rm IC})$ and $f_\nu \propto \nu^1$ for $\nu < \nu_a^{\rm IC}$; for $\max(\gamma_i, \gamma_a, \gamma_c) = \gamma_a$ $f_\nu \propto \nu^1$ for $\nu < \nu_{a,1}^{\rm IC}$. The synchrotron photon field usually peaks below the optical band. Thus, we use the synchrotron

segments above f_{ν_p} to extrapolate f_{ν_p} to 2 eV: $f_\nu \propto \nu^{-p/2}$, $f_\nu \propto \nu^{-(p-1)/2}$, and $f_\nu \propto \nu^{-0.5}$.

Lastly, as with the synchrotron parameter space search, we also require that the IC emission from multiple IC scatterings not violate energy constraints. For SSC, the 1st IC produces the $\sim 10^{51} - 10^{52}$ ergs of energy observed for X-ray flares. If the 2nd IC scattering is not KN suppressed, for a valid solution, we require $Y^2 < 1000$ and that the 3rd IC scattering is KN suppressed. If the 3rd IC scattering is not suppressed, we require $Y^3 < 1000$ for a valid synchrotron solution; we take the 4th IC scattering to be KN suppressed.

4.5.3 Results for SSC Parameter Space Search

For the 4 bursts we consider for our X-ray flare parameter space search (Section 4.3.3), we found a very narrow parameter space of solutions for GRB 080310, which has an observed X-ray spectrum $f_\nu \propto \nu^{-1/2}$, and we found no solutions for the other three bursts. The basic problem with SSC is that the seed synchrotron field overproduces the observed flux at 2 eV. From Table 4.1, the X-ray flux at 0.3keV-1keV is ~ 100 times larger than the observed flux at 2 eV. Thus, in order to match the observed X-ray flare peak flux with $f^{\rm IC}_{\nu_p} = 3\tau_e f_{\nu_p}$, the seed synchrotron flux will be larger than the observed optical flux by a factor $\sim 100/(3\tau_e)$. This large synchrotron flux overproduces the observed optical flux by a large factor. Thus, we determine that SSC is not a good mechanism to explain the X-ray flare observations. Lastly, we note that Troja et al. (2015) performed a similar parameter space search for SSC and

they also determined that SSC cannot explain the X-ray flare observations.

4.6 Synchrotron from a Poynting Jet Parameter Space Search

In this section, we consider synchrotron from a Poynting jet, where the energy of the jet is carried primarily by magnetic fields. In a Poynting model, magnetic reconnection is taken to dissipate the magnetic field and the particles are accelerated in regions referred to as Particle Acceleration Sites (PASs), associated with X-points. In these X-points, the magnetic field lines reconnect and the electric field generated by reconnection is taken to accelerate the electrons. These electrons then radiate synchrotron emission while inside the PASs. Although the magnetic field in a PAS is strong, the electrons will not cool significantly as long as the rate at which the electrons are radiating energy is less than the rate at which the electrons gain energy through magnetic reconnection. The time spent by electrons in PASs is unknown. Once an electron leaves a PAS, it will cool by radiating synchrotron in the strong magnetic field present in the jet. Multiple PASs are expected to be produced in the jet by magnetic reconnection and the electrons can be re-accelerated by entering another PAS.

A predictive model for radiation from a Poynting jet has not been developed due to the poorly understood details of magnetic reconnection and particle acceleration in magnetic reconnection regions. Recently, Kumar & Crumley (2015) used global properties of the magnetic field and conservation

laws to understand the broad properties of radiation from a Poynting jet. In this section, we apply the model presented in Kumar & Crumley (2015) to X-ray flares.

4.6.1 Methodology for Poynting Jet Parameter Space Search

In a Poynting jet, the jet luminosity can be used to determine the strength of the magnetic field in the jet, defined as B_0 (B_0 is measured in the jet-comoving frame):

$$L = (B_0)^2 \Gamma^2 R^2 c \rightarrow B_0 = \frac{\sqrt{L/c}}{R\Gamma}. \tag{4.19}$$

In the PASs, although some of the magnetic field B_0 is dissipated by magnetic reconnection to produce an electric field, the magnetic field in PAS is still of order B_0 (Kumar & Crumley, 2015). Thus, by determining B_0, we determine the magnetic field inside PASs. To determine B_0, we take $L = 5L_X$, i.e. we assume $\sim$ 20% efficiency in the conversion of jet energy to X-ray radiation (values of L_X in Table 4.1) and for R we use Equation 4.1. With the value for B_0, we can now perform a parameter space search for synchrotron emission inside PASs. As in Section 4.4, we continue to take Γ, Δt, γ_i, γ_c, and γ_a, as free parameters. We neglect the IC cooling of electrons for the Poynting model since the strong magnetic field in the Poynting jet leads to the synchrotron power dominating over the IC power. To determine N_e, we continue to use Equation 4.6, with B_0 entered for B. We now have all the parameters that describe a synchrotron source (Γ, R, B, γ_i, N_e), which allows us to use Equation 4.5 to calculate ν_a and determine if it is between the optical and X-ray

band. One last detail we note is the following: since electrons are expected to remain hot, and not cool while inside PAS, we do not consider the cases with strong synchrotron self-absorption, i.e. $\gamma_c < \gamma_a$. Thus, for the Poynting model parameter space search, we only consider the regimes $\gamma_a < \gamma_i < \gamma_c$, $\gamma_i < \gamma_a < \gamma_c$, and $\gamma_a < \gamma_c < \gamma_i$.

4.6.2 Constraints for Valid Poynting Solutions

As we described in Section 4.4.3, for a valid solution, in addition to producing a ν_a between the optical and X-ray band, we also require that solutions match the observed spectral index, the observed X-ray flux, and produce an optical flux below the observed optical flux. Furthermore, for a valid Poynting solution, we also require that the synchrotron emission from inside PASs is larger than the synchrotron emission from outside PASs. The ratio of the synchrotron flux from inside PASs to the synchrotron flux from outside PASs, at the peak of the f_ν spectrum, is given by (Kumar & Crumley, 2015)

$$\mathcal{R}_p = \frac{\xi t'_{\rm dyn}}{t'_{\rm cool}(\gamma_p)}. \tag{4.20}$$

In this equation, $\xi t'_{\rm dyn}$ is the time electrons spend inside PASs (in the jet-comoving frame) and $t'_{\rm cool}(\gamma_p) = (6\pi m_e c)/(\sigma_T B_0^2 \gamma_p)$ is the synchrotron cooling time (in the jet-comoving frame) for electrons radiating outside PASs and $\gamma_p = \min(\gamma_i, \gamma_c)$. For the timescale electrons spend inside PAS, ξ is a free parameter, which we take to be in the range $10^{-3} < \xi < 1$ and $t'_{\rm dyn} = R/(2c\Gamma)$. Thus, a smaller ξ leads to electrons spending less time in PASs, which leads to

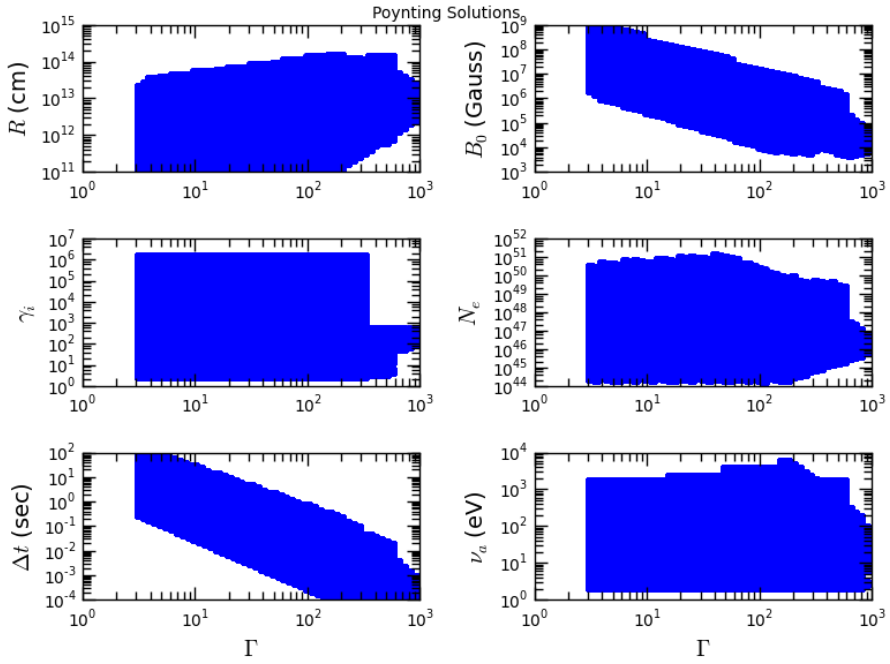

Figure 4.3: Parameter space of acceptable solutions for synchrotron radiation from a Poynting jet for the X-ray flares in our sample.

a smaller value for $\mathcal{R}_p$. In order for the emission from inside PAS to dominate over the emission from outside PAS, we enforce the condition $\mathcal{R}_p > 10$ for acceptable solutions for the Poynting model. Lastly, we note that we enforce the conditions $E_B > E_e$ and $E_B > E_p$ so that the energy in the magnetic field dominates over the energy in electrons and protons.

4.6.3 Results for Poynting Jet Parameter Space Search

In Figure 4.3 and Figure 4.4, we show the parameter space that satisfies the constraints discussed in Section 4.6.2 for the 4 flares we consider for our parameter space search (Section 4.3.3). We were able to find solutions

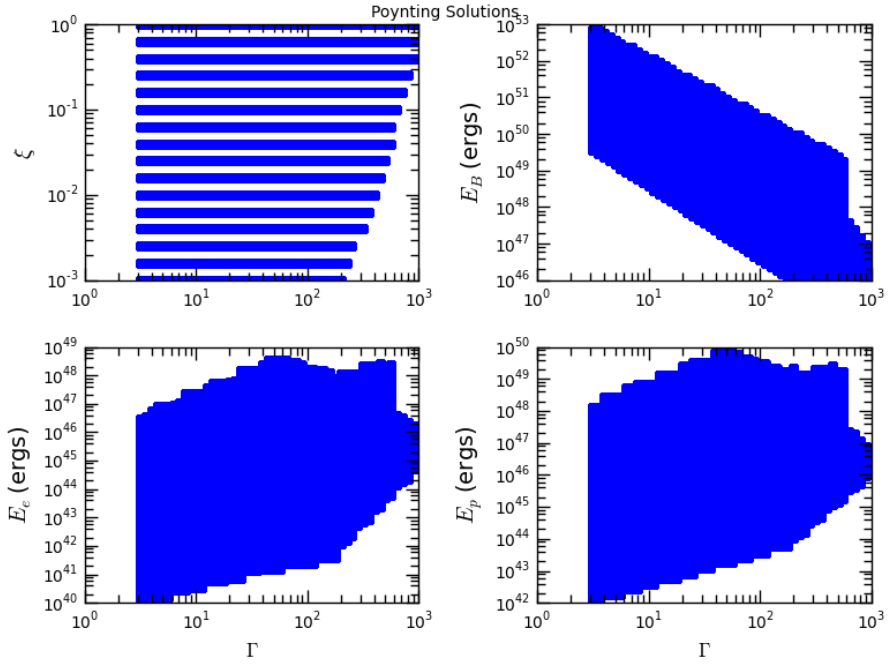

Figure 4.4: Allowed values for ξ, E_B, E_e, and E_p for our synchrotron emission from a Poynting jet parameter space search. In the top-left panel, the blank spaces in between the horizontal lines are due to our grid size of 5 points per log decade in ξ.

for both the flares that have a Band function spectrum and a single power-law spectrum. The parameter space of the allowed solutions is very broad. In particular, there are solutions for the flare variability time spanning from 10^{-4} sec to 10^{2} sec, with $\sim$ 10 - 100 seconds being a typical time for flares. One small drawback of the Poynting model is that studies on particle acceleration in magnetic reconnection regions find $p < 2$, whereas we need either $p = 2.8$ or $p = 3.8$ to fit the observed X-ray flare spectrum. Otherwise, synchrotron radiation from a Poynting jet is a good candidate to explain the radiation

mechanism of the flares in our sample.

4.7 Parameter Space Search for the Photospheric Process

Another mechanism that has been studied in detail to explain the prompt emission is the photospheric process (Thompson, 1994b; Ghisellini & Celotti, 1999; Mészáros & Rees, 2000; Mészáros et al., 2002; Rees & Mészáros, 2005; Pe'er et al., 2006; Thompson et al., 2007; Pe'er, 2008; Giannios, 2008; Beloborodov, 2010; Lazzati & Begelman, 2010; Beloborodov, 2011; Toma et al., 2011; Pe'er & Ryde, 2011; Mizuta et al., 2011; Lundman et al., 2013; Lazzati et al., 2013; Ruffini et al., 2013; Bégué et al., 2013; Deng & Zhang, 2014; Ito et al., 2014; Bégué & Iyyani, 2014). The basic picture of the photospheric process is as follows. Photons are assumed to be produced below the photosphere. At an optical depth $\tau \sim$ few, a dissipation event is assumed to occur, which accelerates electrons to mildly relativistic or relativistic speeds [3]. In the photospheric model, the average energy of the photons is taken to be much smaller than the average energy of the electrons. Thus, while the outflow is still optically thick, the photons and electrons undergo multiple scatterings (Comptonization) and the photons gain energy from the electrons until their energy reaches the average electron energy. Although not a necessary condi-

[3]The dissipation events discussed in the literature for the photospheric process are magnetic reconnection (Thompson, 1994b; Giannios & Spruit, 2005; Giannios, 2006, 2012) and internal shocks (Daigne & Mochkovitch, 2002; Lazzati & Begelman, 2010; Toma et al., 2011; Lazzati et al., 2013).

tion for the Comptonization of photons, works on the photospheric process usually consider the photons to initially have a Blackbody (BB) spectrum, with the BB peak energy taken to match the peak energy of the Band function. Thus, the goal of the photospheric model is to broaden the Blackbody spectrum so that it matches the Band function. The Comptonization of BB photons by hot electrons is predicted to produce a power-law spectrum above the BB peak because only a fraction f of the photons get scattered once by a hot electron to higher energies, only a fraction f^2 of the photons get scattered twice by a hot electron to higher energies, and so on (Lazzati & Begelman, 2010; Ghisellini, 2013). Once the outflow reaches the photospheric radius, the medium becomes optically thin and the photons escape the outflow. The resulting observed spectrum is a peak determined by the BB temperature of photons and a power-law above the peak energy[4].

In this section, we perform Monte Carlo (MC) simulations of the photospheric process to determine if it can explain the X-ray flare observations. To perform the simulations, we use a code we developed to study the photospheric process for the prompt emission (Santana et al., 2015). In the next two subsections, we discuss the values we choose for the input parameters of our code and the simulation results (for a detailed discussion of the code, see Santana et al. 2015).

[4]One of the major difficulties of the photospheric model is reproducing the typically observed low-energy spectrum $f_\nu \propto \nu^0$. In this work, we ignore the low-energy spectrum issue and focus on the high-energy spectrum. For detailed discussions on the low-energy index of the photospheric process, see Vurm et al. 2013; Lundman et al. 2013; Deng & Zhang 2014.

4.7.1 Parameters Considered for MC Photospheric Simulations

An important quantity needed to simulate the photospheric process is the ratio of photons to electrons, since it determines the number of photons (N_γ) and the number of electrons (N_e) needed for a MC simulation (Lazzati & Begelman, 2010; Chhotray & Lazzati, 2015). In Santana et al. 2015, we showed that the photon to electron ratio is given by

$$\frac{N_\gamma}{N_e} = (3 \times 10^7) \left(\frac{\eta}{1-\eta}\right) \left(\frac{\Gamma}{30}\right) \left(\frac{E_{\rm pk}}{1\ {\rm keV}}\right)^{-1}, \tag{4.21}$$

where η is the efficiency in the conversion of kinetic energy of the jet to X-ray radiation and $E_{\rm pk}$ is the peak energy of the X-ray flare spectrum, in the observer frame. Taking an efficiency $\eta \sim 10\%$, the photon to electron ratio is $N_\gamma/N_e \sim 10^6$. Thus, we use $N_\gamma/N_e = 10^6$ for the photospheric simulations we present in this work.

4.7.1.1 Input Parameters for MC Simulations

Below, we define the input parameters for our code and the values we take for each parameter. In the discussion below and throughout this section, unprimed (primmed) quantities refer to quantities in the observer (jet-comoving) frame.

- Γ — The bulk Lorentz factor of the outflow. We consider $\Gamma = 30$, a typical value previous studies have found for the bulk Lorentz factor of X-ray flares (Jin et al., 2010; Yi et al., 2015).

- L — The isotropic equivalent kinetic luminosity of the outflow. We consider $L = 10^{51}$ ergs/sec.

- N_e — The number of electrons in a simulation. We consider $N_e = 10^2$ in this work. Previous works typically considered $N_e = 10^3$ (Lazzati & Begelman, 2010; Chhotray & Lazzati, 2015; Santana et al., 2015). However, if we consider $N_e = 10^3$ electrons, for the large photon to electron ratio we are considering, the simulations will be computational expensive (about 90 GB of RAM are needed). To determine if $N_e = 10^2$ electrons are enough for a MC photospheric simulation, we performed a few simulations with $N_e = 10^3$ and found the results to be identical to the $N_e = 10^2$ simulation results. Thus, we consider $N_e = 10^2$.

- Electron Distribution — We consider a Maxwell-Boltzmann (MB) distribution of electrons since in Santana et al. 2015 we found that this electron distribution broadens the photon spectrum the most. The input parameter is the electron temperature T'_e, with $k_B T'_e = m_e c^2(\gamma'_e - 1)$.

- $\tau_{\rm initial}$ — The optical depth corresponding to the location where the photons are initialized and the location where a dissipation event, which heats up the electrons, is taken to occur. We consider $\tau_{\rm initial} = 2$, 8, 16.

- N_γ — The number of photons in a simulation. Since we consider $N_e = 10^2$, to reach $N_\gamma/N_e = 10^6$, we consider $N_\gamma = 10^8$.

- T'_γ — The photons are initialized to have a Blackbody (BB) distribution with temperature T'_γ. We consider $k_B T'_\gamma = 1$ eV, 3 eV, 10 eV, 30 eV.

- $N_{\rm collect}$ — The number of photons collected for the output spectrum. We consider $N_{\rm collect} = N_\gamma/3$ for our simulations as in previous MC simulations (Lazzati & Begelman, 2010; Santana et al., 2015). By plotting the first $N_\gamma/3$ photons that escape the photosphere for an output spectrum, we are plotting a time-averaged spectrum.

4.7.1.2 Values considered for γ'_e

In the photospheric model, in order to avoid synchrotron cooling of electrons from the magnetic field that is expected to be present in the jet, the synchrotron emission is taken to be self-absorbed. The largest γ'_e that can be considered is found by setting the optical depth for synchrotron self-absorption equal to 1. For a MB distribution of electrons, the synchrotron self-absorption optical depth $\tau_{\rm syn}^{\rm MB}$ is given by (Rybicki & Lightman, 1979; Lazzati & Begelman, 2010)

$$\tau_{\rm syn}^{\rm MB} = \frac{10^{10}}{(\gamma'_e)^5 \epsilon_B^{1/2} (E'_\gamma/10\ {\rm eV})^2}. \tag{4.22}$$

In this equation, $\epsilon_B = U_B/U_{\rm rad}$, where U_B ($U_{\rm rad}$) is the energy density in the magnetic field (radiation). Setting $\tau_{\rm syn}^{\rm MB} = 1$ and $\epsilon_B \sim 0.1$ (magnetic field subdominant to radiation), for the 4 photon temperatures we consider, $E'_\gamma \sim$ 1 eV, 3 eV, 10 eV, 30 eV, the upper limit we find is $\gamma'_e \sim$ 320, 200, 130, 80, respectively. We consider the largest value allowed for γ'_e for each photon temperature we consider.

Lastly, we note that our code includes adiabatic cooling of photons and electrons.

4.7.2 Results for MC Photospheric Simulations

In Figure 4.5, we show the output spectrum for our MC photospheric simulations. In each panel, a power-law has not developed above the peak energy for the $\tau_{\rm initial} = 2$ simulations. However, for $\tau_{\rm initial} = 8$, 16, there is a clear power-law above the peak-energy for ~ 3 decades in energy, with a peak energy in the range 0.1 - 1 keV [5]. The slope of the high-energy spectrum for the $\tau_{\rm initial} = 8$, 16 simulations are: $f_\nu \propto \nu^{-0.55}$ (top-left panel), $f_\nu \propto \nu^{-0.80}$ (top-right panel), $f_\nu \propto \nu^{-1.06}$ (bottom-left panel), and $f_\nu \propto \nu^{-1.44}$ (bottom-right panel). Thus, the photospheric process can explain the wide range of high-energy spectral indicies observed for the flares in our sample. X-ray flares with a harder high-energy spectrum need to have lower photon temperatures, which allow for the BB spectrum to be broadened more. The increase in broadening for lower values of $k_B T'_\gamma$ is due to two effects: 1. lower energy photons cool the electrons slower, allowing for more photons to be up-scattered to higher energies. 2. weaker synchrotron self-absorption at lower photon energies allows for more energetic electrons, which have more energy available to transfer to the photons. The peak energy for our simulations, $\sim$ 0.1-1 keV, can explain the flares with a Band function spectrum and the flares with a single power-law spectrum. In addition, since the bulk Lorentz factor controls the Doppler boosting of the photon spectrum to the observer frame, the bulk Lorentz factor can be adjusted to obtain a lower or higher peak energy. Lastly, we note

[5] Due to the adiabatic cooling of photons, the $\tau_{\rm initial} = 8$, 16 simulations have a lower peak energy than the $\tau_{\rm initial} = 2$ simulations.

that the low-energy spectrum for our simulations is in the range $f_\nu \propto \nu^{1.6}$ - $f_\nu \propto \nu^{1.9}$. Thus, the photospheric emission in the optical band will be well below the observed optical flux.

4.8 Discussion And Conclusions

In this work, we studied X-ray flares with coincident optical observations to constrain the X-ray flare radiation mechanism. For 8 flares, we determined that the X-ray flare emission, extrapolated to the optical band with a optically-thin $f_\nu \propto \nu^{1/3}$ spectrum, over-produces the observed optical flux by a factor larger than 2. Thus, in order to not over-produce the observed optical flux, the X-ray flare observations require a self-absorption break between the optical and X-ray band. We then performed a parameter space search for synchrotron, SSC, synchrotron from a Poynting jet, and photospheric emission to determine which mechanism can explain the flare observations. Synchrotron and SSC have problems: the synchrotron solutions require a variability time much shorter than the observed flare variability time and the seed synchrotron flux for SSC over-produces the observed optical flux by a large factor. Synchrotron from a Poynting jet and the Photospheric process both have a wide parameter space that explains the flare observations. Thus, both a Poynting jet and a baryonic jet can explain X-ray flares, with the photospheric process being the best candidate in a baryonic jet.

GRB (Band f_ν)	$t_{\rm pk}$ sec	$f_{\rm 10keV}$ mJy	z	$d_{\rm L28}$	$L_{X,50}$	$E_{\rm pk}$ keV	$\beta_{\rm B}$	$f_{\rm 2eV,cor}$ mJy	$\frac{f_{\rm 2eV,pred}}{f_{\rm 2eV,cor}}$
060124	694	2	2.296	5.8	16.9	(1.3 ± 0.2)	1.2 ± 0.1 [1]	0.9 [8][9]	3.0
060904B	180	2	0.70	1.4	1.2	$3.7^{+0.2}_{-0.2}$	1.47 ± 0.10 [2]	0.2 [2][10]	3.0
061121	80	20	1.314	2.9	10.6	$0.95^{+0.05}_{-1}$	$1.4^{+0.1}_{-0.2}$ [1]	5.0 [11][12]	13.9
080928	200	5	1.692	4	10.0	$3.94^{+0.56}_{-0.62}$	$1.74^{+0.05}_{-0.08}$ [3]	0.2 [5]	11.4
GRB (SPL f_ν)	$t_{\rm pk}$ sec	$f_{\rm 10keV}$ mJy	z	$d_{\rm L28}$	$L_{X,50}$	β	$f_{\rm 2eV,cor}$ mJy	$\frac{f_{\rm 2eV,pred}}{f_{\rm 2eV,cor}}$	
051117A	926	0.05	0.73	1.4	0.07	$1.13^{+0.06}_{-0.06}$ [4]	0.07 [13]	6.8	
060714	200	0.2	2.711	7.1	5.1	0.50 ± 0.16 [5]	0.1 [5][9]	3.2	
080310	390	1	2.42	6.2	2.4	$0.476^{+0.019}_{-0.019}$ [6]	0.5 [14]	2.2	
081008	385	0.8	1.9685	4.8	1.2	$1.51^{+0.13}_{-0.12}$ [7]	7.0 [7]	4.3	

Table 4.1: Properties of the 8 X-ray flares for which we determined that ν_a must be between the optical and the X-ray band. The top [bottom] part of this table shows the properties of the four [four] X-ray flares whose spectrum is better fit by a Band function [Single Power-Law (SPL)] spectrum. References for X-ray spectrum and optical data: [1] = Butler & Kocevski (2007a), [2] = Margutti et al. (2010), [3] = Rossi et al. (2011), [4] = Falcone et al. (2007), [5] = Krimm et al. (2007), [6] = Evans et al. (2010), [7] = Yuan et al. (2010), [8] = Romano et al. (2006), [9] = Kann et al. (2010), [10] = Klotz et al. (2008), [11] = Page et al. (2007), [12] = Kopač et al. (2013), [13] = Goad et al. (2007), [14] = Littlejohns et al. (2012).

Ordering	SSC break frequencies
$\gamma_a < \gamma_i < \gamma_c$	$\nu_a^{\rm IC} = 4\gamma_i^2\nu_a$, $\nu_i^{\rm IC} = 4\gamma_i^2\nu_i$, $\nu_c^{\rm IC} = 4\gamma_c^2\nu_c$
$\gamma_i < \gamma_a < \gamma_c$	$\nu_a^{\rm IC} = 4\gamma_i^2\nu_a$, $\nu_c^{\rm IC} = 4\gamma_c^2\nu_c$
$\gamma_a < \gamma_c < \gamma_i$	$\nu_a^{\rm IC} = 4\gamma_c^2\nu_a$, $\nu_c^{\rm IC} = 4\gamma_c^2\nu_c$, $\nu_i^{\rm IC} = 4\gamma_i^2\nu_i$
$\gamma_c < \gamma_a < \gamma_i$	$\nu_a^{\rm IC} = 4\gamma_c^2\nu_a$, $\nu_i^{\rm IC} = 4\gamma_i^2\nu_i$
$\gamma_i < \gamma_c < \gamma_a$	$\nu_{a,1}^{\rm IC} = 4\gamma_i^2\nu_a$, $\nu_{a,2}^{\rm IC} = 4\gamma_c^2\nu_a$
$\gamma_c < \gamma_i < \gamma_a$	$\nu_{a,1}^{\rm IC} = 4\gamma_c^2\nu_a$, $\nu_{a,2}^{\rm IC} = 4\gamma_i^2\nu_a$

Table 4.2: Break frequencies of SSC spectrum. When $\max(\gamma_i,\, \gamma_a,\, \gamma_c) = \gamma_a$, there are two break frequencies associated with ν_a, which we denote as $\nu_{a,1}^{\rm IC}$ and $\nu_{a,2}^{\rm IC}$ (Panaitescu & Mészáros, 2000).

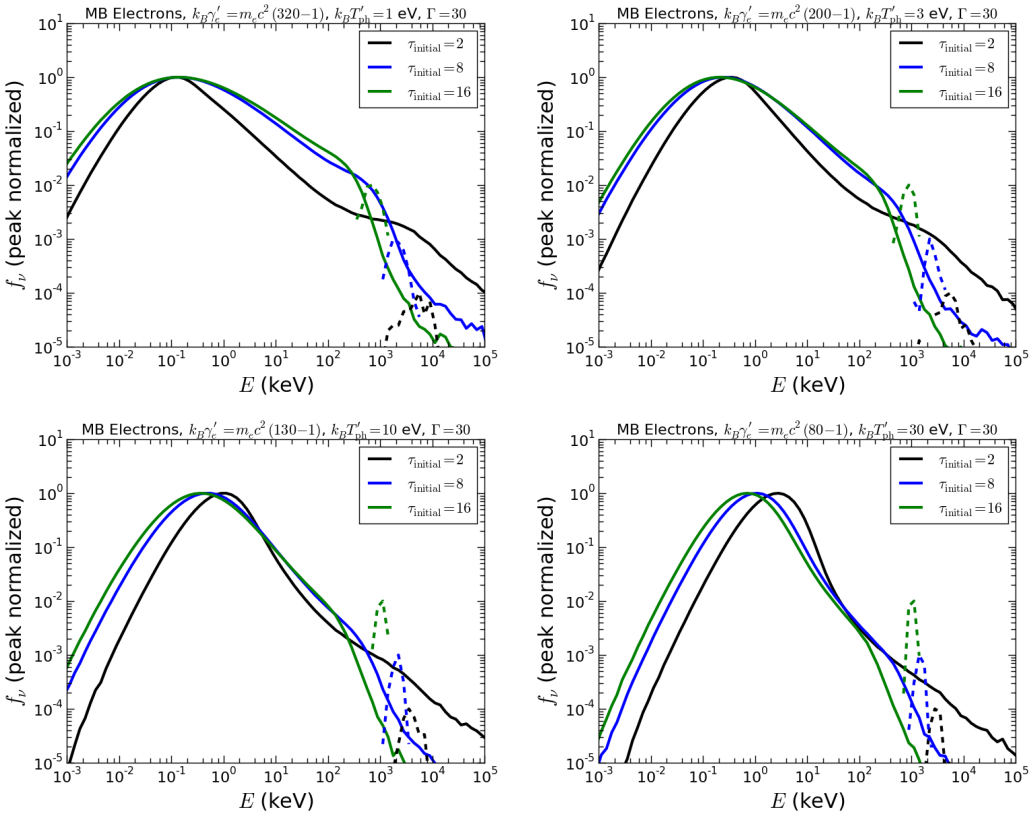

Figure 4.5: Output spectrum for MC photospheric simulations for Maxwell Boltzmann (MB) electrons, $\tau_{\rm initial} = 2$, 8, 16, and $\Gamma = 30$. The solid (dotted) lines correspond to the photon (electron) spectrum at the end of the simulations in the observer frame. The photon and electron temperatures for each panel are: $k_B T_\gamma' = 1$ eV, $k_B T_e' = (320-1) m_e c^2$ (top-left panel), $k_B T_\gamma' = 3$ eV, $k_B T_e' = (200-1) m_e c^2$ (top-right panel), $k_B T_\gamma' = 10$ eV, $k_B T_e' = (130-1) m_e c^2$ (bottom-left panel), $k_B T_\gamma' = 30$ eV, $k_B T_e' = (80-1) m_e c^2$ (bottom-right panel).

Appendices

Appendix A

ϵ_e And ϵ_B Values From The Literature

In this Appendix, we show a table of the ϵ_e and ϵ_B values we used to make the histograms in Figure 2.1. For the first GRBs with high quality afterglow data, different works (e.g. Wijers & Galama 1999; Chevalier & Li 1999, 2000; Li & Chevalier 2001; Harrison et al. 2001; Yost et al. 2003) have presented afterglow modeling studies on the same GRBs. In Table A.1, for these early afterglow studies, we show the results from Panaitescu & Kumar 2001a,b, 2002 since they have the largest afterglow modeling compilations. It is important to note that in some cases, different groups determined significantly different values for the afterglow parameters (e.g. GRB 970508 Wijers & Galama 1999; Chevalier & Li 2000; Frail et al. 2000; Panaitescu & Kumar 2002, GRB 000418 Berger et al. 2001; Panaitescu & Kumar 2002).

Table A.1: ϵ_e and ϵ_B Values From The Literature

GRB	ϵ_e	ϵ_B	Ref.
970508	0.62	0.10	[1]
980329	0.12	0.17	[2]
980519	0.25	$(3.5^{+32}_{-2.3}) \times 10^{-5}$	[1]
980703	0.14	4.6×10^{-4}	[3]
990123	0.59	$(7.4^{+23}_{-5.9}) \times 10^{-4}$	[1]
990510	> 0.3	6×10^{-3}	[4]
991208	0.32	2.1×10^{-2}	[1]

Table A.1: ϵ_e and ϵ_B Values From The Lit. (Continued)

GRB	ϵ_e	ϵ_B	Ref.
991216	0.4	2×10^{-2}	[4]
000301C	0.4	7×10^{-2}	[4]
000926	0.35	$(6.5^{+1.5}_{-1.1}) \times 10^{-2}$	[1]
010222	> 0.3	2×10^{-4}	[4]
011211	0.22	5.0×10^{-4}	[5]
020405	0.1	0.3	[6]
020813		4.0×10^{-4}	[5]
021004	0.21	2×10^{-4}	[7]
030226	0.11	2.5×10^{-4}	[5]
030329	0.16	0.10	[8]
050416A	$0.2 - 0.333$	$0.072 - 0.333$	[9]
050820A	$0.14^{+0.02}_{-0.01}$	$0.013^{+0.003}_{-0.001}$	[10]
050904	0.02	0.015	[11]
051022	$0.0681^{+0.3951}_{-0.0348}$	$(8.02^{+28.18}_{-7.17}) \times 10^{-3}$	[12]
051221A	$0.24 - 0.333$	$0.12 - 0.333$	[13]
060418	$0.06^{+0.01}_{-0.02}$	$0.15^{+0.14}_{-0.01}$	[10]
070125	$0.27^{+0.03}_{-0.01}$	$0.0277^{+0.0044}_{-0.0075}$	[14]
080129	0.4	5×10^{-2}	[15]
080319B	0.11 ± 0.01	0.33	[10]
080928	0.165	$(2.5^{+16}_{-2.4}) \times 10^{-4}$	[16]
090323	$0.070^{+0.005}_{-0.005}$	$0.0089^{+0.0007}_{-0.0018}$	[17]
090328	$0.11^{+0.06}_{-0.01}$	$0.0019^{+0.0004}_{-0.0008}$	[17]
090423	0.28	1.6×10^{-4}	[18]

Table A.1: ϵ_e and ϵ_B Values From The Lit. (Continued)

GRB	ϵ_e	ϵ_B	Ref.

Table A.1: In this table, we show all of the ϵ_e and ϵ_B values, determined in previous afterglow modelling studies, that we were able to find in the literature. These values are plotted in the histograms in Figure 2.1. In the column labeled Ref. we give the reference where we found each value of ϵ_e and ϵ_B. Reference Legend: [1] = Panaitescu & Kumar (2002), [2] = Yost et al. (2002), [3] = Panaitescu & Kumar (2001b), [4] = Panaitescu & Kumar (2001a), [5] = Panaitescu (2005), [6] = Berger et al. (2003a), [7] = Björnsson et al. (2004), [8] = Berger et al. (2003b), [9] = Soderberg et al. (2007), [10] = Cenko et al. (2010), [11] = Frail et al. (2006), [12] = Rol et al. (2007), [13] = Soderberg et al. (2006) [14] = Chandra et al. (2008), [15] = Gao (2009), [16] = Rossi et al. (2011), [17] = Cenko et al. (2011), [18] = Chandra et al. (2010)

Appendix B

MC Photospheric Code Algorithm

B.1 Conventions for Appendices

In the appendices below, we describe the details of the algorithm we adopted for our MC Photospheric code. The algorithms in Appendices B.2.1, B.2.2, B.3.1, B.3.2, and B.4 were adopted from the comprehensive IC/Compton scattering reference Pozdnyakov et al. (1983).

The conventions we describe here apply to all the Appendices below. All primed (un-primmed) quantities are in the jet-comoving (observer) frame. A quantity with a subscript i (initial) [f (final)] refers to the quantity before [after] the scattering event. All the random numbers we draw are denoted by ξ and they are uniform random numbers in the interval 0 to 1. When referring to a vector $\mathbf{A}$, the vector is put in boldface and the magnitude of the vector is denoted by $\|\mathbf{A}\|$. Lastly, $\hat{x}$, $\hat{y}$, $\hat{z}$ represent the unit vectors in Cartesian coordinates.

B.2 Initialization of Electrons

B.2.1 Drawing Random Electron Directions

The momentum of an electron is given by $\mathbf{p}'_e = \|\mathbf{p}'_e\|\mathrm{v}'_1\hat{x} + \|\mathbf{p}'_e\|\mathrm{v}'_2\hat{y} + \|\mathbf{p}'_e\|\mathrm{v}'_3\hat{z}$, where v'_1, v'_2, and v'_3 are the components of $\mathbf{p}'_e$ in the x, y, and z directions, respectively. To draw a random direction for an electron, draw two random numbers ξ_1, ξ_2 and use the expressions

$$\begin{aligned} \mathrm{v}'_3 &= 2\xi_1 - 1 \\ \mathrm{v}'_2 &= \sqrt{1-(\mathrm{v}'_3)^2}\sin(2\pi\xi_2) \\ \mathrm{v}'_1 &= \sqrt{1-(\mathrm{v}'_3)^2}\cos(2\pi\xi_2). \end{aligned}$$

B.2.2 Drawing Electron Energy from MB and PL Distributions

B.2.2.1 Maxwell Boltzmann Electrons

The dimensionless energy (n) and the dimensionless momentum (η) of an electron are given by $n = k_B T'_e/(m_e c^2)$ and $\eta = \|\mathbf{p}'_e\|/(m_e c)$, where $\|\mathbf{p}'_e\| = m_e c \beta'_e \gamma'_e$. From the expression for η, $\gamma'_e = \sqrt{\eta^2+1}$ and $\beta'_e = \eta/\gamma'_e$. Pozdnyakov et al. (1983) present two algorithms for drawing γ'_e for an electron, depending on whether $k_B T'_e$ is less than or larger than 150 keV.

If $k_B T'_e < 150$ keV, draw two random numbers ξ_1, ξ_2. First, calculate ξ' with the expression $\xi' = -(3/2)\ln(\xi_1)$. Then, test the acceptance-rejection condition $\xi_2^2 < 0.151(1+n\xi')^2\xi'(2+n\xi')\xi_1$. If it is satisfied, set $\eta = \sqrt{n\xi'(2+n\xi')}$, $\gamma'_e = \sqrt{\eta^2+1}$, and $\beta'_e = \eta/\gamma'_e$. Otherwise, continue to draw new ξ_1, ξ_2 until the acceptance-rejection condition is satisfied.

If $k_B T'_e \geq 150$ keV, draw four random numbers ξ_1, ξ_2, ξ_3, ξ_4. Compute the quantities $\eta' = -n \ln(\xi_1\xi_2\xi_3)$ and $\eta'' = -n \ln(\xi_1\xi_2\xi_3\xi_4)$ and test the acceptance-rejection condition $(\eta'')^2 - (\eta')^2 > 1$. If it is satisfied, set $\eta = \eta'$, $\gamma'_e = \sqrt{\eta^2 + 1}$, and $\beta'_e = \eta/\gamma'_e$. Otherwise, continue to draw new ξ_1, ξ_2, ξ_3, ξ_4 until the acceptance-rejection condition is satisfied.

B.2.2.2 Power-Law Distribution of Electrons

To drawn γ'_e for an electron following a PL distribution, draw one random number ξ_1 and calculate $E' = m_e c^2 \gamma'_e$ with the expression

$$E' = [\xi_1((E'_2)^{1-p} - (E'_1)^{1-p}) + (E'_1)^{1-p}]^{1/(1-p)}.$$

Then, we set $\gamma'_e = E'/(m_e c^2)$ and $\beta_e = \sqrt{1 - (\gamma'_e)^{-2}}$.

B.3 Initialization of Photons

B.3.1 Photon Directions

The momentum of a photon is given by $\mathbf{p}'_\gamma = (E'_\gamma/c)\Omega'_1\hat{x} + (E'_\gamma/c)\Omega'_2\hat{y} + (E'_\gamma/c)\Omega'_3\hat{z}$, where Ω'_1, Ω'_2, and Ω'_3 are the components of $\mathbf{p}'_\gamma$ in the x, y, and z directions, respectively. To draw a random direction for a photon, draw two random numbers ξ_1, ξ_2 and use the expressions (same algorithm as in Appendix B.2.1)

$$\begin{aligned}
\Omega'_3 &= 2\xi_1 - 1 \\
\Omega'_2 &= \sqrt{1 - (\Omega'_3)^2}\sin(2\pi\xi_2) \\
\Omega'_1 &= \sqrt{1 - (\Omega'_3)^2}\cos(2\pi\xi_2).
\end{aligned}$$

B.3.2 Photon Energies

B.3.2.1 BB Distribution

Draw four random numbers ξ_1, ξ_2, ξ_3, ξ_4. Then, determine α such that

$$\alpha = \begin{cases} 1 \text{ if} & 1.202\xi_1 < 1 \\ m \text{ if} & \sum_1^{m-1} j^{-3} \leq 1.202\xi_1 < \sum_1^{m} j^{-3}. \end{cases}$$

Then, set $E'_\gamma = -(k_B T'_\gamma/\alpha)\ \ln(\xi_2\xi_3\xi_4)$.

B.3.2.2 Power-Law Distribution

To draw a photon power-law distribution with $E'_{\gamma,1} < E < E'_{\gamma,2}$, draw one random number ξ_1 and set

$$E'_\gamma = [\xi_1((E'_{\gamma,2})^{1-p} - (E'_{\gamma,1})^{1-p}) + (E'_{\gamma,1})^{1-p}]^{1/(1-p)}.$$

The f_ν photon spectrum is given by $f_\nu \propto \nu^{1-p}$.

B.3.3 Photon Propagation

In this subappendix, we calculate the new position of a photon in the observer frame after it has traveled a distance s' in the jet-comoving frame. We denote the initial [final] position of the photon in the observer frame as $\mathbf{R_i} = R_{1,i}\hat{x} + R_{2,i}\hat{y} + R_{3,i}\hat{z}$ [$\mathbf{R_f} = R_{1,f}\hat{x} + R_{2,f}\hat{y} + R_{3,f}\hat{z}$]. The time traveled by the photon in the jet-comoving frame ($\Delta t'$) and the displacements of the photon in the jet-comoving frame in the x ($\Delta R'_1$), y ($\Delta R'_2$), and z ($\Delta R'_3$)

directions are given by

$$\begin{aligned}
\Delta t' &= s'(R)/c \\
\Delta R'_1 &= s'(R)\Omega'_{1,i} \\
\Delta R'_2 &= s'(R)\Omega'_{2,i} \\
\Delta R'_3 &= s'(R)\Omega'_{3,i},
\end{aligned}$$

where $\Omega'_{1,i}$ ($\Omega'_{2,i}$) [$\Omega'_{3,i}$] is the direction of the photon in the x (y) [z] direction before the scattering event.

From the bulk Lorentz factor of the jet, the speed of the jet divided by the speed of light is $\beta_j = \sqrt{1-\Gamma^{-2}}$. The components of β_j in the x ($\beta_{j,1}$), y ($\beta_{j,2}$), and z ($\beta_{j,3}$) directions are given by

$$\begin{aligned}
\beta_{j,1} &= \beta_j \cos\phi \sin\theta \\
\beta_{j,2} &= \beta_j \sin\phi \sin\theta \\
\beta_{j,3} &= \beta_j \cos\theta.
\end{aligned}$$

The angles θ and ϕ, corresponding to the photon position in spherical coordinates, can be found with the expressions $\cos\theta = R_{3,i}/\sqrt{(R_{1,i})^2 + (R_{2,i})^2 + (R_{3,i})^2}$ and $\tan\phi = R_{2,i}/R_{1,i}$. With these results, we can Lorentz transform the displacements from the jet comoving frame to the observe frame with the expres-

sions

$$\begin{aligned}
\Delta R_1 &= \Gamma\beta_{j,1}c\Delta t' + \left[1 + (\Gamma-1)\frac{\beta_{j,1}^2}{\beta_j^2}\right]\Delta R_1' + \\
&\quad \left[(\Gamma-1)\frac{\beta_{j,1}\beta_{j,2}}{\beta_j^2}\right]\Delta R_2' + \left[(\Gamma-1)\frac{\beta_{j,1}\beta_{j,3}}{\beta_j^2}\right]\Delta R_3' \\
\Delta R_2 &= \Gamma\beta_{j,2}c\Delta t' + \left[(\Gamma-1)\frac{\beta_{j,2}\beta_{j,1}}{\beta_j^2}\right]\Delta R_1' + \\
&\quad \left[1 + (\Gamma-1)\frac{\beta_{j,2}^2}{\beta_j^2}\right]\Delta R_2' + \left[(\Gamma-1)\frac{\beta_{j,2}\beta_{j,3}}{\beta_j^2}\right]\Delta R_3' \\
\Delta R_3 &= \Gamma\beta_{j,3}c\Delta t' + \left[(\Gamma-1)\frac{\beta_{j,3}\beta_{j,1}}{\beta_j^2}\right]\Delta R_1' + \\
&\quad \left[(\Gamma-1)\frac{\beta_{j,3}\beta_{j,2}}{\beta_j^2}\right]\Delta R_2' + \left[1 + (\Gamma-1)\frac{\beta_{j,3}^2}{\beta_j^2}\right]\Delta R_3'. \\
\Delta t &= \Gamma\Delta t' + \Gamma\beta_{j,1}(\Delta R_1'/c) + \\
&\quad \Gamma\beta_{j,2}(\Delta R_2'/c) + \Gamma\beta_{j,3}(\Delta R_3'/c).
\end{aligned}$$

In the above equation, Δt is the time it took the photon to travel a distance s' in the observer frame. The new position of the photon and the new distance of the photon from the central engine can be found with the equations

$$\begin{aligned}
R_{1,f} &= R_{1,i} + \Delta R_1 \\
R_{2,f} &= R_{2,i} + \Delta R_2 \\
R_{3,f} &= R_{3,i} + \Delta R_3 \\
R &= \sqrt{(R_{1,f})^2 + (R_{2,f})^2 + (R_{3,f})^2}.
\end{aligned}$$

B.4 Electron Photon Scattering Interaction

In this Appendix, we describe the algorithm from Chapter 9 of Pozdnyakov et al. (1983) for calculating the final energy ($E'_{\gamma,f}$) and direction of a photon ($\Omega'_{1,f}, \Omega'_{2,f}, \Omega'_{3,f}$) after a scattering event. The angle between the electron direction and photon direction before the scattering event is given by

$$\mu'_i = \mathrm{v}'_{1,i}\Omega'_{1,i} + \mathrm{v}'_{2,i}\Omega'_{2,i} + \mathrm{v}'_{3,i}\Omega'_{3,i}.$$

With the angle μ'_i, we can compute the dimensionless photon energy in the electron rest-frame, denoted as x'_i, with the expression

$$x'_i = 2\gamma'_{e,i}(E'_{\gamma,i}/m_e c^2)(1 - \mu'_i\beta'_{e,i}).$$

With x'_i, we can compute the cross-section for this interaction, $\sigma(x'_i) = 2\pi r_e^2 \hat{\sigma}(x'_i)$, where $r_e = e^2/(m_e c^2)$ is the Classical electron radius, e is the electron charge, and $\hat{\sigma}$ is calculated with the expression (Pozdnyakov et al., 1983)

$$\hat{\sigma}(x'_i) = \begin{cases} 1/3 + 0.141x'_i - 0.12(x'_i)^2 + \\ \quad (1 + 0.5x'_i)(1 + x'_i)^{-2}, & x'_i \leq 0.5; \\ [\ln(1 + x'_i) + 0.06](x'_i)^{-1}, & 0.5 \leq x'_i \leq 3.5; \\ [\ln(1 + x'_i) + 0.5 - (2 + 0.076x'_i)^{-1}](x'_i)^{-1}, & 3.5 \leq x'_i. \end{cases}$$

To test if the scattering event will occur, we draw a random number ξ_s. If $\xi_s < \sigma(x'_i)/\sigma_T$ is satisfied, the scattering event occurs.

If the scattering event is determined to occur, we perform an acceptance-rejection for the direction and energy of the photon after the scattering event. We first draw 3 random numbers ξ_1, ξ_2, ξ_3. The random numbers ξ_1, ξ_2 are

used to compute the angles

$$\begin{aligned}\mu'_f &= \frac{\beta'_{e,i} + 2\xi_1 - 1}{1 + \beta'_{e,i}(2\xi_1 - 1)} \\ \phi'_f &= 2\pi\xi_2.\end{aligned}$$

From μ'_f, ϕ'_f, we can compute the direction of the photon after the scattering event with the expressions

$$\begin{aligned}\Omega'_{1,f} &= \mu'_f \mathrm{v}'_{3,i} + \sqrt{1-(\mu'_f)^2}\rho^{-1}(\mathrm{v}'_{2,i}\cos\phi_f + \mathrm{v}'_{1,i}\mathrm{v}'_{3,i}\sin\phi'_f) \\ \Omega'_{2,f} &= \mu'_f \mathrm{v}'_{2,i} + \sqrt{1-(\mu'_f)^2}\rho^{-1}(-\mathrm{v}'_{1,i}\cos\phi'_f + \mathrm{v}'_{2,i}\mathrm{v}'_{3,i}\sin\phi'_f) \\ \Omega'_{3,f} &= \mu'_f \mathrm{v}'_{3,i} + \sqrt{1-(\mu'_f)^2}\rho\sin\phi'_f,\end{aligned}$$

where $\rho = \sqrt{(\mathrm{v}'_{1,i})^2 + (\mathrm{v}'_{2,i})^2}$. The next step is to compute the ratio of the dimensionless photon energy in the electron rest frame after scattering (x'_f), to x'_i, with the equation

$$\frac{x'_f}{x'_i} = \left[1 + \frac{E'_{\gamma,i}(1 - \mathbf{\Omega'_i}\cdot\mathbf{\Omega'_f})}{\gamma'_{e,i} m_e c^2 (1 - \mu_f \beta'_{e,i})}\right]^{-1},$$

where $\mathbf{\Omega'_i}\cdot\mathbf{\Omega'_f} = \Omega'_{1,i}\Omega'_{1,f} + \Omega'_{2,i}\Omega'_{2,f} + \Omega'_{3,i}\Omega'_{3,f}$ is the angle between the initial photon direction and the final photon direction. To determine if the final photon energy and direction is accepted, we use ξ_3 to test the acceptance-rejection condition

$$\begin{aligned}2\xi_3 &< \left(\frac{x'_f}{x'_i}\right)^2 \mathcal{X} \text{ , where} \\ \mathcal{X} &= \left(\frac{x'_f}{x'_i}\right)^{-1} + \frac{x'_f}{x'_i} + \frac{4}{x'_i}\left[1 - \left(\frac{x'_f}{x'_i}\right)^{-1}\right] + \frac{4}{(x'_i)^2}\left[1 - \left(\frac{x'_f}{x'_i}\right)^{-1}\right]^2.\end{aligned}$$

If the condition $2\xi_3 < (x'_f/x'_i)^2\mathcal{X}$ is satisfied, the final photon direction is accepted and the energy of the photon after scattering is found with the expression $E'_{\gamma,f} = (x'_f/x'_i)x'_i m_e c^2[2\gamma'_{e,i}(1-\mu'_f\beta'_{e,i})]^{-1}$. Otherwise, we continue to draw 3 new random numbers ξ_1, ξ_2, ξ_3 until the condition $2\xi_1 < (x'_f/x'_i)^2\mathcal{X}$ is satisfied.

B.5 Updating Electron Energy and Direction After Scattering

In addition to updating the energy and direction of the photon after the scattering event, we also update the energy and direction of the electron. The energy of a photon-electron system is given by $E' = E'_\gamma + m_e c^2\gamma'_e$. Using conservation of energy, we can find $\gamma'_{e,f}$ with the expression

$$\gamma'_{e,f} = \frac{E'_{\gamma,i} - E'_{\gamma,f} + m_e c^2\gamma'_{e,i}}{m_e c^2}.$$

The momentum of a photon-electron system is given by $\mathbf{p'} = [(E'_\gamma/c)\Omega'_1 + \|\mathbf{p}'_e\|\mathrm{v}'_1]\hat{x} + [(E'_\gamma/c)\Omega'_2 + \|\mathbf{p}'_e\|\mathrm{v}'_2]\hat{y} + [(E'_\gamma/c)\Omega'_3 + \|\mathbf{p}'_e\|\mathrm{v}'_3]\hat{z}$, where $\|\mathbf{p}'_e\| = m_e c\beta'_e\gamma'_e$. Using conservation of momentum in each direction, we can find $\mathrm{v}'_{1,f}$, $\mathrm{v}'_{2,f}$, $\mathrm{v}'_{3,f}$ with the expressions

$$\begin{aligned}
\mathrm{v}'_{1,f} &= \frac{(E'_{\gamma,i}/c)\Omega'_{1,i} + m_e c\beta'_{e,i}\gamma'_{e,i}\mathrm{v}'_{1,i} - (E'_{\gamma,f}/c)\Omega'_{1,f}}{m_e c\beta'_{e,f}\gamma'_{e,f}} \\
\mathrm{v}'_{2,f} &= \frac{(E'_{\gamma,i}/c)\Omega'_{2,i} + m_e c\beta'_{e,i}\gamma'_{e,i}\mathrm{v}'_{2,i} - (E'_{\gamma,f}/c)\Omega'_{2,f}}{m_e c\beta'_{e,f}\gamma'_{e,f}} \\
\mathrm{v}'_{3,f} &= \frac{(E'_{\gamma,i}/c)\Omega'_{3,i} + m_e c\beta'_{e,i}\gamma'_{e,i}\mathrm{v}'_{3,i} - (E'_{\gamma,f}/c)\Omega'_{3,f}}{m_e c\beta'_{e,f}\gamma'_{e,f}}.
\end{aligned}$$

Appendix C

X-ray and Optical Lightcurves of the GRBs in our Sample

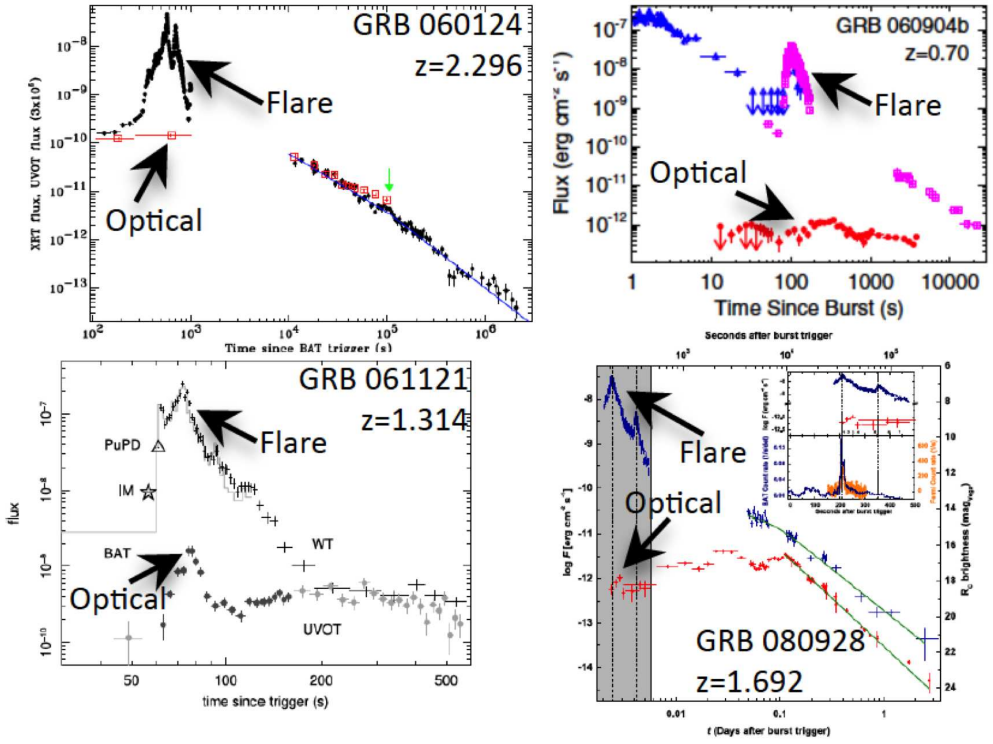

Figure C.1: In this figure, we show the lightcurves for 4/8 X-ray flares in our sample with coincident optical observations. The spectrum for these 4 flares was better fit by a Band-function. The light curves were taken from the following works: GRB 060124 from Romano et al. 2006, GRB 060904B from Rykoff et al. 2009, GRB 061121 from Page et al. 2007, and GRB 080928 from Rossi et al. 2011.

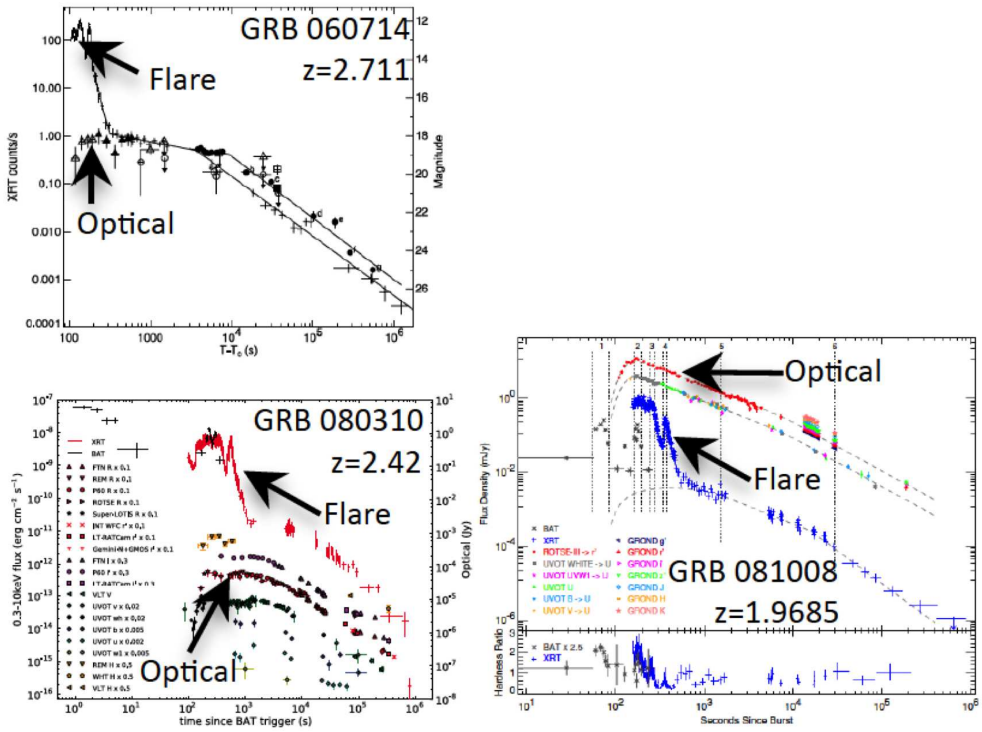

Figure C.2: Same as in Figure C.1. There 3 X-ray flares shown in this figure were better fit by a single-power law. The light curves were taken from the following works: GRB 060714 from Krimm et al. 2007, GRB 080310 from Littlejohns et al. 2012, and GRB 081008 from Yuan et al. 2010.

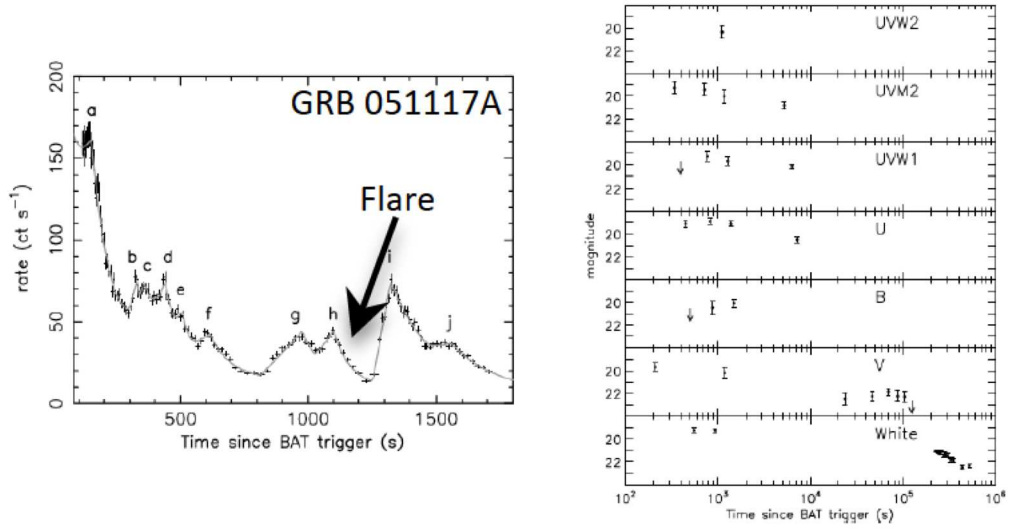

Figure C.3: In this figure we show the lightcurves of GRB 051117A, whose X-ray flare spectrum was better fit by a single-power law. The X-ray light curve for this burst is shown on the left and the optical light curve is shown on the right. Both light curves were taken from Goad et al. 2007.

Bibliography

Abdo, A. A., et al. 2011, ApJ, 734, L27

Achterberg, A., Gallant, Y. A., Kirk, J. G., & Guthmann, A. W. 2001, MNRAS, 328, 393

Antonelli, L. A., et al. 2006, A&A, 456, 509

Band, D., et al. 1993, ApJ, 413, 281

Barnes, J., & Kasen, D. 2013, ApJ, 775, 18

Barniol Duran, R., & Kumar, P. 2011, MNRAS, 417, 1584

Barthelmy, S. D., et al. 2005a, Nature, 438, 994

—. 2005b, Space Sci. Rev., 120, 143

Beck, R. 2011, Space Sci. Rev., 135

Bégué, D., & Iyyani, S. 2014, ApJ, 792, 42

Bégué, D., & Pe'er, A. 2014, ArXiv e-prints

Bégué, D., Siutsou, I. A., & Vereshchagin, G. V. 2013, ApJ, 767, 139

Beloborodov, A. M. 2010, MNRAS, 407, 1033

—. 2011, ApJ, 737, 68

Beniamini, P., & Piran, T. 2013, ApJ, 769, 69

Berger, E. 2014, ARA&A, 52, 43

Berger, E., Fong, W., & Chornock, R. 2013, ApJ, 774, L23

Berger, E., Soderberg, A. M., Frail, D. A., & Kulkarni, S. R. 2003a, ApJ, 587, L5

Berger, E., et al. 2001, ApJ, 556, 556

—. 2003b, Nature, 426, 154

—. 2005, Nature, 438, 988

Bernardini, M. G., Margutti, R., Chincarini, G., Guidorzi, C., & Mao, J. 2011, A&A, 526, A27

Bhattacharya, D. 2001, Bulletin of the Astronomical Society of India, 29, 107

Björnsson, G., Gudmundsson, E. H., & Jóhannesson, G. 2004, ApJ, 615, L77

Blandford, R., & Eichler, D. 1987, Phys. Rep., 154, 1

Blandford, R. D., & McKee, C. F. 1976, Physics of Fluids, 19, 1130

Blandford, R. D., & Znajek, R. L. 1977, MNRAS, 179, 433

Bloom, J. S., et al. 2006, ApJ, 638, 354

Bucciantini, N., Quataert, E., Arons, J., Metzger, B. D., & Thompson, T. A. 2008, MNRAS, 383, L25

Bucciantini, N., Quataert, E., Metzger, B. D., Thompson, T. A., Arons, J., & Del Zanna, L. 2009, MNRAS, 396, 2038

Burrows, D. N., et al. 2005a, Science, 309, 1833

—. 2005b, Space Sci. Rev., 120, 165

Butler, N. R., & Kocevski, D. 2007a, ApJ, 663, 407

—. 2007b, ApJ, 663, 407

Campana, S., et al. 2006, Nature, 442, 1008

Cenko, S. B., et al. 2009, ApJ, 693, 1484

—. 2010, ApJ, 711, 641

—. 2011, ApJ, 732, 29

Chandra, P., et al. 2008, ApJ, 683, 924

—. 2010, ApJ, 712, L31

Chang, P., Spitkovsky, A., & Arons, J. 2008, ApJ, 674, 378

Chen, W.-X., & Beloborodov, A. M. 2007, ApJ, 657, 383

Chevalier, R. A., & Li, Z. 2000, ApJ, 536, 195

Chevalier, R. A., & Li, Z.-Y. 1999, ApJ, 520, L29

Chhotray, A., & Lazzati, D. 2015, ApJ, 802, 132

Chincarini, G., et al. 2007, ApJ, 671, 1903

—. 2010, MNRAS, 406, 2113

Chornock, R., et al. 2010, ArXiv e-prints

Costa, E., et al. 1997, Nature, 387, 783

Couch, S. M., Milosavljević, M., & Nakar, E. 2008, ApJ, 688, 462

Covino, S., et al. 2010, A&A, 521, A53

Curran, P. A., Evans, P. A., de Pasquale, M., Page, M. J., & van der Horst, A. J. 2010, ApJ, 716, L135

Curran, P. A., van der Horst, A. J., & Wijers, R. A. M. J. 2008, MNRAS, 386, 859

Dai, Z. G., & Lu, T. 1998, A&A, 333, L87

Dai, Z. G., Wang, X. Y., Wu, X. F., & Zhang, B. 2006a, Science, 311, 1127

—. 2006b, Science, 311, 1127

Daigne, F., & Mochkovitch, R. 2002, MNRAS, 336, 1271

Deng, W., & Zhang, B. 2014, ApJ, 785, 112

Di Matteo, T., Perna, R., & Narayan, R. 2002, ApJ, 579, 706

Drake, J. F., Opher, M., Swisdak, M., & Chamoun, J. N. 2010, ApJ, 709, 963

Drake, J. F., Swisdak, M., Che, H., & Shay, M. A. 2006, Nature, 443, 553

Drenkhahn, G. 2002, A&A, 387, 714

Drenkhahn, G., & Spruit, H. C. 2002, A&A, 391, 1141

Eichler, D., Livio, M., Piran, T., & Schramm, D. N. 1989, Nature, 340, 126

Eichler, D., & Waxman, E. 2005, ApJ, 627, 861

Evans, P. A., et al. 2007, A&A, 469, 379

—. 2009, MNRAS, 397, 1177

—. 2010, A&A, 519, A102

Falcone, A. D., et al. 2006, ApJ, 641, 1010

—. 2007, ApJ, 671, 1921

Fan, Y., & Piran, T. 2006, MNRAS, 369, 197

Fermi, E. 1949, Physical Review, 75, 1169

Fox, D. B., et al. 2005, Nature, 437, 845

Frail, D. A., Waxman, E., & Kulkarni, S. R. 2000, ApJ, 537, 191

Frail, D. A., et al. 2001, ApJ, 562, L55

—. 2006, ApJ, 646, L99

Friis, M., & Watson, D. 2013, ApJ, 771, 15

Frontera, F., et al. 1998, ApJ, 493, L67

Galama, T. J., et al. 1998, Nature, 395, 670

Gao, H., Lei, W.-H., Wu, X.-F., & Zhang, B. 2013, MNRAS, 435, 2520

Gao, H., & Zhang, B. 2014, ArXiv e-prints

Gao, W.-H. 2009, ApJ, 697, 1044

Gehrels, N., Ramirez-Ruiz, E., & Fox, D. B. 2009, ARA&A, 47, 567

Gehrels, N., et al. 2004a, ApJ, 611, 1005

—. 2004b, ApJ, 611, 1005

—. 2005, Nature, 437, 851

Ghisellini, G., ed. 2013, Lecture Notes in Physics, Berlin Springer Verlag, Vol. 873, Radiative Processes in High Energy Astrophysics

Ghisellini, G., & Celotti, A. 1999, ApJ, 511, L93

Ghisellini, G., Celotti, A., & Lazzati, D. 2000, MNRAS, 313, L1

Giannios, D. 2006, A&A, 457, 763

—. 2008, A&A, 480, 305

—. 2012, MNRAS, 422, 3092

Giannios, D., & Spruit, H. C. 2005, A&A, 430, 1

Goad, M. R., et al. 2007, A&A, 468, 103

Goodman, J. 1986, ApJ, 308, L47

Goodman, J., & MacFadyen, A. 2008, Journal of Fluid Mechanics, 604, 325

Gorbovskoy, E. S., et al. 2012, MNRAS, 421, 1874

Gotz, D., & Mereghetti, S. 2005, GRB Coordinates Network, 3329, 1

Gou, L.-J., Fox, D. B., & Mészáros, P. 2007, ApJ, 668, 1083

Granot, J., Komissarov, S. S., & Spitkovsky, A. 2011, MNRAS, 411, 1323

Granot, J., Königl, A., & Piran, T. 2006, MNRAS, 370, 1946

Granot, J., Piran, T., & Sari, R. 2000, ApJ, 534, L163

Granot, J., & Sari, R. 2002, ApJ, 568, 820

Greiner, J., et al. 2009, ApJ, 693, 1610

Gruzinov, A., & Waxman, E. 1999, ApJ, 511, 852

Guidorzi, C., et al. 2011, MNRAS, 417, 2124

Guo, F., Li, H., Daughton, W., & Liu, Y.-H. 2014, Physical Review Letters, 113, 155005

Guo, F., Liu, Y.-H., Daughton, W., & Li, H. 2015, ApJ, 806, 167

Harrison, F. A., et al. 2001, ApJ, 559, 123

Hjorth, J., et al. 2003, Nature, 423, 847

Inoue, T., Asano, K., & Ioka, K. 2011, ApJ, 734, 77

Ito, H., Nagataki, S., Matsumoto, J., Lee, S.-H., Tolstov, A., Mao, J., Dainotti, M., & Mizuta, A. 2014, ApJ, 789, 159

Jin, Z.-P., Fan, Y.-Z., & Wei, D.-M. 2010, ApJ, 724, 861

Kagan, D., Milosavljević, M., & Spitkovsky, A. 2013, ApJ, 774, 41

Kagan, D., Sironi, L., Cerutti, B., & Giannios, D. 2015, Space Sci. Rev.

Kaneko, Y., Preece, R. D., Briggs, M. S., Paciesas, W. S., Meegan, C. A., & Band, D. L. 2006, ApJS, 166, 298

Kann, D. A., et al. 2010, ApJ, 720, 1513

Keshet, U., Katz, B., Spitkovsky, A., & Waxman, E. 2009, ApJ, 693, L127

King, A., O'Brien, P. T., Goad, M. R., Osborne, J., Olsson, E., & Page, K. 2005, ApJ, 630, L113

Klotz, A., et al. 2008, A&A, 483, 847

Kluźniak, W., & Ruderman, M. 1998, ApJ, 505, L113

Kohri, K., & Mineshige, S. 2002, ApJ, 577, 311

Kohri, K., Narayan, R., & Piran, T. 2005, ApJ, 629, 341

Komissarov, S. S. 2004, MNRAS, 350, 427

Komissarov, S. S., Vlahakis, N., Königl, A., & Barkov, M. V. 2009, MNRAS, 394, 1182

Kopač, D., et al. 2013, ApJ, 772, 73

Kouveliotou, C., Meegan, C. A., Fishman, G. J., Bhat, N. P., Briggs, M. S., Koshut, T. M., Paciesas, W. S., & Pendleton, G. N. 1993, ApJ, 413, L101

Krimm, H. A., et al. 2007, ApJ, 665, 554

Krühler, T., et al. 2009, ApJ, 697, 758

Kulkarni, S. R., et al. 1999, Nature, 398, 389

Kulsrud, R. M. 1998, Physics of Plasmas, 5, 1599

Kumar, K., & Crumley, P. 2015, MNRAS, submitted.

Kumar, P., & Barniol Duran, R. 2009, MNRAS, 400, L75

—. 2010, MNRAS, 409, 226

Kumar, P., & McMahon, E. 2008, MNRAS, 384, 33

Kumar, P., & Panaitescu, A. 2000, ApJ, 541, L51

Kumar, P., & Zhang, B. 2015, Phys. Rep., 561, 1

Kumar, P., et al. 2007, MNRAS, 376, L57

Larsson, J., Ryde, F., Lundman, C., McGlynn, S., Larsson, S., Ohno, M., & Yamaoka, K. 2011, MNRAS, 414, 2642

Lazzati, D., & Begelman, M. C. 2010, ApJ, 725, 1137

Lazzati, D., Morsony, B. J., Margutti, R., & Begelman, M. C. 2013, ApJ, 765, 103

Lazzati, D., & Perna, R. 2007, MNRAS, 375, L46

Lee, H. K., Wijers, R. A. M. J., & Brown, G. E. 2000, Phys. Rep., 325, 83

Lee, W. H., Ramirez-Ruiz, E., & López-Cámara, D. 2009, ApJ, 699, L93

Lei, W.-H., Zhang, B., & Liang, E.-W. 2013, ApJ, 765, 125

Lemoine, M. 2013, MNRAS, 428, 845

Lemoine, M., Li, Z., & Wang, X.-Y. 2013, ArXiv e-prints

Levan, A. J., et al. 2014, ApJ, 792, 115

Leventis, K., van Eerten, H. J., Meliani, Z., & Wijers, R. A. M. J. 2012, MNRAS, 427, 1329

Li, L., et al. 2012, ApJ, 758, 27

Li, L.-X., & Paczyński, B. 1998, ApJ, 507, L59

Li, Z.-Y., & Chevalier, R. A. 2001, ApJ, 551, 940

Liang, E., Zhang, B., Virgili, F., & Dai, Z. G. 2007, ApJ, 662, 1111

Liang, E.-W., Racusin, J. L., Zhang, B., Zhang, B.-B., & Burrows, D. N. 2008, ApJ, 675, 528

Liang, E.-W., Yi, S.-X., Zhang, J., Lü, H.-J., Zhang, B.-B., & Zhang, B. 2010, ApJ, 725, 2209

Littlejohns, O. M., et al. 2012, MNRAS, 421, 2692

Lundman, C., Pe'er, A., & Ryde, F. 2013, MNRAS, 428, 2430

MacFadyen, A. I., & Woosley, S. E. 1999, ApJ, 524, 262

Malesani, D., et al. 2004, ApJ, 609, L5

Margutti, R., Guidorzi, C., Chincarini, G., Bernardini, M. G., Genet, F., Mao, J., & Pasotti, F. 2010, MNRAS, 406, 2149

Margutti, R., et al. 2011, MNRAS, 417, 2144

Martins, S. F., Fonseca, R. A., Silva, L. O., & Mori, W. B. 2009, ApJ, 695, L189

McKinney, J. C. 2005, ApJ, 630, L5

McKinney, J. C., & Blandford, R. D. 2009, MNRAS, 394, L126

McKinney, J. C., & Narayan, R. 2007, MNRAS, 375, 513

Medvedev, M. V., Fiore, M., Fonseca, R. A., Silva, L. O., & Mori, W. B. 2005, ApJ, 618, L75

Medvedev, M. V., & Loeb, A. 1999, ApJ, 526, 697

Melandri, A., et al. 2008, ApJ, 686, 1209

—. 2010, ApJ, 723, 1331

—. 2012, A&A, 547, A82

—. 2014, ArXiv e-prints

Mészáros, P., Ramirez-Ruiz, E., Rees, M. J., & Zhang, B. 2002, ApJ, 578, 812

Meszaros, P., & Rees, M. J. 1993, ApJ, 405, 278

—. 1997, ApJ, 476, 232

Mészáros, P., & Rees, M. J. 2000, ApJ, 530, 292

Metzger, B. D., Giannios, D., Thompson, T. A., Bucciantini, N., & Quataert, E. 2011, MNRAS, 413, 2031

Metzger, B. D., Thompson, T. A., & Quataert, E. 2008, ApJ, 676, 1130

Metzger, B. D., et al. 2010, MNRAS, 406, 2650

Milosavljević, M., & Nakar, E. 2006, ApJ, 651, 979

Milosavljevic, M., Nakar, E., & Zhang, F. 2007, ArXiv e-prints

Mizuno, Y., Pohl, M., Niemiec, J., Zhang, B., Nishikawa, K.-I., & Hardee, P. E. 2011, ApJ, 726, 62

Mizuta, A., Nagataki, S., & Aoi, J. 2011, ApJ, 732, 26

Modjaz, M., et al. 2006, ApJ, 645, L21

Molinari, E., et al. 2007, A&A, 469, L13

Morris, D. C., et al. 2007, ApJ, 654, 413

Nakar, E. 2007, Phys. Rep., 442, 166

Narayan, R., Paczynski, B., & Piran, T. 1992, ApJ, 395, L83

Narayan, R., Piran, T., & Kumar, P. 2001, ApJ, 557, 949

Nousek, J. A., et al. 2006, ApJ, 642, 389

O'Brien, P. T., Willingale, R., Osborne, J. P., & Goad, M. R. 2006a, New Journal of Physics, 8, 121

O'Brien, P. T., et al. 2006b, ApJ, 647, 1213

Paczynski, B. 1990, ApJ, 363, 218

Paczyński, B. 1998, ApJ, 494, L45

Paczynski, B., & Rhoads, J. E. 1993, ApJ, 418, L5

Pagani, C., et al. 2006, ApJ, 645, 1315

Page, K. L., et al. 2007, ApJ, 663, 1125

Panaitescu, A. 2005, MNRAS, 363, 1409

—. 2007, MNRAS, 379, 331

Panaitescu, A., & Kumar, P. 2000, ApJ, 543, 66

—. 2001a, ApJ, 560, L49

—. 2001b, ApJ, 554, 667

—. 2002, ApJ, 571, 779

Panaitescu, A., & Mészáros, P. 2000, ApJ, 544, L17

Panaitescu, A., Mészáros, P., Burrows, D., Nousek, J., Gehrels, N., O'Brien, P., & Willingale, R. 2006, MNRAS, 369, 2059

Panaitescu, A., & Vestrand, W. T. 2011, MNRAS, 414, 3537

Parker, E. N. 1957, J. Geophys. Res., 62, 509

Pe'er, A. 2008, ApJ, 682, 463

—. 2015, ArXiv e-prints

Pe'er, A., Mészáros, P., & Rees, M. J. 2006, ApJ, 642, 995

Pe'er, A., & Ryde, F. 2011, ApJ, 732, 49

Perley, D. A., et al. 2008, ApJ, 688, 470

—. 2009, ArXiv e-prints

—. 2011, AJ, 141, 36

Perna, R., Armitage, P. J., & Zhang, B. 2006, ApJ, 636, L29

Pian, E., et al. 2006, Nature, 442, 1011

Piran, T. 2004, Reviews of Modern Physics, 76, 1143

Piran, T., Sari, R., & Zou, Y.-C. 2009, MNRAS, 393, 1107

Piro, L. 2001, in Gamma-ray Bursts in the Afterglow Era, ed. E. Costa, F. Frontera, & J. Hjorth, 97

Popham, R., Woosley, S. E., & Fryer, C. 1999, ApJ, 518, 356

Pozdnyakov, L. A., Sobol, I. M., & Syunyaev, R. A. 1983, Astrophysics and Space Physics Reviews, 2, 189

Preece, R. D., Briggs, M. S., Mallozzi, R. S., Pendleton, G. N., Paciesas, W. S., & Band, D. L. 2000, ApJS, 126, 19

Proga, D., & Zhang, B. 2006, MNRAS, 370, L61

Qian, Y.-Z., & Woosley, S. E. 1996, ApJ, 471, 331

Racusin, J. L., et al. 2009, ApJ, 698, 43

Rees, M. J., & Meszaros, P. 1992, MNRAS, 258, 41P

—. 1994, ApJ, 430, L93

Rees, M. J., & Mészáros, P. 2005, ApJ, 628, 847

Resmi, L., & Bhattacharya, D. 2008, MNRAS, 388, 144

Rhoads, J. E. 1999, ApJ, 525, 737

Robishaw, T., Quataert, E., & Heiles, C. 2008, ApJ, 680, 981

Rol, E., et al. 2007, ApJ, 669, 1098

Romano, P., et al. 2006, A&A, 456, 917

Roming, P. W. A., et al. 2005, Space Sci. Rev., 120, 95

Rossi, A., et al. 2011, A&A, 529, A142

Rosswog, S. 2007, MNRAS, 376, L48

Ruffini, R., Siutsou, I. A., & Vereshchagin, G. V. 2013, ApJ, 772, 11

Rybicki, G. B., & Lightman, A. P. 1979, Radiative processes in astrophysics (Wiley-Interscience)

Rykoff, E. S., et al. 2009, ApJ, 702, 489

Santana, R., Hernández, R. A., Crumley, P., & Kumar, P. 2015, MNRAS, submitted.

Sari, R., & Esin, A. A. 2001, ApJ, 548, 787

Sari, R., Narayan, R., & Piran, T. 1996, ApJ, 473, 204

Sari, R., & Piran, T. 1999a, ApJ, 517, L109

—. 1999b, ApJ, 520, 641

Sari, R., Piran, T., & Halpern, J. P. 1999, ApJ, 519, L17

Sari, R., Piran, T., & Narayan, R. 1998, ApJ, 497, L17+

Schulze, S., et al. 2011, A&A, 526, A23+

Shen, R.-F., & Zhang, B. 2009, MNRAS, 398, 1936

Silva, L. O., Fonseca, R. A., Tonge, J. W., Dawson, J. M., Mori, W. B., & Medvedev, M. V. 2003, ApJ, 596, L121

Sironi, L., & Goodman, J. 2007, ApJ, 671, 1858

Sironi, L., & Spitkovsky, A. 2011, ApJ, 726, 75, provided by the SAO/NASA Astrophysics Data System

—. 2014, ApJ, 783, L21

Sironi, L., Spitkovsky, A., & Arons, J. 2013, ArXiv e-prints

Soderberg, A. M., et al. 2006, ApJ, 650, 261

—. 2007, ApJ, 661, 982

Sonbas, E., MacLachlan, G. A., Shenoy, A., Dhuga, K. S., & Parke, W. C. 2013, ApJ, 767, L28

Sparre, M., et al. 2011, ApJ, 735, L24

Stanek, K. Z., et al. 2003, ApJ, 591, L17

Starling, R. L. C., et al. 2011, MNRAS, 411, 2792

Stratta, G., et al. 2009, A&A, 503, 783

Sweet, P. A. 1958, in IAU Symposium, Vol. 6, Electromagnetic Phenomena in Cosmical Physics, ed. B. Lehnert, 123

Swenson, C. A., & Roming, P. W. A. 2013, ArXiv e-prints

Swenson, C. A., Roming, P. W. A., De Pasquale, M., & Oates, S. R. 2013, ApJ, 774, 2

Tanvir, N. R., Levan, A. J., Fruchter, A. S., Hjorth, J., Hounsell, R. A., Wiersema, K., & Tunnicliffe, R. L. 2013, Nature, 500, 547

Taylor, G. B., Frail, D. A., Berger, E., & Kulkarni, S. R. 2004, ApJ, 609, L1

Tchekhovskoy, A., & McKinney, J. C. 2012a, MNRAS, 423, L55

—. 2012b, MNRAS, 423, L55

Tchekhovskoy, A., McKinney, J. C., & Narayan, R. 2008, MNRAS, 388, 551

Tchekhovskoy, A., Narayan, R., & McKinney, J. C. 2010, New A, 15, 749

Thompson, C. 1994a, MNRAS, 270, 480

—. 1994b, MNRAS, 270, 480

Thompson, C., Mészáros, P., & Rees, M. J. 2007, ApJ, 666, 1012

Thompson, T. A., Quataert, E., & Murray, N. 2009, MNRAS, 397, 1410

Toma, K., Wu, X.-F., & Mészáros, P. 2011, MNRAS, 415, 1663

Troja, E., Piro, L., Vasileiou, V., Omodei, N., Burgess, J. M., Cutini, S., Connaughton, V., & McEnery, J. E. 2015, ApJ, 803, 10

Ubertini, P., et al. 2003, A&A, 411, L131

Uehara, T., et al. 2010, A&A, 519, A56

Usov, V. V. 1992, Nature, 357, 472

van Paradijs, J., et al. 1997, Nature, 386, 686

Vereshchagin, G. V. 2014, International Journal of Modern Physics D, 23, 30003

Vurm, I., Lyubarsky, Y., & Piran, T. 2013, ApJ, 764, 143

Wanderman, D., & Piran, T. 2010, MNRAS, 406, 1944

Wang, D. X., Xiao, K., & Lei, W. H. 2002, MNRAS, 335, 655

Wang, F. Y., & Dai, Z. G. 2013, Nature Physics, 9, 465

Weibel, E. S. 1959, Physical Review Letters, 2, 83

Werner, G. R., Uzdensky, D. A., Cerutti, B., Nalewajko, K., & Begelman, M. C. 2014, ArXiv e-prints

Wheeler, J. C., Yi, I., Höflich, P., & Wang, L. 2000, ApJ, 537, 810

Wijers, R. A. M. J., & Galama, T. J. 1999, ApJ, 523, 177

Winkler, C., et al. 2003, A&A, 411, L1

Woosley, S. E. 1993, ApJ, 405, 273

—. 2011, ArXiv e-prints

Wu, X. F., Dai, Z. G., Huang, Y. F., & Lu, T. 2003, MNRAS, 342, 1131

Xu, D., et al. 2013, ApJ, 776, 98

Xue, R.-R., Fan, Y.-Z., & Wei, D.-M. 2009, A&A, 498, 671

Yi, S.-X., Wu, X.-F., Wang, F.-Y., & Dai, Z.-G. 2015, ApJ, 807, 92

Yost, S. A., Harrison, F. A., Sari, R., & Frail, D. A. 2003, ApJ, 597, 459

Yost, S. A., et al. 2002, ApJ, 577, 155

Yuan, F., et al. 2010, ApJ, 711, 870

Zalamea, I., & Beloborodov, A. M. 2011, MNRAS, 410, 2302

Zaninoni, E., Bernardini, M. G., Margutti, R., Oates, S., & Chincarini, G. 2013, A&A, 557, A12

Zhang, B. 2011, Comptes Rendus Physique, 12, 206

—. 2014, International Journal of Modern Physics D, 23, 30002

Zhang, B., Fan, Y. Z., Dyks, J., Kobayashi, S., Mészáros, P., Burrows, D. N., Nousek, J. A., & Gehrels, N. 2006, ApJ, 642, 354

Zhang, B., & Mészáros, P. 2001, ApJ, 552, L35

Zhang, B., et al. 2007a, ApJ, 655, 989

Zhang, B.-B., Liang, E.-W., & Zhang, B. 2007b, ApJ, 666, 1002

Zhang, W., MacFadyen, A., & Wang, P. 2009, ApJ, 692, L40

Zhao, X. H., Dai, Z. G., Liu, T., Bai, J. M., & Peng, Z. Y. 2010, ApJ, 708, 1357

Zhao, X.-H., Li, Z., & Bai, J.-M. 2011, ApJ, 726, 89, provided by the SAO/NASA Astrophysics Data System

Zou, Y.-C., Fan, Y.-Z., & Piran, T. 2011, ApJ, 726, L2

Zweibel, E. G., & Yamada, M. 2009, ARA&A, 47, 291

Vita

Rodolfo Santana was born in Northridge, California on 18 September 1987, the son of Rodolfo Flores Santana and Bertha Alicia Santana. He graduated from San Fernando High School in June 2005. In June 2009, he earned a Bachelor of Science degree in Physics from the Massachusetts Institute of Technology. In August 2009, he enrolled as a PhD student in the Astronomy department at the University of Texas at Austin.

Permanent address: 2515 Speedway, Stop C1400
Austin, Texas 78712

This dissertation was typeset with LaTeX[†] by the author.

[†]LaTeX is a document preparation system developed by Leslie Lamport as a special version of Donald Knuth's TeX Program.